NUMERICAL AND EXPERIMENTAL STUDIES OF THE $Fe_xNi_{1-x}Cl_2$ MIXED MAGNETIC SYSTEM

A THESIS

SUBMITTED IN PARTIAL FULFILMENT

OF THE REQUIREMENTS FOR THE DEGREE

OF

DOCTOR OF PHILOSOPHY IN PHYSICS

IN THE

UNIVERSITY OF CANTERBURY

by

Stephen Botha

University of Canterbury

1998

i

Abstract

Previous Mössbauer studies of the $Fe_xNi_{1-x}Cl_2$ system led to conflicting hypothesises about the exact magnetic behaviour of the Fe^{2+} ions in the mixed magnetic phase. This phase occurs between the Fe^{2+} concentration values of $x=0.03$ and 0.12, and at temperatures less than 45 K. Tamaki and Ito (1991,1993) used a model which had co-existing magnetic order, with some Fe^{2+} and Ni^{2+} spins aligned near the crystalline c axis, while the others aligned near the perpendicular xy plane (model 1). The relative population of the two sites is dependent on the concentration x and the temperature. Pollard et al (1982,1991) used a similar model, but with the spins aligned parallel to the x axis or in the xy plane (model 2). Again, the populations of the two sites depended on x and temperature.

New Mössbauer studies were done, and the results are displayed and discussed in this thesis. The new studies concerned mixtures within the mixed phase ($x=0.031$ and 0.052) and the pure anti-ferromagnetic phase ($x=0.15$). Models 1 and 2 both generated similar simulated spectra, which gave similar fits to the experimental spectra. Model 1 generated spectra which fit only marginally better than model 2 spectra. Therefore it was not possible to conclude which model gave a better description of the $Fe_xNi_{1-x}Cl_2$ system, using the new Mössbauer studies.

Monte Carlo studies were also done, to provide a possible explanation for the complex magnetic behaviour which occurs in the mixed phase of $Fe_xNi_{1-x}Cl_2$. The results showed that a random distribution of metal ions does not create co-existing spin order. However, clusters of Fe^{2+} ions embedded in regions of $Fe_xNi_{1-x}Cl_2$ with low values of x did create co-existing magnetic order. The spins aligned near the crystalline c axis or the xy plane, in agreement with model 1. Hence it was concluded that an un-even distribution of metal ions in $Fe_xNi_{1-x}Cl_2$ exists, and directs the complex mixed phase behaviour which has been observed experimentally by workers using Mössbauer spectroscopy and Neutron diffraction techniques. The Monte Carlo programs mentioned in this thesis were written by the Author.

Contents

Contents

List of Tables

List of Figures

Chapter 1

Introduction to the study of the $Fe_xNi_{1-x}Cl_2$ magnetic system.

1.1 Introduction.

This chapter introduces the $Fe_xNi_{1-x}Cl_2$ mixed magnetic crystal and describes its structure, magnetic properties and the various experimental studies that have been performed on it in the past. The justification for further study by Mössbauer spectroscopy is to clear up past experimental disagreements about some of the system's magnetic properties.

Since current theories of mixed-magnetic systems are not capable of describing the $Fe_xNi_{1-x}Cl_2$ system sufficiently well (as will be discussed in chapter 3), numerical studies using the Monte Carlo technique were performed (see chapter 5). This work together with new Mössbauer studies (described in chapter 6) form the topic of this thesis.

1.2 Physical characteristics of $Fe_xNi_{1-x}Cl_2$.

The $Fe_xNi_{1-x}Cl_2$ system (with $0 \leq x \leq 1$) consists of a random mixture of two compounds, $FeCl_2$ and $NiCl_2$. Both compounds have the $CdCl_2$ structure below their melting points of $670\,C$ and $1000\,C$ respectively and at ambient pressure or lower (Vettier and Yelon 1975). The structure is shown in figure 1.1 as reproduced from p 4702 of Vettier and Yelon (1975).

The plane of the layers is the xy plane, and the perpendicular (z) direction to the plane is the c axis. The crystal structure of $Fe_xNi_{1-x}Cl_2$ consists of layers of magnetic-metal ions (either Fe^{2+} or Ni^{2+}) separated from adjacent layers by two layers of chloride ions (Cl^-). The crystal space group of $Fe_xNi_{1-x}Cl_2$ is D_{3d}^5, with each metal ion experiencing a crystal field of

Figure 1.1: Crystal structure of the $Fe_x Ni_{1-x} Cl_2$ system.

Cl^- ion.

Fe^{2+} or Ni^{2+} ion.

Easy plane of pure $NiCl_2$ (xy plane).

Easy axis of pure $FeCl_2$ (c axis).
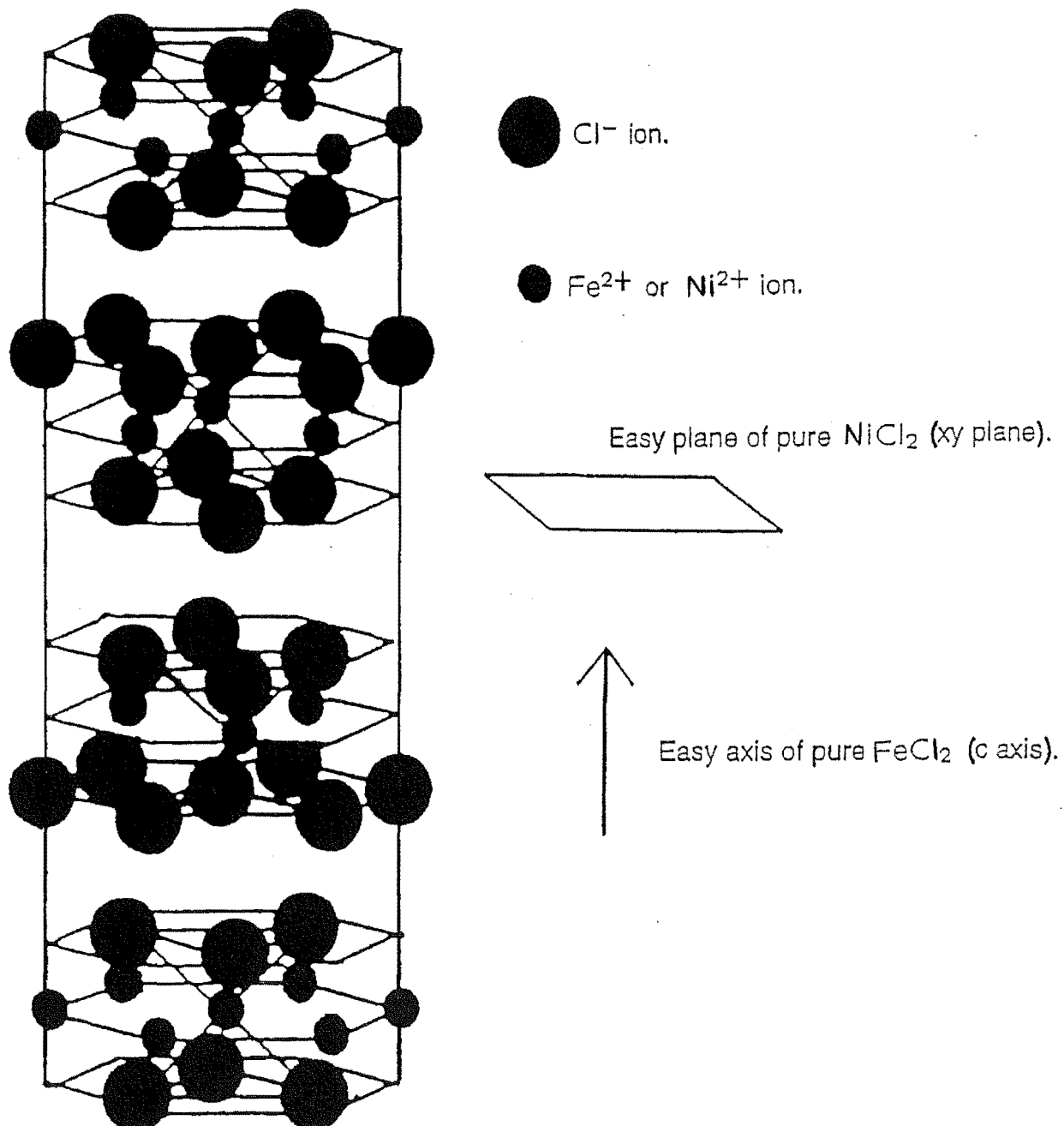
approximately cubic symmetry, with a slight trigonal distortion along the crystalline c axis.

The lattice constants for $FeCl_2$ and $NiCl_2$ differ by 3%, having the values 3.593 Å and 3.483 Å respectively (Donnay and Ondk 1973). The ionic sizes are also similar, 0.76 Å and 0.72 Å for Fe^{2+} and Ni^{2+} respectively (Kittel 1986). The metal ions are positioned in a hexagonal array, with an extra position at the centre of each hexagon; each ion can then be visualised as either being on the outer perimeter of a hexagon or at its centre. Figure 1.2 provides a two-dimensional representation of one layer of the lattice, where each line intersection in the figure is the location for a metal ion. Adjacent layers of metal ions can be visualised as being above or below the figure, but displaced such that the third layer above or below the layer has ions at the same locations (as seen from the view shown in figure 1.1). Two such ions are indicated.

This visualisation correctly represents all of the relations between ions (such as which ion is the neighbour of a specific ion), and is of particular use in numerical simulations of the system, as will be discussed later (Hernandez *et al* 1993) in chapter 5.

1.3 The magnetic properties of $Fe_xNi_{1-x}Cl_2$.

Pure $FeCl_2$ and $NiCl_2$ crystals are both antiferromagnets below their Néel temperatures of 23.6 K and 52 K respectively, with no significant magnetic field being detectable outside a sample of either compound (Wilkinson *et al* 1959 and Lines 1963 respectively). Both have an effective spin 1 (Igel *et al* 1990).

Both $FeCl_2$ and $NiCl_2$ are anti-ferromagnetic metamagnets. This class of magnetic material has the unusual property that a relatively small magnetic field along their crystalline c axes will align all the metal ion spins parallel to it. This is consistent with (in the case of no external field being present) all the magnetic spins being aligned parallel in layers, and antiparallel to the spins in adjacent layers, and is in agreement with experimental data (Starr 1940). If the interlayer exchange interactions between the metal

Figure 1.2: Schematic views of metal ions layers in the $Fe_x Ni_{1-x} Cl_2$ system. Metal ions are located at the line intersections.

Plan view of part of a metal ion layer.
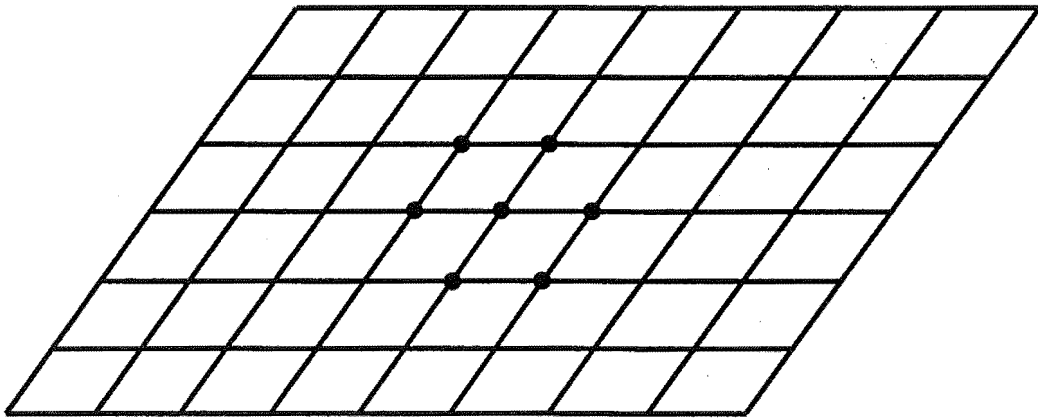
A metal ion.

Side view of 4 adjacent metal ion layers.
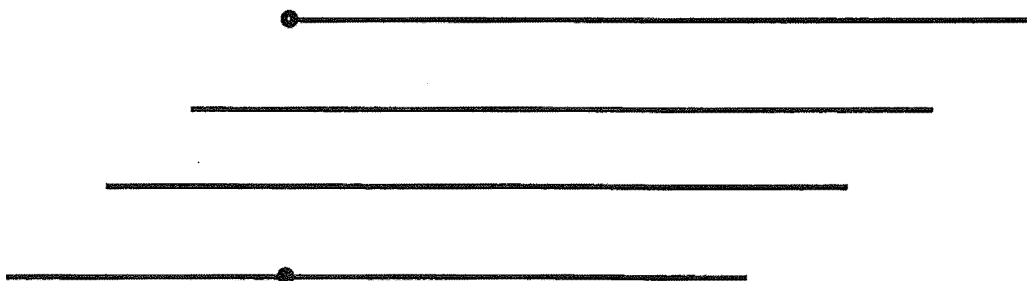
A metal ion.

ions are antiferromagnetic and weaker than the intra-layer exchange interactions (which are ferromagnetic), then this behaviour can be accounted for. The only interaction an external field has to overcome is just the relatively weak interlayer interaction. Neutron diffraction studies of $FeCl_2$ and $NiCl_2$ are consistent with this picture, as described later in this chapter. Of particular interest are the interlayer exchange interactions, since the wavefunctions of two magnetic ions in adjacent cation layers do not overlap because between them is a large distance, containing non-magnetic chloride ions. The exchange interaction involves overlap between the magnetic and non-magnetic ions, and is known as super-exchange (Wagner 1972).

Magnetic anisotropy, that is an interaction between the ionic spins and the lattice, which aligns the spins in particular directions (Chikazumi and Charap 1964), is important for both $FeCl_2$ and $NiCl_2$. The anisotropy strongly aligns the Fe spins along the crystalline c axis in $FeCl_2$, which is labelled the easy axis for the Fe spins, whereas the Ni spins are only weakly held by magnetic anisotropy in the xy plane in $NiCl_2$ (the easy plane for Ni spins) (Wilkinson *et al* 1959 and Fujita *et al* 1969 respectively). In a mixture of the two compounds, the two different magnetic ions will introduce conflicting ordering influences into the system; Fe spins will tend to align parallel to the c axis and influence neighbouring spins to do likewise, through the exchange interaction; Ni spins will attempt to align neighbouring spins in the xy plane. This is an example of a system with competing interactions (competing to create order) and is a class of system which has been extensively studied both theoretically and experimentally over the last few decades (Ito 1986). As will be discussed in detail in chapter 3, both theoretical studies (via renormalization group theory and mean-field theory) and experimental studies show several phases exist on the magnetic-phase diagram, depending on the concentration of Fe and the temperature. Phases exist where the spins behave as for the pure systems (i.e. all spins align along the c axis or in the xy plane), or differently in a mixed phase where the different ionic species have different orientations.

The following sections briefly describe neutron diffraction and Mössbauer experiments, which have helped to determine the exchange and magnetic

anisotropy interaction strengths for $FeCl_2$ and $NiCl_2$. These were useful for creating realistic numerical models of $Fe_xNi_{1-x}Cl_2$ (see chapter 5).

1.4 Experimental studies of $Fe_xNi_{1-x}Cl_2$ single crystals.

1.4.1 Mössbauer studies.

Figure 1.3 shows a magnetic-phase diagram of $FeCl_2$ single crystals derived from Mössbauer and neutron diffraction studies (Ito 1986). Present in the phase diagram are four phases; two pure anti-ferromagnetic phases (phases 2 and 3), a paramagnetic phase (phase 1) with no average spin order at any ionic site and a mixed phase (phase 4) where neutron-diffraction experiments detected order parallel to the c axis and in the xy plane.

Analysis of ^{57}Fe Mössbauer spectra for the mixed phase also shows two orientations for the Fe spins. However there are different conclusions about the orientations. Tamaki and Ito (1991, 1993) examined in detail, by the Mössbauer effect, the spin behaviour for the Fe concentrations $x = 0.034, 0.068$ and 0.079, all of which fall within the mixed phase (phase 4) of figure 1.3. An analysis of their Mössbauer spectra showed not one direction for the Fe spins but two; there were coexisting populations present, with some spins oriented close to the c axis (population 1), while others lay almost in the xy plane (population 2). As the temperature was lowered from its paramagnetic value, population 1 grew at the expense of population 2, and the spins of population 2 slowly moved out of close proximity to the xy plane, and oriented closer to the c axis. Similar spin behaviour also occurs in the $CsMn_{1-x}Co_xCl_3 \cdot 2H_2O$ mixture of antiferromagnets (Kato 1994). However, most other mixed magnetic systems simply show one orientation for each species in the mixed phase, which is consistent with several theoretical studies (see chapter 3).

Figure 1.3: Magnetic phase diagram for $Fe_xNi_{1-x}Cl_2$ reproduced from Ito (1986).
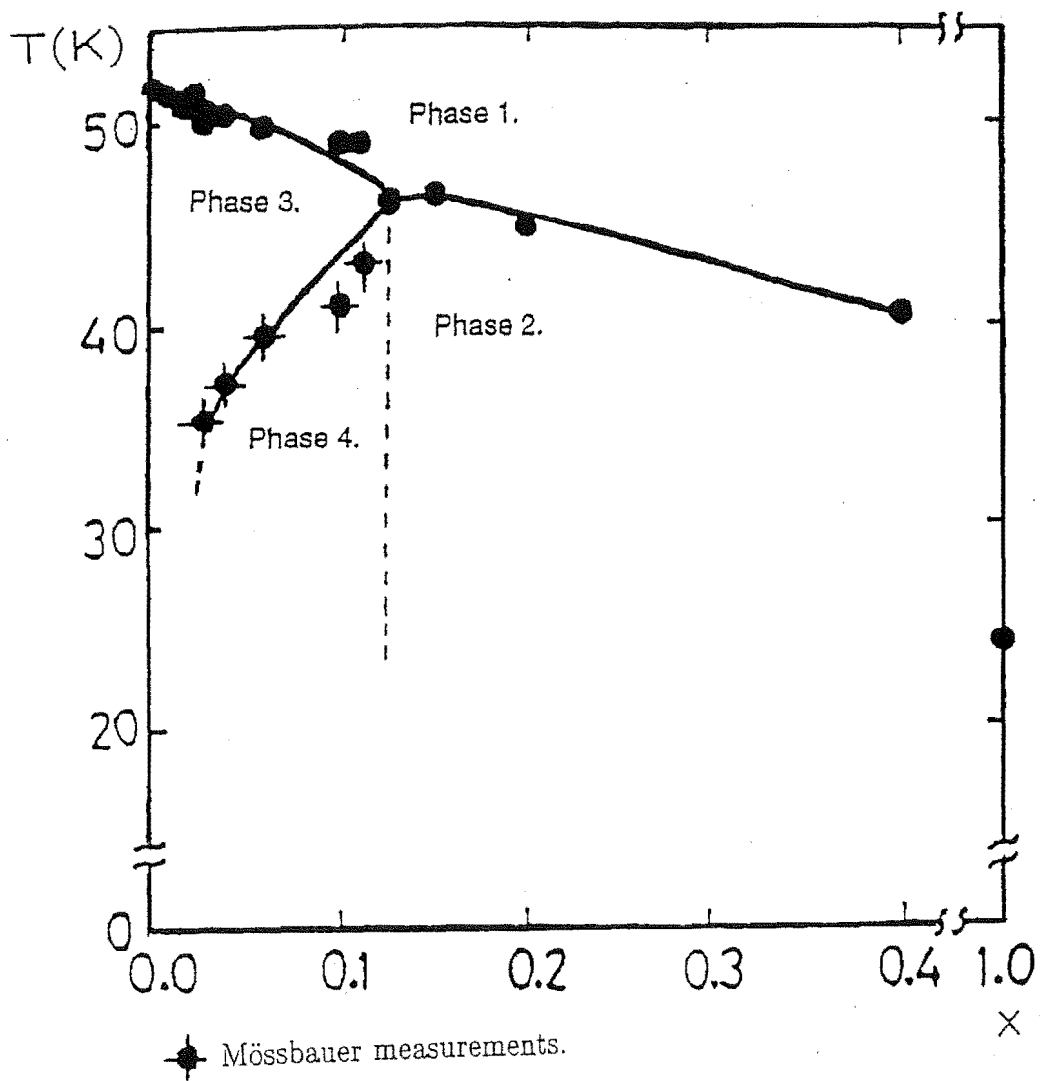
Phase 1: Paramagnetic phase.

Phase 2: Spins align along the c axis.

Phase 3: Spins lie in the xy plane.

Phase 4: The mixed phase.

Other workers utilising Mössbauer spectroscopy also detected the pre-
sence of Fe^{2+} ions with different spin orientations coexisting in the mixed
phase, but the exact behaviour within those domains was different. Again a
paramagnetic phase and two pure anti-ferromagnetic phases were detected
(and in the same regions as shown in figure 1.3). In the mixed phase, the
Fe spins oriented either parallel or perpendicular to the c axis (they lie in
the xy plane); as temperature decreases, the proportion of spins parallel
to the c axis increases (Pollard et al 1991). There was no reorientation of
population 2 spins out of the xy plane as observed by Tamaki et al and the
orientations themselves were different. The spins orientations and populati-
ons for several different values of the Fe concentration x are shown in tables
1.1 to 1.3 from Tamaki et al (1991, 1993), and the results from Pollard et al
(1982,1991) are shown in table 1.4 to allow a direct comparison. In each
table, Fe spin orientations are given in degrees with respect to the crystal c
axis.

As is clear in tables 1.1 to 1.4, increasing concentrations of Fe increa-
ses spin order close to the c axis, as does decreasing the temperature. As
the temperature decreases, energy differences between states becomes more
important in determining spin orientations; whereas energy differences bet-
ween different orientations becomes irrelevant near or higher than the pa-
ramagnetic temperature for the system. So the ability of the Fe magnetic
anisotropy to orient spins close to the c axis is enhanced. And higher con-
centrations of Fe in the system means more magnetic-anisotropy energy is
present in the system, trying to create order along the c axis.

Pollard et al (1991) also analysed previous Mössbauer spectra that Ito
et al (1983) had previously recorded, but had not been able to analyse suc-
cessfully, by taking into account thickness effects which the original authors
had not. When this was done, results similar to those in table 1.4 were ob-
tained, with parallel and perpendicular order (to the c axis) being present
simultaneously in the mixed phase.

Although the two group's results differ, they do share the same obser-
vation of the coexistence phenomena of different spin behaviours, which
does not agree with several theoretical predictions for mixtures of magnets

with competing order parameters. These predictions and their relationship to Mössbauer spectra obtained from the $Fe_xNi_{1-x}Cl_2$ system will be discussed in chapter 3.

T(K)	Fe spin orientations(°)	Proportions in the spectrum.
4.2	20 and 90	0.5 and 0.5
10	20 and 68	0.45 and 0.55
15	20 and 73	0.4 and 0.6
25	20 and 80	0.3 and 0.7
40	20 and 90	0 and 1.0
48	20 and 90	0 and 1.0

Table 1.1: Mössbauer data for the Fe concentration x=0.034, with the spin orientations taken relative to the crystalline c axis. Data from Tamaki et al (1993).

T(K)	Fe spin orientations(°)	Proportions in the spectrum.
4.2	20	1.0
25	20 and 75	0.85 and 0.15
35	20 and 80	0.7 and 0.3
42	20 and 85	0.5 and 0.5
44	20 and 90	0.4 and 0.6
46	20 and 90	0.3 and 0.7
47	20 and 90	0.2 and 0.8
48	20 and 90	0.2 and 0.8

Table 1.2: Mössbauer data for the Fe concentration x=0.068, with the spin orientations taken relative to the crystalline c axis. Data from Tamaki et al (1991).

T(K)	Fe spin orientations($^\circ$)	Proportions in the spectrum.
49	20 and 60	0.2 and 0.8
40	20	1.0

Table 1.3: Mössbauer data for the Fe concentration x=0.079, with the spin orientations taken relative to the crystalline c axis. Data from Tamaki et al (1993).

T(K)	Fraction of Fe spins parallel to the c axis.
25	0.74
35	0.57
42	0.35
44	0.27
46	0.08

Table 1.4: Mössbauer data for the Fe concentration x=0.10, with the spins found either parallel or perpendicular to the crystalline c axis. Data from Pollard et al (1991).

1.4.2 Neutron diffraction studies of $Fe_xNi_{1-x}Cl_2$.

Ito et al (1983) studied $Fe_xNi_{1-x}Cl_2$ by neutron diffraction over the Fe concentration range of $x = 0.005$ to 0.12, which, at low temperatures, has the crystal in the mixed phase, or in a phase with spins in the xy plane as can be seen in figure 1.3. Again it is found that spin order both parallel and perpendicular to the c axis exists in the mixed phase. However since neutron diffraction measures large-scale magnetisation and not the orientations of individual spins, the technique cannot be used to investigate individual Fe spin behaviours, for which Mössbauer spectroscopy is ideally suited.

It should be emphasised that neutron diffraction techniques cannot distinguish between Fe and Ni spins; both species contribute to the number of neutrons detected at different scattering angles. The results showing simultaneous parallel and perpendicular order is in fact mainly due to the presence of Ni spins, since they make up the bulk of the spins present in the mixed phase region (as x is less than 0.12 in that region).

It was also noted that the lower phase transition from spins aligned along (or antiparallel to) the c axis to the mixed phase is broad. This would indicate a possible coupling between the parallel and perpendicular components of the spins. If such couplings were random from site to site, the system would break up into domains, each of which has their own slightly different transition temperature, hence explaining the broadened phase transitions (Wong 1986). Such random interaction terms could be very small and still explain the broadened transition; the average interaction is inversely proportional to the size of the domains in question (Imry 1975), and the domains may be large.

Other neutron-diffraction studies of relevance have studied the pure $FeCl_2$ and $NiCl_2$ constituents of $Fe_x Ni_{1-x} Cl_2$ mainly to calculate the values of the various exchange interactions and magnetic anisotropies. The different studies all show the presence of strong ferromagnetic exchange interactions between nearest neighbours and weaker antiferromagnetic ones between next nearest neighbours in the metal ion planes; also a weak antiferromagnetic exchange interaction between nearest neighbours in different planes. The values of the exchange constants for nearest in-plane, next-nearest in-plane and nearest between-plane spin pairs are 7.88 K, -1.04 K and -0.36 K respectively for $FeCl_2$ (Birgeneau et al 1972), and 43.4 K, -9.7 K and -1.54 K respectively for $NiCl_2$ (Lindgard et al 1975). The nearest between-plane exchange constants were calculated on the assumption that each metal ion interacts with 6 metal ions on adjacent planes, and the exchange constants given assume that the total exchange energy of the system is written in terms of a sum over spin pair exchange energies, without double counting.

Since Mössbauer spectroscopy and neutron diffraction studies measure different aspects of the $Fe_x Ni_{1-x} Cl_2$ system, they are complementary to one another.

1.5 Theoretical studies of the $Fe_xNi_{1-x}Cl_2$ system.

These studies will be discussed in chapter 3 where the main conclusion that will be drawn is that a numerical approach to the understanding of the spin behaviours in $Fe_xNi_{1-x}Cl_2$ is preferable to a theoretical model. The theoretical methods are useful for systems which are uniform in space. Numerical simulations can easily model any spatial variations in the system, such as clusters of Fe ions which may form, possibly giving rise to the coexisting Fe spin populations which are observed by Mössbauer spectroscopy.

1.6 Overview of the thesis.

Theoretical details of Mössbauer spectroscopy relevant to the experimental studies of $Fe_xNi_{1-x}Cl_2$ detailed in this thesis are described in chapter 2. The important hyperfine interactions are described, as well as the interpretation of Mössbauer spectra obtained from single crystal absorbers.

The most commonly used theoretical models of mixed-magnetic systems are discussed in chapter 3. Mean-field theory and its applications to magnetic systems is discussed in sections 3.2 and 3.3. The more modern renormalisation group theory is described in sections 3.4 - 3.6. It is concluded that a numerical approach to the description of $Fe_xNi_{1-x}Cl_2$ is required, and the Monte Carlo technique which was used for this purpose is discussed in section 3.9.

Chapter 4 describes the procedures which were used to produce Mössbauer spectra of $Fe_xNi_{1-x}Cl_2$ single crystals. The methods used to create the single crystal absorbers are listed in section 4.2, and details of the Mössbauer equipment and usage in obtaining adequate absorption spectra are detailed in section 4.3.

Chapter 5 discusses in detail the Monte Carlo techniques used to model the $Fe_xNi_{1-x}Cl_2$ system. It is found that a completely random distribution of metal ions within layers does not give a satisfactory explanation for the coexisting magnetic order detected by Mössbauer spectroscopy occuring in the mixed phase of $Fe_xNi_{1-x}Cl_2$. This is discussed in section 5.2. Sections 5.3 and 5.4 describe cluster-based simulations that do provide an explanation

for the co-existing magnetic behaviour. Alternative explanations are briefly described in section 5.5.

The interpretation of the Mössbauer spectra which were obtained for this thesis in terms of hyperfine parameters at the ^{57}Fe nuclei is discussed in chapter 6. This chapter also contains a discussion about what can be concluded from the Mössbauer and numerical studies described in this thesis, as they apply to the $Fe_x Ni_{1-x} Cl_2$ system, and mixed magnetic systems in general.

Chapter 2

Mössbauer spectroscopy.

2.1 Introduction.

This chapter describes the Mössbauer effect and techniques based on it, which are useful for determining a number of nuclear and electronic variables for a variety of atomic and ionic systems. The analysis of experimental Mössbauer spectra is discussed, with particular attention being paid to the spectra obtained for ^{57}Fe nuclei, which are the nuclei investigated by Mössbauer spectroscopy in the case of the $Fe_xNi_{1-x}Cl_2$ system.

2.2 The Mössbauer effect.

2.2.1 Resonant absorption of radiation- the Mössbauer effect.

When a free atomic or ionic nucleus emits γ radiation, arguments based on the conservation of energy and momentum for the system show that the energy of the γ-ray is less than the energy gap between the nuclear transitions that gave rise to the radiation (Bancroft 1973). This energy difference can be expressed as

$$E_t - E_\gamma = E_R + E_D \qquad (2.1)$$

where E_t is the energy difference between the nuclear levels that gave rise to the transition, E_γ is the actual photon energy, and E_R and E_D refer to the energy of recoil of the nucleus and energy due to the velocity of the nucleus before the transition occurred (the Doppler term). As a consequence of the recoil and Doppler terms, the photon energy on average is less than the transition energy, and takes on different possible values (i.e. is broadened) creating an emission line with a width far greater than the value which follows solely from a consideration of the Heisenberg lifetime for the transition.

If an atom or ion possessing a similar nuclear transition to the emitting nucleus were to absorb the γ radiation, there would be little resonant absorption since the distribution of energies of the radiation are shifted below the transition energy, while the process of absorption of the γ-ray with the absorbing nucleus shifts the possible energies of absorption on average above the transition energy (and broadening also occurs).

In 1957 Mössbauer discovered that, in certain cases, the energies of the γ-rays could closely match the transition energy, with a line width close to the value from the uncertainty in the lifetime of the transition. The same was true for the absorbing process. This is known as the Mössbauer effect (Wertheim 1964). The emitting and absorbing nuclei are both fixed in a solid (such as a crystal lattice), and as a result the energy loss due to recoil can be very much lessened, as the whole lattice can now recoil, not simply one nucleus alone (Frauenfelder 1963). Quantum mechanically, the recoil energy can be transferred to possible phonon (vibrational) excitations in the lattice, but only if the energy is close to a possible phonon energy for the crystal, which is quantised. If it is transferred, the nucleus recoils. If not, then the entire lattice recoils, which has a far larger mass than a single nucleus; hence the recoil energy is far lower than that associated with one nucleus emitting or absorbing radiation. The fraction of γ-rays that are emitted or absorbed via this lattice recoil mechanism is denoted f, the recoil-less fraction. These are the rays that form the absorption lines in Mössbauer spectra. Likewise Doppler energy broadening is dramatically decreased through the same mechanism (Gibb 1976).

The absorber used in a Mössbauer experiment will typically have several different absorptions transitions present, and the source one transition only. The source radiation energy is altered by vibrating the source away from and towards the absorber. The Doppler effect then varies the source photon energy to span the energy range of interest (to cover all of the absorption transitions). Counts are then made at each velocity of the number of γ-rays that passed through the absorber, allowing the measurement of the relative absorption at different energies to be made; these absorptions can then be related to nuclear and electronic quantities. If the spectral lines are narrow enough, very small shifts in these quantities can be measured.

A useful expression for the spectra obtained from Mössbauer absorption experiments is given by

$$n(v) = f_S n_0 (1-h) \int_{E_1}^{E_2} S(E+E\frac{v}{c})e^{-\sigma(E)T_A} dE + (1-f_S+f_S h)n_0 + n_a \quad (2.2)$$

where $n(v)$ is the number of γ-rays detected at velocity v, c is the speed of light, f_S is the recoil-less fraction for γ emission (for the transition of interest) from the source, and n_0 is the number of γ-rays detected at velocities where no absorption occurs (Pollard 1982). n_a is the number of counts received from radiation, which is due to transitions other than the Mössbauer transition. h is the fraction of radiation which does not pass through the absorber; due for example to holes in the absorber (which could not completely be eliminated). E represents the radiation energy, which is integrated over the range E_1 to E_2 which is taken as $-\infty$ to $+\infty$ because the energy range detected is much greater than the linewidth of the source profile, and the detector response is virtually constant over that range (Ure and Flinn 1971 and Pollard 1982). The function S in the integral is the source profile, giving the probability of finding radiation at any particular energy E. $e^{-\sigma(E)T_A}$ gives the probability that radiation is transmitted by the absorber, where T_A is the effective absorber thickness (a measure of the amount of absorbing material present).

The first term in equation 2.2 creates absorption lines in the Mössbauer spectrum. It represents the number of γ-rays which can be absorbed by the Mössbauer transition, but which are transmitted instead. $f_S n_o (1 - h)$ is the number of γ photons available to be absorbed at any velocity, which are recoil-less and actually pass through the absorber. The fraction of these transmitted is given by the convolution integral. The second term measures the number of Mössbauer transition γ-rays that cannot be absorbed, because they involve recoiling processes (the $1 - f_S$ fraction), or simply do not pass through the absorber (the $f_S h$ fraction). These rays simply add to the total background count of radiation observed where no absorption takes places, as do the rays represented by the third term in equation 2.2.

The aim of Mössbauer spectroscopy is to determine the cause of the transmission term in the convolution integral in equation 2.2, and to relate it to the nuclear and electronic quantities which the experimenter wishes to determine. This process is discussed in the final section of this chapter.

2.2.2 Characteristics of useful Mössbauer nuclei.

The nuclei used in Mössbauer experiments must have several features to allow the spectra to be easily obtainable and useful. The recoil-less fraction f must be high, to get many resonance events occurring. The half life of the transition must be large enough to ensure small widths of the spectral lines, but not so long that achieving resonance energy is impossible with vibrations of the experimental apparatus shifting the lines apart. The γ-rays must be easily detectable. A source with a long half life must exist so that many of the states that give rise to the emission of the source γ-rays can always be present. The nuclei must be stable enough to remain in the experimental apparatus long enough to act as an absorber (Gibb 1976).

^{57}Co is such a source, with a useful 14.4 keV transition between nuclear spins states of $\frac{3}{2}$ and $\frac{1}{2}$ with a half-life of $T_{\frac{1}{2}} = 10^{-7}$ seconds. This half-life can be related to the linewidth Γ (the energy difference between points on the emission line with half maximum intensity) by equation 2.3 (Wertheim 1964)

$$\Gamma = \frac{\ln 2 \cdot h}{2\pi T_{\frac{1}{2}}}$$
(2.3)

where h is Planck's constant, which gives $\Gamma = 4.6 \times 10^{-9}$ eV (This is equivalent to a Doppler shift in the 14.4 keV γ-ray energy due to a velocity of 0.1mm/s). This is smaller than the transition energy of 14.4 keV by a factor of 10^{-13}, and allows high resolution studies to be carried out, such as hyperfine interactions in $Fe_xNi_{1-x}Cl_2$ single crystals.

^{57}Fe is a relatively rare isotope of iron, with a natural abundance of 2.1(1) % (CRC 1997), but it can be easily doped into samples to achieve satisfactory spectra. In the $Fe_xNi_{1-x}Cl_2$ system, $FeCl_2$ (containing only the ^{57}Fe isotope) was added to the mixture before it forms into a single crystal, as will be discussed in chapter 4.

The next section discusses the quantities of interest which can be calculated via Mössbauer spectra, for the absorption spectra which are commonly taken for systems such as $Fe_xNi_{1-x}Cl_2$.

2.3 Nuclear and electronic quantities obtained from Mössbauer spectroscopy.

The following quantities discussed are termed *hyperfine interactions* since they involve weak interactions between the nucleus and its environment.

2.3.1 The isomer shift.

The isomer shift (also known as the chemical isomer shift or centre shift) is the change in electrical energy associated with the interaction between orbiting electrons and the nucleus, and takes into account the fact that the nucleus is not a point charge. If the nucleus is assumed (to a good approximation) to be spherical, then the energy difference between an excited state and the ground state can be written as

$$\delta E_e - \delta E_g = K(\psi(0)_s)^2(R_e^2 - R_g^2)$$
(2.4)

where δE_e and δE_g, R_e and R_g represents the energy shifts and nuclear radii for the excited and ground states of the nucleus respectively, K is a constant depending on the nucleus and $\psi(0)_s$ represents the wavefunction at the nucleus for s electrons; this term depends on the electronic state of the atom or ion, whereas the other expressions in equation 2.4 are nuclear quantities which don't change unless a different nuclear species is used. Other electron orbitals can also contribute to this energy difference indirectly, by shielding the s electron wavefunction from the nucleus (by decreasing $\psi(0)_s^2$) (Gibb 1976).

The energy difference between E_e and E_g is that of the photon emitted, and will in general be different for the source and absorber nuclei. The difference is termed the *isomer shift* IS (Thosar *et al* 1983)

$$IS = K(R_e^2 - R_g^2) \left[(\psi(0)_s^2)_A - (\psi(0)_s^2)_S \right] \qquad (2.5)$$

where the subscripts A and S in equation 2.5 refer to the absorber and source nuclei, and the various terms are defined as in equation 2.4. This energy difference in the photon emitted by the source and absorbed by the absorbing nuclei shifts all the Mössbauer spectral lines equally, as no term in equation 2.5 refers to the nuclear spin.

2.3.2 Nuclear electric quadrupole coupling to the electric field gradient.

The nuclear electric quadrupole interaction is an interaction between the nuclear electric quadrupole moment and the spatial gradient of the electric field at the Mössbauer nucleus. The quadrupole moment Q (a measure of the difference between the nuclear shape and a perfect sphere) can be expressed as

$$Q = \frac{1}{|e|} \int \rho r^2 (3cos^2\theta - 1)d\tau \qquad (2.6)$$

where e is the electron charge, ρ is the density of charge at a volume element $d\tau$, r is the distance of the volume element from the nucleus and θ is the angle between vector r and the nuclear spin axis (Gibb 1976). Q for the ground state of ^{57}Fe (with nuclear spin $I = \frac{1}{2}$) is zero, while $Q = 0.21 \times 10^{-28}m^2$ for the $I = \frac{3}{2}$ excited state (Mössbauer effect data index 1976).

The nuclear electric quadrupole interacts with the electric field gradient tensor which has components

$$\nabla_i E_j = -\frac{\partial^2 V}{\partial x_i \partial x_j} = -V_{ij} \qquad (2.7)$$

where V is the electric potential at the nucleus, and x_i, x_j (with i,j $= 1...3$) refer to the Cartesian x, y or z axes (Kolk 1984).

For convenience the *principal axis system* is chosen to describe the electric field gradient since in that case the gradient terms in equation 2.7 are all equal to zero except for the diagonal terms V_{xx}, V_{yy} and V_{zz}. These components are not independent; they can be inter-related by the expression

$$V_{xx} + V_{yy} + V_{zz} = 0 \qquad (2.8)$$

since the components must obey the Laplace equation, and there is no electronic charge in the nuclear region other than s electrons. Since they have a spherically symmetrical distribution about the nucleus, they do not contribute to the right hand side of expression 2.8 (Thosar *et al* 1983).

Only two variables are needed to write down the quadrupole interaction. These are usually chosen to be V_{zz} and

$$\eta = \frac{V_{xx} - V_{yy}}{V_{zz}} \qquad (2.9)$$

where the z axis is chosen such that $|V_{zz}| > |V_{yy}| \geq |V_{xx}|$ in the principal axis system, and η is the asymmetry parameter which expresses the difference between V_{xx} and V_{yy} for the chosen axis system. It has values between 0 and 1 (Thosar *et al* 1983).

The Hamiltonian for the electric quadrupole interaction can be written as

$$H_{QS} = \frac{|e|QV_{zz}}{4I(2I-1)} \left[3I_z^2 - \mathbf{I}^2 + \eta(I_x^2 - I_y^2) \right] \qquad (2.10)$$

where I is the nuclear spin and $\mathbf{I}$ is the nuclear spin operator with Cartesian components I_x, I_y and I_z (Thosar *et al* 1983). The eigenvalues E_{QS} of the electric quadrupole Hamiltonian are given by

$$E_{QS} = \frac{|e|QV_{zz}}{4I(2I-1)} \left(3m_I^2 - I(I+1) \right) \left(1 + \frac{\eta^2}{3} \right)^{\frac{1}{2}} \qquad (2.11)$$

where m_I is the projection of the nuclear spin along the z axis with the values $\pm\frac{1}{2}$, $\pm\frac{3}{2}$ for the excited state of ^{57}Fe. These pairs of values for m_I form two doublets, separated by an energy QS equal to

$$QS = \frac{1}{2}|e|QV_{zz} \left(1 + \frac{\eta^2}{3} \right)^{\frac{1}{2}} \qquad (2.12)$$

(Thosar *et al* 1983).

The electric field gradient tensor $\nabla\mathbf{E}$ is created by external charges on neighbouring atoms or ions (the lattice contribution) and electrons orbiting the Mössbauer nucleus (the valence electron contribution) (Kolk 1984).

2.3.3 Hyperfine magnetic fields.

Magnetic fields at the nucleus can interact with the nuclear magnetic moment $\boldsymbol{\mu}$ via the Hamiltonian term

$$H_M = -\boldsymbol{\mu} \cdot \mathbf{B} = -g_I \mu_N \mathbf{I} \cdot \mathbf{B} \qquad (2.13)$$

where $\mathbf{B}$ is the magnetic field acting at the nucleus, μ_N is the nuclear magneton and g_I is the Lande g factor when the nucleus is in the spin state I and has the value 0.18121(2) and $-0.10354(3)$ for a ^{57}Fe ion nucleus in the ground and excited state, respectively (Mössbauer effect data index 1976). The magnetic field can have a source external or internal to the Mössbauer atom or ion. In this work on $Fe_x Ni_{1-x} Cl_2$ the external magnetic field was zero. The eigenvalues of expression 2.13 are given by

$$E_m = -g_I \mu_N B m_I \qquad (2.14)$$

where m_I are the possible values of the magnetic quantum number for the nucleus (which give the quantised values for the projection of the nuclear spin along a z axis chosen parallel to the magnetic field $\mathbf{B}$), and μ and B are the magnitudes of the nuclear magnetic moment and magnetic field at the nucleus, respectively (Kolk 1984). The internal magnetic field can itself have several sources. Interactions between outer electrons and s electrons leads to a magnetic field at the nucleus, termed the *Fermi-contact term* $\mathbf{B_s}$

$$|\mathbf{B}_s| = \frac{2\mu_0 \mu_B}{3} \left[(\psi_{up}(0))^2 - (\psi_{down}(0))^2 \right] \qquad (2.15)$$

where μ_0 and μ_B are the magnetic permeability of free space and the Bohr magneton, respectively. The ψ terms represent electron spin densities at the nucleus, either parallel (up) or anti-parallel (down) to the nuclear magnetic moment (Thosar *et al* 1983). The Fermi-contact term can also be written as

$$\mathbf{B}_s = \frac{1}{2} B_c \langle \mathbf{S} \rangle \qquad (2.16)$$

where B_c is the Fermi-contact effective field of approximate magnitude -44 T (Greenwood and Gibb 1971) and S is the electronic spin. The presence of orbital angular momentum can also induce a magnetic field at the nucleus. This field $\mathbf{B}_L$ is given by

$$\mathbf{B}_L = \frac{\mu_0 \mu_B}{2\pi} \left\langle r^{-3} \right\rangle \langle \mathbf{L} \rangle \qquad (2.17)$$

where $\langle r^{-3} \rangle$ refers to the expectation value of r^{-3} where r is the distance of electrons from the nucleus (and has a value of approximately 3.7 au), and L is the orbital angular momentum operator (Kolk 1984). If the orbital angular momentum is quenched (has a zero expectation value), then spin-orbit interactions can still produce a contribution to this field (Thosar *et al* 1983). A further magnetic field term describes the interaction between the orbital spin and the nuclear magnetic moment

$$\mathbf{B}_D = \frac{\mu_0 \mu_B}{84\pi} \left\langle r^{-3} \right\rangle \left\langle \frac{3}{2} \left[\mathbf{L}(\mathbf{L} \cdot \mathbf{S}) + (\mathbf{L} \cdot \mathbf{S})\mathbf{L} \right] - L(L+1)\mathbf{S} \right\rangle \qquad (2.18)$$

(Kolk 1984).

The combination of all these fields gives the total field B

$$\mathbf{B} = \mathbf{B}_S + \mathbf{B}_L + \mathbf{B}_D \qquad (2.19)$$

which appears in equation 2.13 to give the hyperfine magnetic splittings observed in the Mössbauer spectra.

2.3.4 Combined hyperfine interactions.

In general the isomer shift, electric quadrupole and magnetic hyperfine interactions are all present and together determine the energies levels of the

different nuclear spin states, via the total Hamiltonian H_{total}

$$H_{total} = IS + H_{QS} + H_M \qquad (2.20)$$

where IS refers to the isomer-shift energy and H_{QS} and H_M refers to the electric field gradient and magnetic energy expressions of equations 2.10 and 2.13 respectively. The isomer-shift term simply moves the entire spectrum towards positive or negative Doppler velocities; the latter two interactions are the important factors in determining the energies and intensities of the Mössbauer absorption lines.

When only one of the latter two interactions is present (and $\eta = 0$ if that interaction is the quadrupole-coupling interaction), then the energy eigenstates of equation 2.20 are single I_z angular momentum states. In general, with all three hyperfine interactions present, the energy eigenstates are linear combinations of I_z angular momentum states, and equation 2.20 has no simple analytical solution. Its matrix representation must then be diagonalized to calculate the energy eigenstates and eigenvalues (Greenwood and Gibb 1971).

2.4   The absorption of γ radiation.

The previous sections have described how nuclear energy levels are shifted due to hyperfine interactions. A transition between two energy levels creates (absorbs) a photon, given rise to an emission (absorption) line with an intensity I_n that can be split into two factors, one of which is independent of angular factors, while the other is not. The first factor is given by the Clebsch-Gordan coefficient

$$(\text{Intensity factor})_1 = \langle I_1 J - m_1 m | I_2 m_2 \rangle^2 \qquad (2.21)$$

where I_1 and I_2 are the spins of the two nuclear states in question, and

m_1 and m_2 are the z components of the appropriate nuclear spins. This equation is valid for transitions between pure angular momentum states. J is the quantum number of the vector sum $\mathbf{I_1} + \mathbf{I_2}$ and $m = m_1 - m_2$. The transitions of importance for this thesis that occur in ^{57}Fe nuclei are the M_1 transitions, i.e. magnetic dipole transitions with $J = 1$, which occur between the nuclear states with spin $I = \frac{1}{2}$ or $\frac{3}{2}$. There are nominally eight such transitions, but two are forbidden by the selection rule $m = 0, \pm 1$ (Greenwood and Gibb 1971).

The second factor (Intensity factor)$_2$ depends on angles defined relative to the quantisation axis used (which is along the magnetic field if no electric quadrupole interactions are present, and along V_{zz} if are). The factors are simple, and are listed for each M_1 transition in ^{57}Fe in Gibb (1976) p 41. The total intensity I_n for an absorption line in a Mössbauer spectrum is then given by

$$I_n = (\text{Intensity factor})_1 \cdot (\text{Intensity factor})_2 \qquad (2.22)$$

In general, the eigenstates will not be single angular momentum I_z states, leading to complex expressions for the absorption line intensities, and eight lines then occur in the Mössbauer spectrum (Kolk 1984).

2.5 Conclusions.

The various hyperfine interactions described in this chapter can be used to generate a predicted Mössbauer spectrum, with absorption lines at positions determined by those interactions. This spectrum can then be compared with an experimental one, to determine the values of the interactions in the physical system. Further information can be obtained from the line intensities in the spectrum, such as the orientation in space of the magnetic field and electric field gradient principal-axis directions (Gibb 1976).

Chapter 3

The theory of critical phenomena.

3.1 Introduction.

The study of critical behaviour, that is the behaviour of a system when it is close to a discontinuous change in its free energy, is a field that has advanced rapidly over the last few decades. Earlier mean-field techniques dating back to the 1930s are now being replaced by more sophisticated methods, especially renormalization group theory (RGT). Also the concept of universality has developed, describing the way many completely different systems exhibit similar critical behaviour (Ma 1976).

However the simple nature of the mean-field theories and the fact that the predictions of RGT become inadequate as physical systems move away from criticality means that mean-field theory continues to be widely used (Ma 1976). This chapter will concentrate particularly on the critical behaviour and phase diagrams of magnetic systems, the topic of this thesis for the $Fe_xNi_{1-x}Cl_2$ system. Specifically we deal with random mixtures of compounds with competing magnetic anisotropies, a subgroup of a general class of systems which have come under particular study over the last two decades, that of systems with competing interactions. Each compound in the mixture has its own value and kind of magnetic anisotropy and spin, which affects the orientations of spins on neighbouring compounds via the quantum-exchange interaction. The anisotropy trying to line up a certain spin along its easy (i.e. minimum energy) axis competes with the exchange interaction which tries to align that spin parallel (anti-parallel) to neighbouring spins, in the case of ferromagnetism (antiferromagnetism).

This chapter describes the modern theories of critical phenomena in sections 3.2, 3.5 and 3.6 and their applications to mixed magnetic systems

in sections 3.3 and 3.8. Numerical modelling is discussed in section 3.9.

3.2 Mean-field theory.

Mean-field theory is based on the assumption that the effect on one particular part of a system by the remaining parts can be accurately expressed by representing those other parts by their thermal averages. Consider the case of a mixture of several different atomic species which form a simple mixed magnetic system which can be represented by the Heisenberg model Hamiltonian

$$\mathcal{H}_i = -2 \sum_j J_{ij} \boldsymbol{S}_i \cdot \boldsymbol{S}_j. \tag{3.1}$$

$\boldsymbol{S}_j$ represents a spin which interacts with $\boldsymbol{S}_i$ with the sum over j taking into account all interacting spins, and J_{ij} is the exchange coupling constant between the spins (Hook and Hall 1991). In mean-field theory the spins $\boldsymbol{S}_j$ are replaced by $<\boldsymbol{S}_j>$, their thermal averages. All spins belonging to the same atomic species are assumed for simplicity to have the same thermal average. An effective field is then defined (Smart 1966) which replaces the exchange interaction and interacting spins $\boldsymbol{S}_j$ by an equivalent magnetic field (often termed a molecular field) via

$$\mathcal{H}_i = -g\beta \boldsymbol{S}_i \cdot \boldsymbol{B}_e. \tag{3.2}$$

where g is the g factor for the atom or ion in question, and β is the Bohr magneton. This Hamiltonian for the spin $\boldsymbol{S}_i$ is equivalent to equation 3.1, where the effective field $\boldsymbol{B}_e$ is given by

$$\boldsymbol{B}_e = \frac{2}{g\beta} \sum_j J_{ij} <\boldsymbol{S}_j> . \tag{3.3}$$

Extra terms can be added to equation 3.2 to describe magnetic anisotropy or any other interactions.

The energies for particular orientations of the spin S_i can then be found from equation 3.2 for each atomic species, allowing the thermal average of S_i to be found (in terms of the spin averages of the neighbouring spins). Solving the resulting equations then gives the thermal averages for each atomic species, allowing phase diagrams for the system to be constructed (Smart 1966). Mean-field theory does have serious limitations. As the temperature T approaches its critical temperature T_c, thermodynamic quantities describing a spin system fluctuate strongly about their mean values, with spins fluctuating in a closely correlated way. Since mean-field theory describes the behaviours of spins in terms of interactions with only a small number of spins (typically their nearest or next nearest neighbours only) it cannot describe the long range correlations of spins which are observed experimentally (Ma 1976). In fact mean-field theory assumes each spin belonging to the same atomic species has the same thermal average, hence is completely correlated, at all temperatures. This assumption of mean-field theory is always a problem, since even for random mixtures different spins will have a different local environment with different numbers of each species surrounding them, and hence cannot have the same thermal average.

More complex theories have been devised to take these spin fluctuations into account with the most widely used being RGT. However the predictions of RGT become inaccurate far from phase lines and points. The region of a phase diagram where RGT can usefully be applied is called the critical region, and that region can be calculated (Ma 1976). However, this region tends to be very small. For example, the critical region in the $Fe_{1-x}Co_xCl_2$ system has been calculated to be restricted to temperatures within 10^{-5} K of the tetracritical point for the system (Wong $et\ al$ 1983).

3.3 Mean-field theory applied to systems with competing magnetic anisotropy.

Someya (1982) derived the phase diagram for $Fe_{1-x}Co_xCl_2$ which is a random mixture of the antiferromagnets $FeCl_2$ and $CoCl_2$. $FeCl_2$ has uniaxial anisotropy (along its c axis) while $CoCl_2$ has anisotropic exchange leading

to order in the plane perpendicular to the easy axis of FeCl$_2$ (the xy plane). Assuming the exchange constants took their pure compound values even in the mixture, Someya derived the thermal averages of the spins obtaining a phase diagram with four distinct phases, as shown in figure 3.1.

A tetracritical point forms a junction between the four different phases. Of particular interest is the oblique phase, where the spins on average align at an angle to both the c axis and the xy plane. This angle (different for the two different species) depends on the relative concentration of the two compounds and the temperature, and tends towards the easy axis (or plane) of whichever compound dominates. A similar prediction was derived by Matsubara and Inawashiro (1977) where they described a theoretical random mixture of antiferromagnets with magnetic anisotropy described via anisotropic exchange only. They also used mean-field theory to generate a phase diagram for the $Co_xFe_{1-x}Cl_2 2H_2O$, system, which compared well with experiments (Matsubara and Inawashiro 1979). A more recent study performed by Mano (1990) also gave equivalent results.

Igel et al (1990) studied the $Fe_xNi_{1-x}Cl_2$ system using mean-field theory, and generated a magnetic phase diagram which agreed well with faraday-rotation experiments. However, they did not investigate the mixed phase for the case where no external magnetic field is present.

3.4 Modern theories of critical phenomena.

Since the most important modern theory, RGT, grew out of the homogeneity hypothesis of critical phenomena, that theory will be described first. RGT will then be described, with its predictions for mixed magnetic systems. A physical justification for RGT will be given in the next subsection.

3.4.1 Scale invariance of systems at critical points.

The modern theories of critical phenomena are based on the observation that physical systems become scale invariant as a critical point is reached. This invariance is a consequence of the fluctuations of order parameters away from their average values. As temperature increases, fluctuations are

Figure 3.1: Phase diagram for the mixture $Fe_{1-x}Co_xCl_2$. There are four phases present, where spins can (I) lie along the c axis, (II) be in an oblique phase, (III) lie in the xy plane or (IV) have no mean magnetisation. Reproduced from Someya (1982).
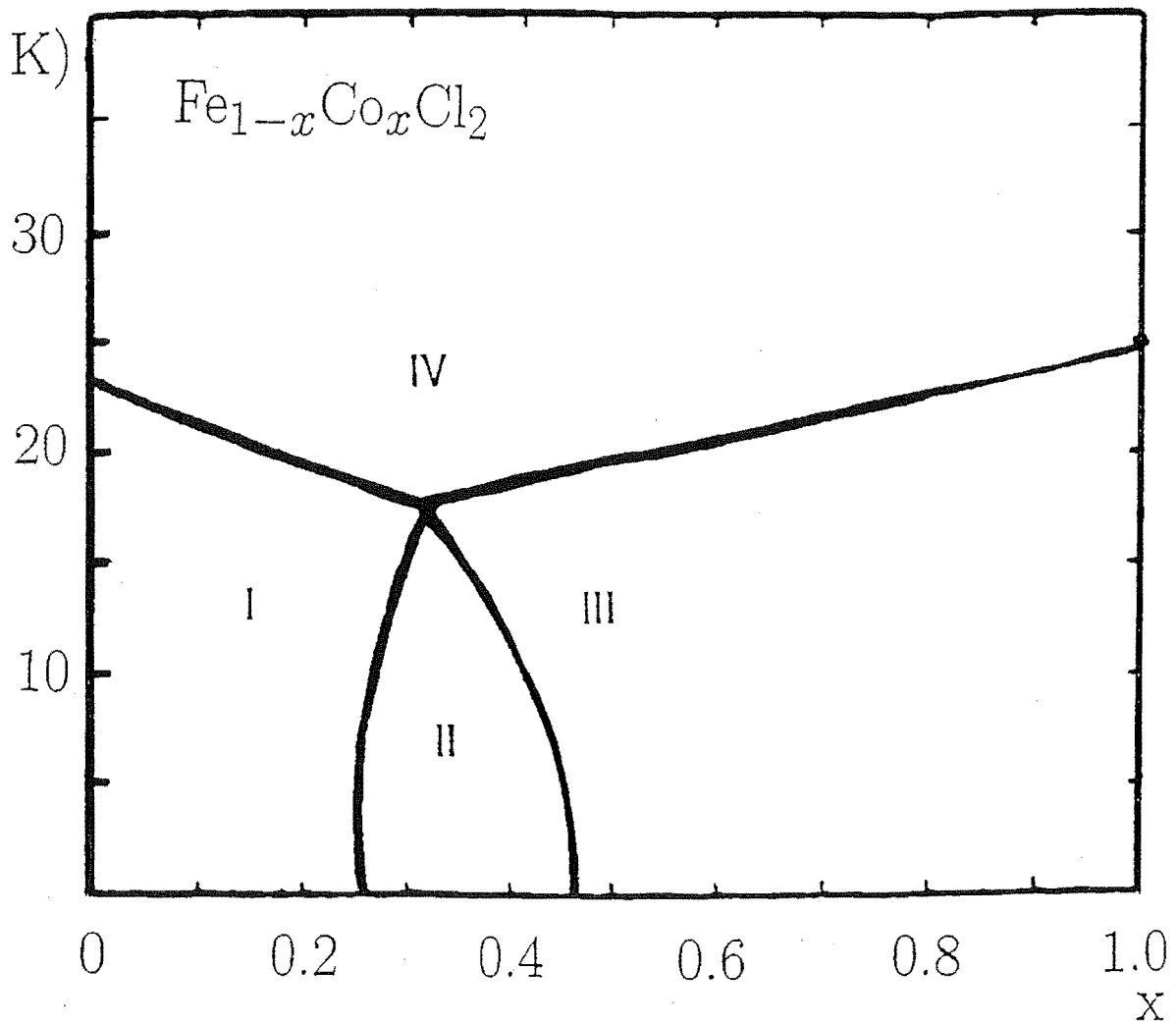
increasingly likely, since their thermodynamic Boltzmann factor increases. In particular, long wavelength fluctuations become common. In the case of magnetic systems of spins, these large scale fluctuations will correlate spins at large distances, even if the actual interactions in the system are of short range only. If block spins are then defined (as described in section 3.6) to describe spin order over large scales, scale invariance exists, as the block spins are now closely correlated over large distances, behaviour which also exists at smaller length scales between distant individual spins. As the critical temperature is reached, the fluctuations can span the entire system, leading to scale invariance at all length scales (Amit 1984). The spin configuration at any time will show small fluctuations within bigger ones, and averaging the configurations over time lead to identical average spin configurations at all length scales (Bellac 1991).

As discussed in section 3.2, mean-field theory cannot describe fluctuations in order parameters, which become increasingly important as the critical temperature is approached. However, in the case of a system with more than 4 spatial dimensions, or with infinite range interactions between spins, the mean-field description becomes exact (for systems with 3 order parameters, like the metal ion spins of $FeCl_2$ or $NiCl_2$) (Binney 1992).

Scale invariance will be discussed further in section 3.6.

3.5 The homogeneity hypothesis.

As the critical temperature T_c is approached thermodynamic quantities can be represented via critical exponents in terms of powers of $(T - T_c)$ with $T < $ or $> T_c$. For example the heat capacity C is given by

$$C \propto (T - T_c)^{-\alpha}$$

(Amit 1984).

An important quantity in the study of critical phenomena is the spin correlation function Γ, which describes the extent to which spins align relative to one another on average. The function is defined by

$$\Gamma(x_i - x_j) = < (S_i - < S_i >) \cdot (S_j - < S_j >) > \qquad (3.4)$$

where $x_i - x_j$ is the distance between two spins (S_i and S_j) and $<>$ represents the thermal average (Lawrie 1990). The quantity $S_i - <S_i>$ represents the fluctuation of spin S_i from its thermal mean (similarly for spin S_j). If two spins are always aligned then $\Gamma = 1$; if uncorrelated, Γ will tend to zero.

Γ can also be written in the form

$$\Gamma(q, h, T - T_c) = b^{2y}\Gamma(bq, b^{y_1}h, b^{y_2}(T - T_c)) \qquad (3.5)$$

with $|q|$ small, where h is a magnetic field (if it exists) and q is a Fourier variable (physically, a vector in the reciprocal lattice space of the system) where

$$S(q) \propto \int d^D x \exp(-iq.x)S(x) \qquad (3.6)$$

and

$$\Gamma(x) \propto \int d^D q \exp(iq.x)\Gamma(q) \qquad (3.7)$$

gives the relationship between Γ in x and q space (Ma 1976 and Wilson and Kogut 1974). D in equations 3.6 and 3.7 represents the spatial dimension of the crystal (which is usually a three dimensional structure) and the reciprocal lattice space. The variables b, y, y_1 and y_2 are constants to be determined. Equation 3.5 defines the homogeneity hypothesis. Manipulation of this equation gives the critical exponents and relationships between them, which compare very well with exponents derived from experimental studies (Ma 1976).

The homogeneity hypothesis has a physical justification in RGT.

3.6 Renormalization group theory.

The key idea in RGT is to study a system at different length scales where it is found that as a system approaches criticality the laws describing the system become scale invariant; the Hamiltonian remains the same independent of which length scale is used to study the system. In a magnetic system such as a ferromagnet, the Hamiltonian involves spin variables, and, looking at the system at different length scales, means defining a block spin for a block of lattice sites. A typical definition is

$$S(\text{block}) = \sum_i S_i \qquad (3.8)$$

where the variable i labels the spins contained within a block. A new (block) Hamiltonian is constructed, as a function of the (block) spins, but of the same form (e.g. the Ising model) as the original Hamiltonian. The spins are then rescaled via $S(\text{block}) \rightarrow \alpha(ab)S(\text{block})$ where a block size of ab is used with lattice constant a, and b is a positive integer. $\alpha(b)$ is an arbitrary function of b, allowing the block spin magnitudes to be arbitrarily set. Distances are rescaled via $x \rightarrow (1/b)x = x'$ (Ma 1976) so that the size of the blocks measured in the new length scale x' is equal to the lattice constant a.

Effectively the system has been viewed through a 'microscope' such that only degrees of freedom for large portions of the system are seen (the block spins). The lattice itself looks the same due to the length rescaling. The combination of defining a block spin, rescaling lengths and spins is called a (real space) renormalization group transformation (Wilson and Kogut 1974).

Figure 3.2: The Hamiltonian coefficient space. The variables g_i are the coefficients appearing in an arbitrary Hamiltonian. Shown is a theoretical critical surface with a pathway representing successive applications of renormalization transformations, driving the initial set g_i at the starting point s towards a fixed point.
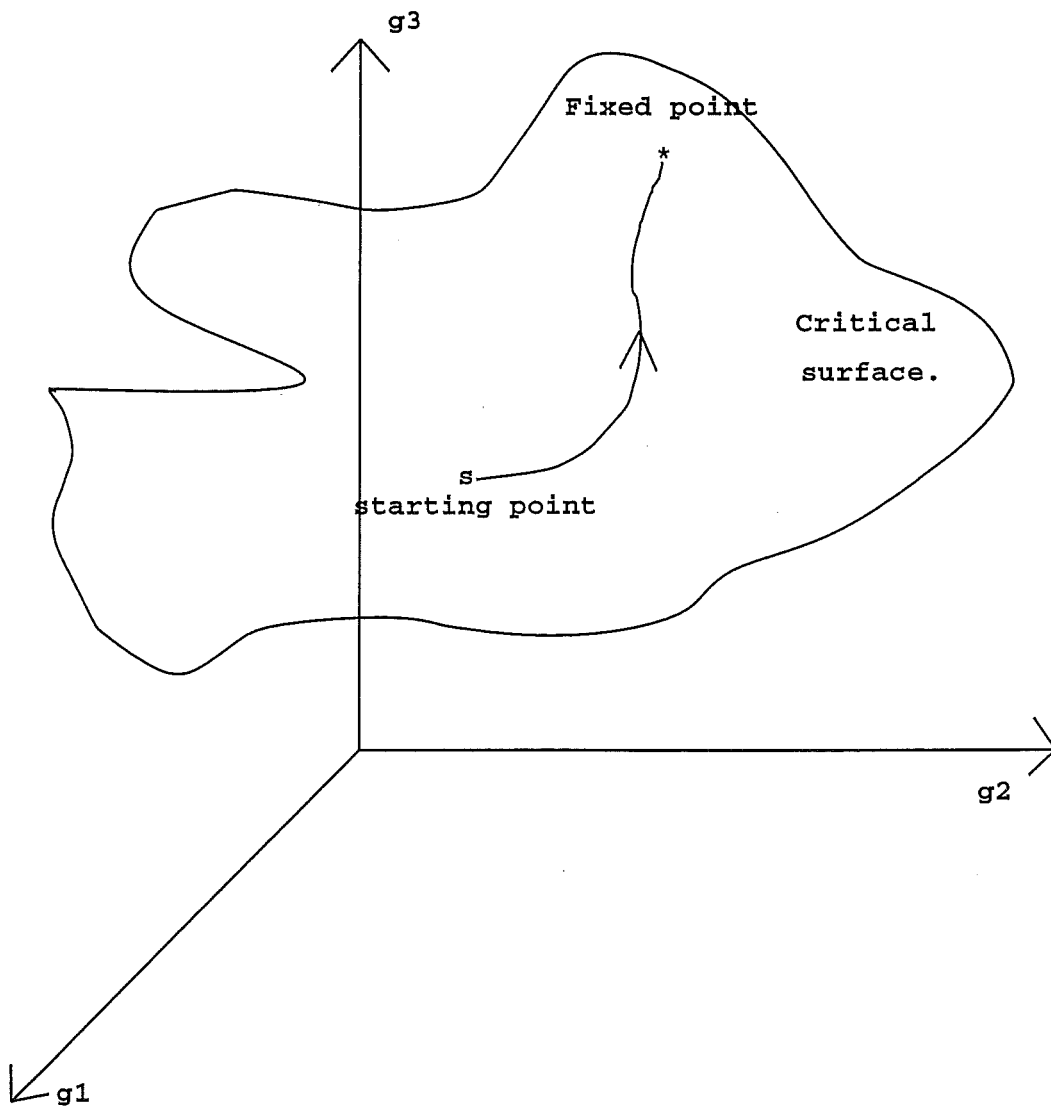
If renormalization group transformations are done one after another, fixed point behaviour is reached which means that the coefficients in the Hamiltonian remain the same after further transformations are performed;the system looks the same at all higher length scales. The values of the coefficients which remain invariant can be used to graphically define a fixed point in a space whose axes are defined by those coefficients, as illustrated in figure 3.2.

If we represent the set of coefficients in the Hamiltonian by μ, and the renormalization group transformation by an operator R_b, then we write the fixed point behaviour as

$$\mu^\star = R_b \mu^\star \qquad\qquad (3.9)$$

where $\mu = \mu^\star$ at the fixed point, which from equation 3.9 is unchanged under R_b. The region in parameter space within which R_b takes μ to $\mu^\star$ is called the critical plane. This is also illustrated in figure 3.2. Any particular physical system could have many fixed points (Wilson and Kogut 1974). Every system also has a critical region in its phase diagram, where the system is scale invariant for a finite number of renormalization transformations. Far from this critical region, the predictions of RGT become more difficult to calculate, and mean-field theory gives an adequate description (Ma 1976).

Renormalization group transformations are often performed on physical systems with Hamiltonians rewritten in terms of Fourier variables as used in equations 3.6 and 3.7. Instead of creating block spins we integrate out certain of the $S(q)$ degrees of freedom (the Fourier transforms of the spins), leaving Hamiltonians describing a more restricted group of $S(q)$. This process can be shown to be equivalent to blocking spins as described above (Ma 1976).

Critical exponents are derived by studying the behaviour of μ near $\mu^\star$ under the action of R_b, as described by Ausloos and Elliot (1983). We consider μ near $\mu^\star$, and expand as follows

$$\mu = \mu^\star + t_1 E_1 + t_2 E_2 + \ldots\ldots = \mu^\star + \delta\mu \qquad (3.10)$$

where E_i are eigenfunctions of R_b such that

$$R_b E_i = \lambda(i) E_i. \qquad (3.11)$$

Then

$$R_b\mu = \mu^\star + R_b\delta\mu = \mu^\star + t_1 b^{y_1} E_1 + t_2 b^{y_2} E_2 + \ldots\ldots \qquad (3.12)$$

where b^{y^i} are the eigenvalues of E_i. The variables t_i are real numbers. Depending on the signs of y_i, certain variables under the transformation R_b become irrelevant. For example, after many applications of R_b a coefficient $b^{y^i} \to 0$ if $y_i < 0$. Thus only certain t_i's, which in the case of simple magnetic systems are $(T\text{-}T_c)/\ T_c$ and the magnetic field h, remain of any importance in describing the behaviour of μ after many iterations of R_b. The correlation function can then be written as

$$\Gamma(\mathbf{q}, \mu^\star + t_1 E_1 + t_2 E_2 + \ldots) = b^{2y}\Gamma(b\mathbf{q}, \mu^\star + t_1 b^{y_1} E_1 + \ldots) \qquad (3.13)$$

for $|q|$ small. RGT has thus derived the homogeneity relation, which has the same form as equation 3.5 with the variables t_i chosen as above, which previously had no theoretical justification.

It should be noted that scale invariance implies large scale correlated fluctuations of spin order, as seen experimentally as T approaches T_c , hence RGT can account for experimentally observed behaviour that mean-field theory cannot.

Because irrelevant terms scale away when a system is rescaled, many different systems have the same critical behaviour; all they need is the same or similar fixed points (and set of eigenvalues and eigenvectors for R_b), which

lead to the same homogeneity relations and therefore critical exponents. This important phenomenon is known as Universality (Ma 1976). Systems as different as liquids, magnetic systems and binary alloys can have the same fixed points. The different kinds of systems need a similar Hamiltonian (in form) and the spatial dimension d and order parameter dimension n must be the same, to possess the same critical behaviour. That is, universality classes (classifications of systems according to d, n) exist. Systems of a particular class described at the lowest length scales exist on the same critical plane.

The task of RGT is to find the fixed points E_i and eigenvalues λ_i thus deriving the critical behaviour and universality classes. This brings out similarities between completely different systems; a quest for symmetry and order, which is common in physics.

3.7 Field theoretical description.

Field theoretical descriptions provide the most mathematically rigorous form of RGT. These descriptions of spin systems use a field to represent the magnetisation at different spatial points (strictly speaking, the mean magnetisation for a small volume about a point). A Hamiltonian is then written which determines the behaviour of this field (Binney *et al* 1992):

$$\mathcal{H}(\phi(\boldsymbol{x})) \propto \int d^d x (\frac{1}{2}\alpha^2(\nabla\phi)^2 + \frac{1}{2}\mu\phi^2 + \frac{1}{4!}\lambda\phi^4) \qquad (3.14)$$

where the integral is taken over the volume of a system of spins (of spatial dimension d). This Hamiltonian (known as the Landau-Ginzberg model) is identical in form to the one defining the $\lambda\phi^4$ theory of particle quantum field theory, where the first term in equation 3.14 is a 'kinetic' term, the second a mass term (where μ is the mass) and the final term (with coupling constant λ) describes particle interactions between spin-less interacting particles (Ramond 1981). However, in that case, the field ϕ represents an operator which creates states with particles at particular places from the

vacuum state which has no particles and the integral is over four dimensional spacetime. Since the mathematical methods used in field theoretical statistical mechanics share much in common with those used in quantum field theory, the next section briefly describes them.

3.7.1   Calculational methods in quantum field theory.

The usual first step is to create a function Z, which is the sum of the probabilities for every possible field configuration. This is equivalent to the partition function of statistical mechanics. Propagator functions can then be defined as derivatives of the function Z with respect to source terms J (representing magnetic or other fields). These propagators are the probability amplitudes that a particle will propagate from one spacetime point to another. Propagators involving several particles propagating together can be formed which represent a variety of scattering processes. If the field description is transformed into a Fourier representation in terms of particle momenta, via for example a variable transformation like (Teller 1995)

$$\phi(x, t) = \int d^3 k e^{-i k \cdot x} a(k, t) \qquad (3.15)$$

then propagators can be formed that represent the probability amplitudes that particles of a certain momenta propagate. Here $a(k, t)$ is a creation operator that creates a state with a particle of momentum k from the vacuum state, and the integral is over all values for the particle momentum k. The propagators can be written as a perturbation series in the coupling constant λ leading to the well known Feynmann diagrams, each of which describe how a particle can propagate. Each diagram represents a numerical contribution to the total probability amplitude (a possible way) particles propagate, some involving the creation/annihilation of short lived (virtual) particles (Mandl and Shaw 1984).

A serious problem arises when the numerical contribution to the particle propagators represented by the various Feynmann diagrams are computed; many end up being infinite, which would seem at first glance to render the

theory useless. The terms in question can be written as a function of the expression

$$M = \mu - \int_0^\infty g(\mathbf{k})d\mathbf{k} \qquad (3.16)$$

where μ is the mass of the particles in question appearing in the Hamiltonian for the system (an example is equation 3.14). The integral term in equation 3.16 is infinite for several Feynmann diagrams.

The key to extracting useful information from these infinite expressions is to use an approach called renormalization. If the term M in expression 3.16 is taken to be the observable mass of the particles, then the Feynmann propagators will be finite. The mass μ is taken to be the 'bare' mass of the particle, which is the mass of a particle if no self interactions (of a particle with its own field) existed. The (infinite) integral expression in equation 3.16 is then a correction to the (infinite) bare mass μ, which takes into account the self interaction to give the observable (finite) mass M. The mass M is then set equal to experimental values of the particle in question. Effectively, we have defined the infinities in the theory away (Ramond 1981).

When this procedure is done results are obtained, which are very close to their experimentally determined values. For example the Lande g factor for electrons and Lamb shifts for simple atoms as calculated by quantum electrodynamics are extremely accurate (Ramond 1981). Such agreement clearly indicates the renormalization procedure (whether of mass as above or of other quantities such as charge in more complicated theories) is valid.

Even so, the procedure is still open to interpretation, especially the fact that mathematically in expression 3.16 we are subtracting one infinite quantity from another to get a finite quantity M, which would seem to be an impossibility. One way to remove this problem is to realise that in equation 3.16 at the higher values of k (which cause the infinities in the integral), the theory is not well defined; for example complicated expressions would have to be added to model the effects of gravity, which is an important interaction at very high energies (equivalent to large values of particle momentum k). Such corrections could render the integral finite, thus we would

be subtracting two finite quantities to get the observable mass M (Teller 1994).

3.7.2 The renormalization procedure applied to statistical mechanics.

The previous ideas from particle quantum field theory can be applied to statistical mechanics, where the field ϕ in equation represents not a particle creation operator but a measure of local magnetisation. Again propagator functions are derived, but this time they represent the spin correlation functions. So instead of representing the probability that a particle propagates from one spacetime point to another, the propagator functions indicate to what extent spins at particular spatial points line up together on average. More complicated propagator functions represent to what extent several spins align together on average, rather than describing complicated particle scattering processes as in quantum field theory.

Again the concept of renormalization proves valuable. An example is the calculation of the Fourier transform of the first Feynmann diagram for the second order correlation function Γ^2 (the correlation function between two particular spins) where

$$\Gamma^2(k) = \mu^2 k^2 + \alpha^2 + \frac{\lambda}{2} \int_0^L \frac{d^d q}{\alpha^2 q^2 + \mu^2}. \tag{3.17}$$

Here k and q are vectors in the reciprocal lattice space for the crystal, and the constants μ, α and λ are the constants from equation 3.14. The Fourier transform of the correlation function is given by

$$\Gamma^2(k) = \int_0^L d^d k e^{-ik.x} \Gamma^2(x) \tag{3.18}$$

where the vector x is a displacement vector between the two spins whose correlation we wish to measure. The upper limit, L, on the integral is termed a cutoff, and is not taken to infinity since it can be shown that the

smoothness of the field varies inversely with L; and the magnetisation field ϕ cannot vary on scales less than the lattice constant for the system (as the spins are located at lattice points). Field configurations that vary on a very small scale are not physical. As the cutoff is lowered, since the field will vary only over a large distance scale, we have an equivalent picture to the spin blocking method of studying systems near critical point, as discussed previously (see section 3.6).

This propagator is of particular interest since $\Gamma(\mathrm{k}= 0)$ is inversely proportional to the magnetic susceptibility of the physical system, and this can be measured. If the mass term μ is renormalized as follows

$$m = \mu^2 + \frac{\lambda}{2} \int_0^L \frac{d^d q}{\alpha^2 q^2 + \mu^2} \qquad (3.19)$$

then the expression for $\Gamma^2(k)$ reduces to $m^2 + \alpha^2 k^2$ which is a very simple result. Higher order Feynmann diagrams require a modified renormalization method but the principle is the same. The advantage of the renormalizing procedure is that is removes the cutoff L from the theory; various quantities calculated are then independent of scale, which is the phenomenon of scaling invariance existing in nature, as previously discussed.

3.8   Renormalization group theory applied to the case of random mixtures.

Arahony and Fishman (1976) and Fishman and Arahony (1978) set out the first rigorous RGT treatment of mixed systems with competing magnetic anisotropy. Their approach was based on the Hamiltonian

$$\mathcal{H} = - \sum_{ij} (J_{ij} S_i . S_j + D_{ij} [m_1^{-1} S_{i1} . S_{j1} - m_2^{-1} S_{i2} . S_{j2}]) \qquad (3.20)$$

where S_{i1}, S_{i2} are m_1 and m_2 dimensional components of the vector S_i

respectively. For example, $m_1=1$ if S_{i1} is chosen to be S_{iz} in a Cartesian axis system (a convenient choice if there is magnetic anisotropy along the z axis, for example). This Hamiltonian describes the case of magnetic anisotropy due to anisotropic exchange. The variables D_{ij} energetically favour alignment of the spins so that they only have the S_1 (for $D_{ij} > 0$) or S_2 ($D_{ij} < 0$) components non zero, depending on the identities of the compounds at sites i, j. The Hamiltonian was then rewritten in terms of Fourier vectors $S(q)$ and the fixed points and behaviour of the system near criticality were found, as discussed in section 3.6.

They concluded a 'decoupled' fixed point describes the system at the tetracritical point, where the two subsystems (the two compounds) order independently from one another. Effectively, the two compounds see each other as a non magnetic impurity. Of importance in this decoupling is the lack of long-range forces i.e. only short range isotropic and anisotropic exchange between nearest neighbours was modelled. Figure 3.3 reproduces the phase diagram derived from their RGT study.

As was found in the mean-field studies, below the fixed point is a mixed phase region, where both S_1 and S_2 order (are non zero simultaneously). But the phase diagram around the tetracritical point is smooth, as opposed to the kinked phase diagram predicted by mean-field theory.

Even though the Hamiltonian in equation 3.20 was specific to compounds with anisotropy due to anisotropic exchange, the results also apply to mixtures of compounds with single ion or planar anisotropy (Ausloos and Elliot 1983) such as the $Fe_xNi_{1-x}Cl_2$ system.

Other workers more recently studying mixed systems using field theoretical RGT got equivalent results, but did note that the lower phase transitions are not necessarily sharp (as found by Aharony and Fishman 1976, 1978) in the presence of random fields or off diagonal exchange interactions (Oku and Igarashi 1983).

Figure 3.3: Phase diagram for a mixture $(A_x B_{1-x})$ of compounds (A,B) with competing magnetic anisotropy. Reproduced from Arahony and Fishman (1978)
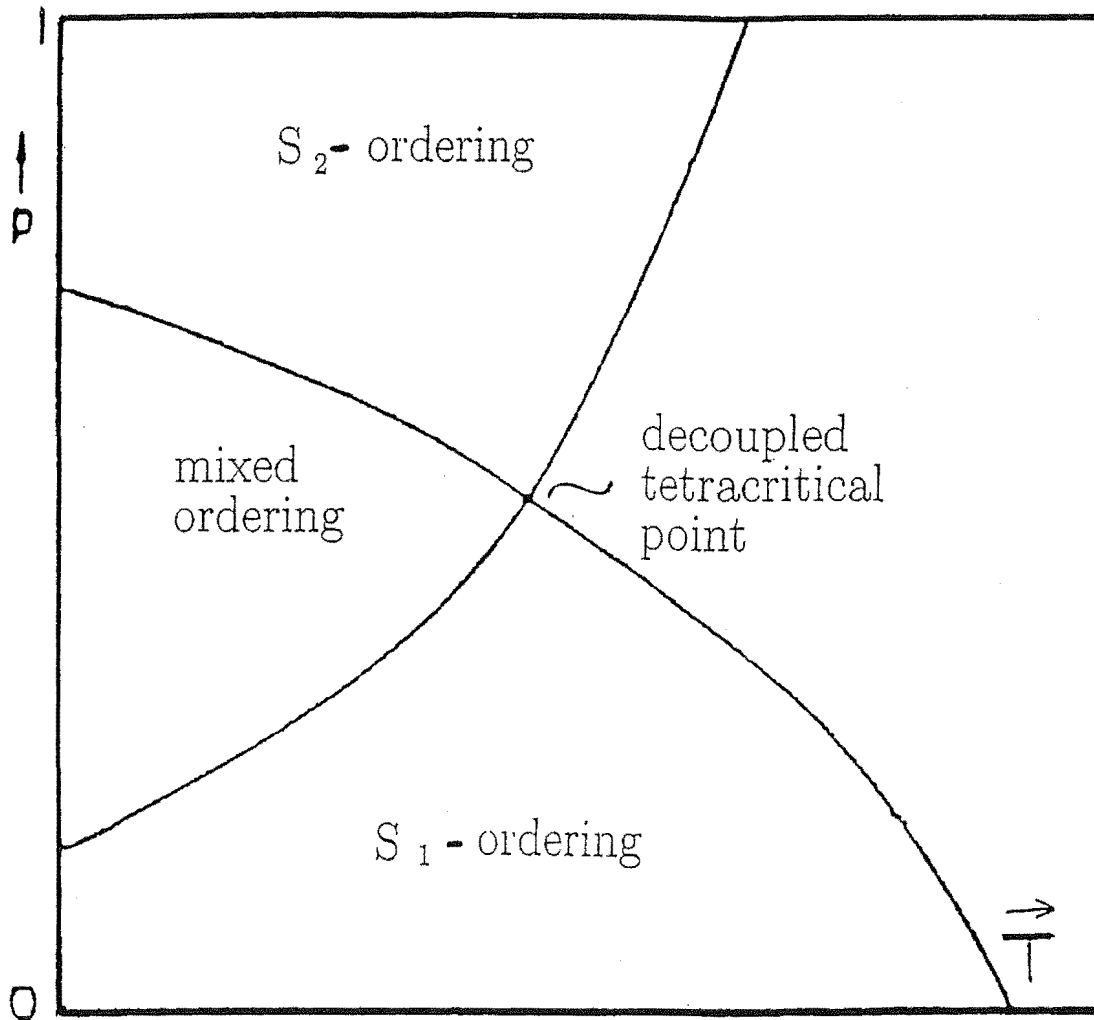
3.9 Numerical simulations.

3.9.1 The need for numerical simulations.

The theoretical approaches mentioned up to now all suffer from limitations which restrict their use in accurately modelling systems with competing order, which includes the mixed magnetic system of $Fe_xNi_{1-x}Cl_2$.

The basic assumptions of mean-field theory allow systems to be easily modelled, but the assumptions are not strictly valid. In the case of spins on different lattice sites interacting, each spin does not interact with the thermal average of neighbouring spins (represented by the *mean field*). Only if those other spins did not fluctuate much from their thermal average would this approximation hold. And individual spins do fluctuate significantly (except at very low temperatures) since the energies for different spin orientations are similar as exchange interactions and any magnetic anisotropy present are weak interactions.

Mean-field theory also assumes that the environment of each spin is identical, with the number of each ionic or atomic species in close proximity with the spins determined solely by their overall relative concentration in the mixture. This effectively removes the randomness from a mixed system such as $Fe_xNi_{1-x}Cl_2$. And the assumed uniformity of neighbouring spin identities also ignores the possibility that clusters of different species may occur in the real system, which may be responsible for the complex spin behaviour observed in the Mössbauer spectral data for the $Fe_xNi_{1-x}Cl_2$ system.

The more modern RGT also has limited applicability to mixed magnetic systems. As mentioned previously, the critical region in the phase diagram, where RGT is a good description, can be very small. This means the mixed phase behaviour which is of particular interest cannot be modelled adequately, as most of it is out of the critical region. In fact, most experimental studies of mixed magnetic systems do not show the decoupling of order parameters predicted by RGT. Systems which show this decoupling are rare (see for example Mook *et al* 1981 and Schobinger-Papamantellos 1981).

Clusters are also not easy to model with RGT. Previous models of mixed magnetic systems assumed a random distribution of ionic or atomic identity

at each lattice site (Aharony and Fishman 1976). This allows the problem to be readily solved, but lacks realism if clusters do form in the mixed system.

For these reasons, theoretical modelling of the $Fe_xNi_{1-x}Cl_2$ system was not attempted, since a *realistic* model would not be possible with either mean-field theory or RGT. And a realistic model is necessary to account for the complex behaviours that have been detected experimentally by Mössbauer and neutron diffraction studies of the system.

Therefore a numerical study of $Fe_xNi_{1-x}Cl_2$ was attempted, which allows the system to be realistically modelled and solved, since an exact analytical solution was not sought. Every possible known interaction could be included in the system's Hamiltonian, as well as any possible distribution of ions, including clusters of ions.

The following subsection describes the numerical modelling technique chosen (the Monte Carlo technique).

3.9.2 The Monte Carlo technique.

The Monte Carlo numerical technique refers to the use of random numbers to solve problems that are usually impossible or difficult to solve analytically (Sobol 1994). When the problem involves modelling systems of interacting spins, the usual approach involves generating arrays of numbers representing the spins or spin components, with appropriate terms to represent interactions between the spins, external magnetic fields, etc. Physical quantities of interest (such as magnetisation and magnetic susceptibility) can then be directly determined from the arrays of numbers.

The arrays of numbers must of course be chosen in such a way that their behaviour mimics the behaviour of real spins. Simply choosing configurations entirely at random (a *simple sampling* method) would lead to inaccuracy, since real systems have a tendency to exist in low energy states, rather than than occupying all possible states equally. What is required is *importance sampling*, where configuration states are considered in proportion to their true probability.

In the case where the physical system of spins is in equilibrium (which is the assumed case for the crystal samples that gave rise to the Mössbauer

data for the $Fe_xNi_{1-x}Cl_2$ system, quoted in this thesis) the probability that any particular configuration of spins exists on measuring the system can be written as

$$P(\mathbf{x}) = \frac{1}{Z} \exp\left(-\frac{H(\mathbf{x})}{kT}\right) \tag{3.21}$$

with

$$Z = \sum_{[All\ configurations]} \exp\left(-\frac{H(\mathbf{x})}{kT}\right) \tag{3.22}$$

where the expression $P(\mathbf{x})$ in equation 3.21 represents the probability that a particular configuration represented by $\mathbf{x}$ exists ($\mathbf{x}$ is in general a matrix with elements containing the spin components with respect to the spatial axes). Equation 3.21 contains the partition function Z, which normalises the probabilities to 1. $H(\mathbf{x})$ is the energy (or Hamiltonian) of the system of spins when in the state $\mathbf{x}$ and the quantities k and T are the Boltzmann constant and temperature (measured in Kelvin) respectively (Binder and Heermann 1992).

The importance sampling technique used in this thesis is based on the *Metropolis Algorithm* which generates a number of configurations in turn, each of which is derived from the previous one. Once an initial configuration has been chosen, some or all of the degrees of freedom (the spins) are altered to form a new configuration. This alteration consists of re-orienting each spin, in 3 dimensional space for spins in the $Fe_xNi_{1-x}Cl_2$ case. The energy of the system before and after the alterations are made is calculated, and the new configuration is accepted as a valid configuration for describing the physical system with a probability equal to

$$\exp\left(-\frac{\delta H}{kT}\right) \tag{3.23}$$

if the energy difference (final - initial configuration energy) denoted by δH is positive. It is selected as a configuration for sure if δH is negative. This ensures that the chance any particular configuration is chosen as a legitimate 'snapshot' of the system of spins is consistent with the Boltzmann distribution given by equation 3.21. The series of configurations chosen as valid descriptions of the system is termed a *Markov chain*, and the process of choosing them, a *Markov process*.

The thermal average $\bar{Q}$ of any quantity Q that depends on the spin configurations can then be easily calculated via

$$\bar{Q} = \frac{1}{Z} \sum_{[All\ configurations]} Q(\mathbf{x}) \frac{\exp(-H(\mathbf{x}))}{kT} \qquad (3.24)$$

where $Q(\mathbf{x})$ is the value of the quantity Q when the system has the spin configuration $\mathbf{x}$. The simplest such quantity is the average of the total energy, with the term $Q(\mathbf{x}) = H(\mathbf{x})$.

The Monte Carlo method does have limitations. It cannot follow spin behaviour as a function of time (dynamics), and there are problems with the Markov process itself. The various problems and their relevance to the Monte Carlo simulations of the $Fe_xNi_{1-x}Cl_2$ system which were carried out will be discussed in detail in chapter 7.

3.10 Conclusions.

While both mean-field theory and RGT offer useful theoretical frameworks for understanding mixed magnetic systems, both have limitations which do not allow them to accurately model the $Fe_xNi_{1-x}Cl_2$ system. For this reason the Monte Carlo numerical technique was chosen to model the system. The results from these simulations will be discussed in chapter 6.

Chapter 4

Techniques involved in the Mössbauer study of $Fe_xNi_{1-x}Cl_2$ crystals.

4.1 Introduction.

This chapter describes the experimental techniques used to produce single crystals of $Fe_xNi_{1-x}Cl_2$, and to measure their Mössbauer spectra.

4.2 Production of $Fe_xNi_{1-x}Cl_2$ absorbers.

4.2.1 Manufacture of $Fe_xNi_{1-x}Cl_2$ powders.

Analar powders of $NiCl_2$ were used. $FeCl_2$ with enhanced levels of ^{57}Fe was added, to guarantee strong Mössbauer absorption spectra. The following procedures were followed for each crystal made.

First, a small amount (typically 3-5 milligrams) of ^{57}Fe metal was placed into a beaker containing pure HCl and distilled water, and the contents stirred for 24 hours by a (heated) magnetic stirrer. After this time the ^{57}Fe had dissolved completely, creating $^{57}FeCl_2 \cdot 4H_2O$. Analar Powders of $FeCl_2 \cdot 4H_2O$ and $NiCl_2 \cdot 6H_2O$ were then added and stirred until dissolved. The solution dried in a vacuum system to remove excess water and remaining acid (which was unattached to metal atom complexes).

The resulting mixture was then placed into a long glass tube, inserted into a heater set to 400 C. This removed much of the remaining water from the Fe and Ni compounds, since they decompose at 250 K and 350 K respectively.

During the drying process, N_2 gas and HCl gas was passed through the tube, to sweep away any vapourised water. The HCl gas inhibited oxidation

of divalent ^{57}Fe to Fe^{3+} in the form of $FeCl_3$, and the inert N_2 insured the atmosphere inside the tube was constantly flowing through the open end, hence sweeping out the water vapour.

Finally, the dried powder (which was orange coloured from the presence of $NiCl_2$ and relatively little $FeCl_2$) was placed in a quartz tube which was evacuated, and heated for a day at 370 C to insure last vestiges of water were removed. The transfer of the powder into its tube was rapid, since $FeCl_2$ is highly hygroscopic. This baking temperature of 370 C removed any $FeCl_3$ that was still present as this evaporates at 306 C (CRC 1997). It was sublimated under vacuum heating of the sample.

4.2.2 Growing single crystals of $Fe_xNi_{1-x}Cl_2$.

The prepared dehydrated powder was then sealed in its quartz tube for placing into a Bridgemann furnace. The tubes terminated in a small bulb with a sharpened point, to promote the growth of adequate size single crystals. If several single crystals grew from the pointed end, only one would enter the main body of the tube because of the narrow neck separating the bulb from the rest of the tube.

The Bridgemann furnace was heated just above 1000 C to melt both compounds since $NiCl_2$ melts at 1001 C, while $FeCl_2$ melts at 670 C (CRC handbook). No temperature probe was available for 1000 C, so the temperature profile of the Bridgemann furnace for a setting of 900 C was determined, and is shown in figure 4.1, and would be similar in shape to the 1000 C profile.

The quartz tubes were small enough to be lowered into the very hot central region of the profile (where temperatures are greater than 1010 C), ensuring that the powder was everywhere melted and hence avoiding multiple seeds points forming which would have led to several coexisting single crystals growing. The tubes had the pointed ends facing down and were lowered through the temperature gradient at a rate of 1.1 $mm\,h^{-1}$.

Figure 4.1: Bridgemann furnace temperature profile at 900 C.
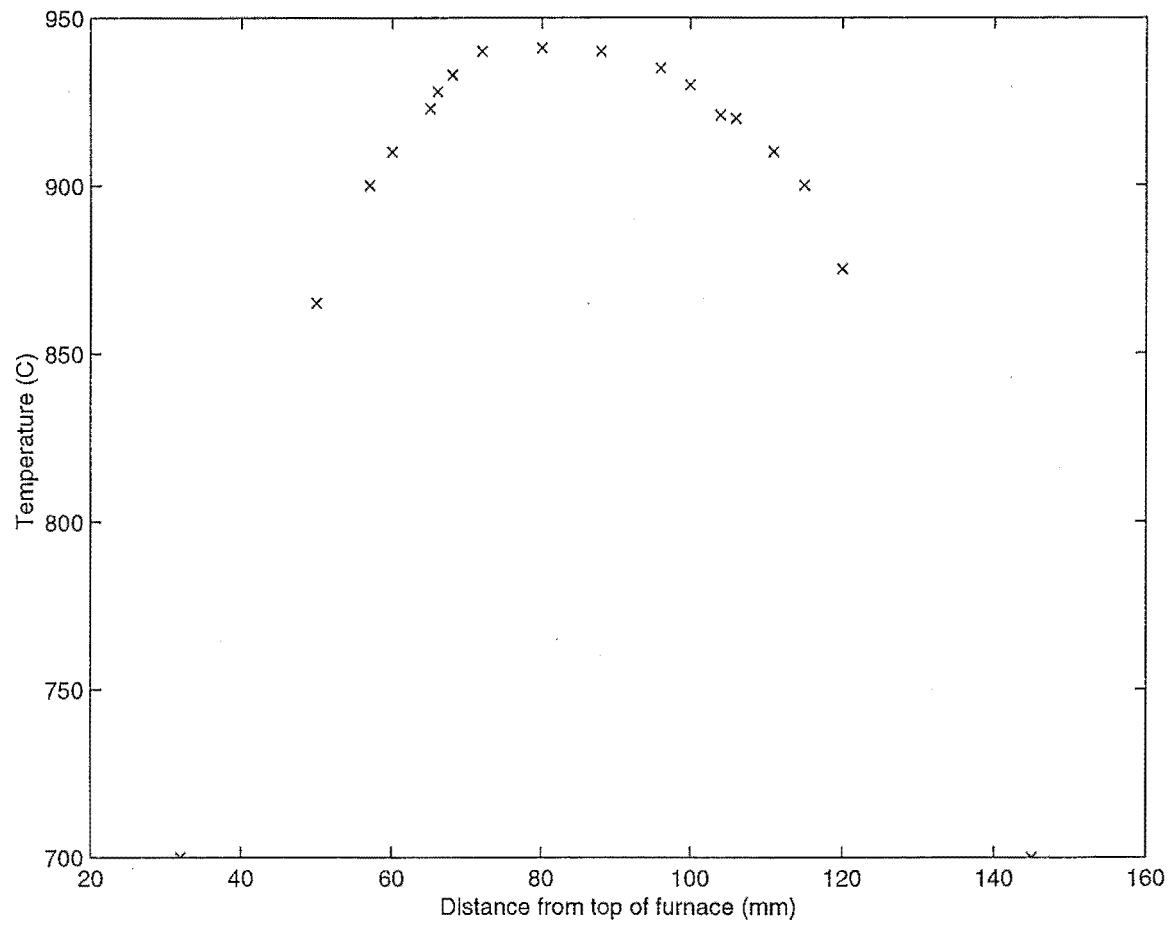
The single crystals produced varied in quality and usability. Several were polycrystalline rather than single crystals, rendering them useless. Even the single crystals had concentration gradients within a cross-sectional sample of a given crystal.

4.2.3   The production of Mössbauer absorbers.

The single crystals studied by Mössbauer spectroscopy are listed in table 4.1, which includes the nominal and actual Fe content of the crystals. Also displayed are the experimentally measured equivalent amounts of natural Fe per square centimeter, that is, the amounts of natural Fe that would provide the same area densities of ^{57}Fe. The actual Fe content was analysed by electron diffraction by the Department of Electrical and Electronic engineering, University of Canterbury, New Zealand. It is apparent that Fe levels in the listed crystals were significantly lower than expected; possibly many Fe atoms had segregated to either end of the crystal.

Nominal Fe concentration x	Actual Fe concentration.
0.08	0.031 [1.1]
0.09	0.052 [3.5]
0.25	0.15 [1.5]

Table 4.1: Fe content of the $Fe_x Ni_{1-x} Cl_2$ absorbers. The numbers in square brackets are the equivalent amounts of natural Fe (in mg per square centimeter).

4.2.4 Final preparation of the Mössbauer absorbers and the cooling procedure followed.

Mössbauer absorbers were created by cleaving fragments off the face of the crystalline samples of $Fe_xNi_{1-x}Cl_2$ grown, using a razor blade. Cellotape-stripping methods proved inadequate as the resulting crystal fragments were so thin that the resulting signal-to-noise ratio in the Mössbauer spectra was very low, giving low quality spectra. The sizes of the crystals grown (and the fact that even good single crystals had only small regions with smooth surfaces for easy cleavage) meant that small fragments were used from the same part of a given crystal.

The absorbers were overlaid with a lead shield, to prevent γ-rays passing through small gaps between adjacent crystallites, which decreases the signal to noise ratio. Even so, it proved impossible to completely eliminate this leak-through problem.

Finally the absorbers were mounted in a cryostat through which cold liquid cryogen was drawn to achieve the desired absorber temperature. Liquid N_2 and He was used for the high temperature ($T > 50\,K$) and low temperature runs respectively (down to $4.2\,K$). Exact temperature control was difficult, with an uncertainty in the temperatures of $\pm 0.2\,K$ for most temperatures, increasing to $\pm 0.3\,K$ for 4.2 to $15\,K$.

4.3 Mössbauer studies of the $Fe_xNi_{1-x}Cl_2$ absorbers.

4.3.1 The Mössbauer apparatus and basic experimental procedures adopted.

The Mössbauer absorbers were placed in a cryostat, in a stationary position. The Mössbauer spectrometer was manufactured by Ranger Scientific incorporated, and consisted of a VT 900 velocity transducer which moved the radiation source relative to the absorber in a triangular saw-toothed pattern of velocities, both away and towards the absorber. A PA 900 proportional counter placed behind the absorber (away from the source) counted the radiation detected in particular velocity intervals (divided into 1020

channels). The output from the PA 900 counter was sent to an Apple IIe computer. The entire apparatus was vibration insulated to minimise any vibrational broadening, so that only γ-ray energy modulation due to the velocity transponder was present. The apparatus was aligned (to an accuracy of 3-5°) so that γ-rays from the source would be incident at right angles to the crystal planes of the absorbing material.

Since the radiation source is more intense when closer to the detector, the resulting background counts were different for different channels. This was corrected for by adding the channel counts for the same velocities (which occur twice per transponder cycle) together, which led to a constant baseline independent of the channel (velocity). This folding procedure was repeated for every spectrum recorded.

The source was ^{57}Co in a Rh matrix supplied by Amersham. This decays into stable ^{57}Fe with a half-life of 270 days (Wertheim 1964). The 14.4 keV γ-rays emitted came from a transition between chemically-unsplit excited and ground states, making the source profile a simple Lorentzian shape. However, other source and matrix γ-rays and X-rays were present and these increase the background readings of radiation detected at each velocity channel without creating any absorption lines, and hence decreases the signal to noise ratio. To reduce this background the levels of the discriminator were set to select the 14.4 keV Mössbauer γ-rays.

There was a small amount of ^{57}Fe impurity in the front window of the PA 900 detector, which resulted in two small lines in any Mössbauer spectrum taken. These were subtracted from all spectra during analysis. The fraction of Mössbauer γ-rays (and those that are detected by the PA 900, but come from other transitions) was determined by placing a thin (0.13 mm thick) copper shield in front of the detector, which blocked out the Mössbauer γ-rays but allowed most of the higher energy photons to pass through (95.25%). The total γ-ray flux was then measured over a 100 second period, and compared with the case where the copper shield was absent. This gives the ratio between the Mössbauer and other γ-rays present for the entire Mössbauer experiment. This process was repeated for every Mössbauer measurement.

The velocity scale was calibrated with respect to the spectrum of iron foil. This was done by taking a spectrum of the Mössbauer iron-standard SRM No. 1541 (supplied by the National Bureau of Standards, US department of Commerce), which has calibrated lines at known velocities. These calibration spectra were taken every few Mössbauer measurements, typically at the start and end of a sequence of several studies and determined the channel to be used for folding the spectra. Isomer shifts were quoted relative to the centroid of the standard iron foil line positions.

4.3.2 Fitting the spectra to determine Mössbauer observables.

Once the Mössbauer spectra were recorded they were fitted with Lorentzian shaped lines using a least squares routine. The fitted quantities could be set seperately for each absorption site, and were as follows (with quantities and symbols defined as in chapter 2);

(a) α and β, the angles between the direction of the incoming γ-rays and the z and x axes of the principal axis system respectively;

(b) B_{hf}, the magnitude of the total hyperfine magnetic field at the nucleus;

(c) $EQVZ2 = \frac{1}{2}|e|QV_{zz}$;

(d) η, the asymmetry parameter;

(e) θ_{hf} and ϕ_{hf}, the angles between the total hyperfine magnetic field at the nucleus and the z and x axes of the principal axis system respectively;

(f) IS, the Isomer shift;

(g) Γ, the halfwidth (in mm/s) of the absorption lines

(h) and D, the dip, a quantity measuring the depth of the absorption site

(relative to the background count).

The specific values for the quantities (a) - (h) used to model the Mössbauer spectra obtained for this thesis, and the restrictions placed on them, will be described in chapter 5.

The computer programs used to compare experimental with simulated spectra were SINGLE and MOSCOR, based on original code by D H Jones of Liverpool University and J B Ward while on leave at Portland State University, respectively. SINGLE calculated simulated spectra using the quantities (a) - (h), which could be fixed or allowed to vary. The program simulated spectra appropriate for absorption sites from a single crystal sample, and could simulate paramagnetic or magnetic spectra. The line shapes simulated were Lorentzian, which are consistent with experimental line shapes in the limit where a very thin Mössbauer source and absorber sample are used (Gibb 1976).

The program MOSCOR compared the simulated spectra with the experimental ones, which were inputed from a seperate data file. The program varied quantities from the list (a) - (h) (or a restricted set chosen by the user) and perfomed a least squares fit, using the reduced χ^2 statistical test to measure the goodness of fit between the calculated and experimental spectra. When the goodness of fit could no longer be improved, the final values of the fixed and varied quantities were stored in a further data file. The program also calculated the relative areas of the absorption spectra due to different absorption sites.

Chapter 5

A Monte Carlo simulation study of the $Fe_xNi_{1-x}Cl_2$ system.

5.1 Previous Monte Carlo studies of mixed magnetic systems.

In 1978 Inawashiro simulated the magnetic behaviour of the system A_xB_{1-x} consisting of a mixture of two anti-ferromagnetic species A and B of spin 1 with magnetic anisotropy due to anisotropic exchange (Inawashiro 1978). The spins were randomly sprinkled about a 2D square lattice with 20 sites to a side and had perpendicular easy axes with the same magnitude of anisotropy. The spins were treated semi-classically in that they were allowed to orient themselves in space in a classical way, but with the quantum mechanical exchange interaction contained within the Hamiltonian. Spin averages of the spins at each separate lattice site were obtained and the usual four phases predicted by mean-field theory and seen in many experiments were produced. Since the magnitudes of the anisotropy constants for the different species were the same, the mixed phase occurred about a tetracritical point at $x=0.5$.

In that phase, local clusters of A and B atoms created coexisting populations of atoms with different spin behaviours, with high A content clusters forcing local spins to align on average close to the easy axis for the A atom, similarly for clusters with many B atoms. Such clusters dictated the outcome since they were relatively large and common throughout the lattice. This was because the concentrations within the mixed phase were all close to $x=0.5$, hence both species were equally numerous and, by random chance, clusters of either species often formed. These results are highly reminiscent

of the spin behaviours found in $Fe_xNi_{1-x}Cl_2$. However they were clearly tied to the presence of relatively large clusters of high A or B concentration, which do not occur very often in a sample of $Fe_xNi_{1-x}Cl_2$, since the tetracritical concentration is then at $x=0.09$, for which the Fe^{2+} ion is relatively rare. Hence clusters of Fe^{2+} ions are relatively few.

Their results can be compared to those of Aplesnin (1988) who modelled on a 30 by 30 square lattice a theoretical mixture of two antiferromagnets with a perpendicular easy axis and easy plane, and again the same exchange constants. In the case where the exchange and anisotropy constants were similar in magnitude, the intermediate region was an oblique phase with some spins aligned along the easy axis or easy plane.

Kato (1994) studied the random mixture $CsMn_{1-x}Co_xCl_3.2H_2O$. In this system competition exists between the strong axial single-ion anisotropy of Co^{2+} ions and the weak anisotropy of the Mn^{2+} ions, which naturally order in a plane perpendicular to the Co^{2+} easy axis. Nuclear magnetic resonance (NMR) experiments of the system (Kubo et al 1984,1989) indicated that in the intermediate (mixed phase) region two different phases coexist, with the average spins aligned along the easy axis of Mn^{2+} or Co^{2+} separated by domain wall regions where the spins align at an angle to both easy axes.

The authors used several simplifications in modelling the mixture, including the use of a simple small 20 by 20 site square lattice, and identical exchange constants for each antiferromagnet. They also used highly-ordered configurations of Co^{2+} and Mn^{2+} ions rather than truly random ones. For example in the intermediate region Co^{2+} ions were grouped into rectangular arrays rather than being scattered randomly about the lattice. Their Monte Carlo results agreed well with the NMR results, with the coexisting spin populations and domain wall structures being detected. However, their results could be a consequence of how they artificially constructed their configurations of ions and may not be valid for truly random distributions of ions. It should be noted that the lattice constants for $CsMnCl_3.2H_2O$ and $CsCoCl_3.2H_2O$ differ by only 2% (Igarashi et al 1992).

Nevertheless the results from these previous studies all strongly suggest clusters of pure ions within mixtures have a noticeable effect, directing the

creation of coexisting populations with different average spin behaviours.

5.2 Monte Carlo simulations of the $Fe_xNi_{1-x}Cl_2$ system.

In the present study, Monte Carlo simulations of $Fe_xNi_{1-x}Cl_2$ were performed via a semi-classical model where the spins could be oriented in any direction in space. As a check on the computation, results were obtained for a simulation of the Ising model applied to pure $FeCl_2$. This was then compared with previous studies on this compound. The Fortran computer programs (Ising and Many for the Ising model and Heisenberg-like model respectively) were written in Vax Fortran.

5.2.1 Common features of the simulations.

The models used the Hamiltonian

$$H = -J_{ij} \sum_{i>j} S_i S_j \tag{5.1}$$

for the Ising model and

$$H = -\sum_{q,i>j} \left(J_{ij}^q S_i^q S_j^q - A(S_i^z)^2 \right) \tag{5.2}$$

for the Heisenberg model. The variable S_i in equation 5.1 represents the effective spin ± 1 (Ising model) or effective spin component (Heisenberg-like model) of the ith spin with magnitude 1, and S_i^q represents the qth spatial component of the ith spin in equation 5.2 (where $q = 1...3$). The index i sums over every spin, j sums over every nearest, next-nearest and between plane nearest-neighbouring spin of the ith spin. The J terms are exchange terms for effective spin pairs. These terms exhibit anisotropy, since their z components are 40% larger than their x and y components for Fe^{2+} pairs (Birgeneau et al 1972). The second term in equation 5.2 represents the

magnetic anisotropy with A the single-ion anisotropy constant. This term is not needed in the Ising model since either possible orientation (parallel or anti-parallel to the c axis) has the same anisotropy energy.

Values for the various exchange constants for pure $FeCl_2$ and $NiCl_2$ could be obtained from inelastic neutron scattering studies of the compounds (Birgeneau *et al* 1972, Wiltshire and Hayes 1978 and Lindgard *et al* 1975) but were initially set to agree with those set by Hernandez *et al* (1993a) to allow a direct comparison with their Monte Carlo study of pure $FeCl_2$. These values were 6.74 K, -1.01 K and -0.07 K for nearest-neighbour, next-nearest-neighbour and between plane nearest-neighbour spin pairs respectively. They used these constants to obtain the correct Néel temperature of $FeCl_2$ of 23.15 K in their simulations.

Both simulations used a lattice corresponding to a slanted cube of lattice sites pictured in Figure 5.1, consisting of a leaning stack of rhombuses.

This shape was chosen for programming convenience, and accurately modelled the true physical lattice.

Each line intersection in figure 5.1 represents an Fe^{2+} or Ni^{2+} ion. The lattice sites were labelled by the integer indices (K,I,J) as shown, with three corner ions of the lattice indicated in the figure with these indices as coordinates. The spatial components of the spins at each lattice site were coded in a matrix M(K,I,J). The indices ran from 1 to an integer L which could be arbitrarily chosen.

Periodic boundary conditions were used to ensure that every spin, including the ones at the edges of the lattice, had the same number of neighbours. Thus a spin at the top of the sample had nearest between- layer-neighbours at the very bottom of the sample, and so on. To have simply left the edge spins with free ends (with certain neighbours non-existent) would probably have caused more inaccuracy (Binder and Heermann 1992).

In performing the Monte Carlo operations each site was visited in a loop over the indices K,I,J with each site being visited once per Monte Carlo step. During each visit, a new spin orientation was randomly chosen, and the energy before (E) and after (E') this reorientation occurred was calculated. The standard Metropolis probability function was used to decide

Figure 5.1: Lattice used in the Monte Carlo simulations.

(12 sites to a side = 1728 sites.)

Twelfth layer. ———>

(12,12,12)

(12,1,1)

K

J

I

(1,12,1)

First layer.

—∕— At every line intersection: an Fe or Ni ion.
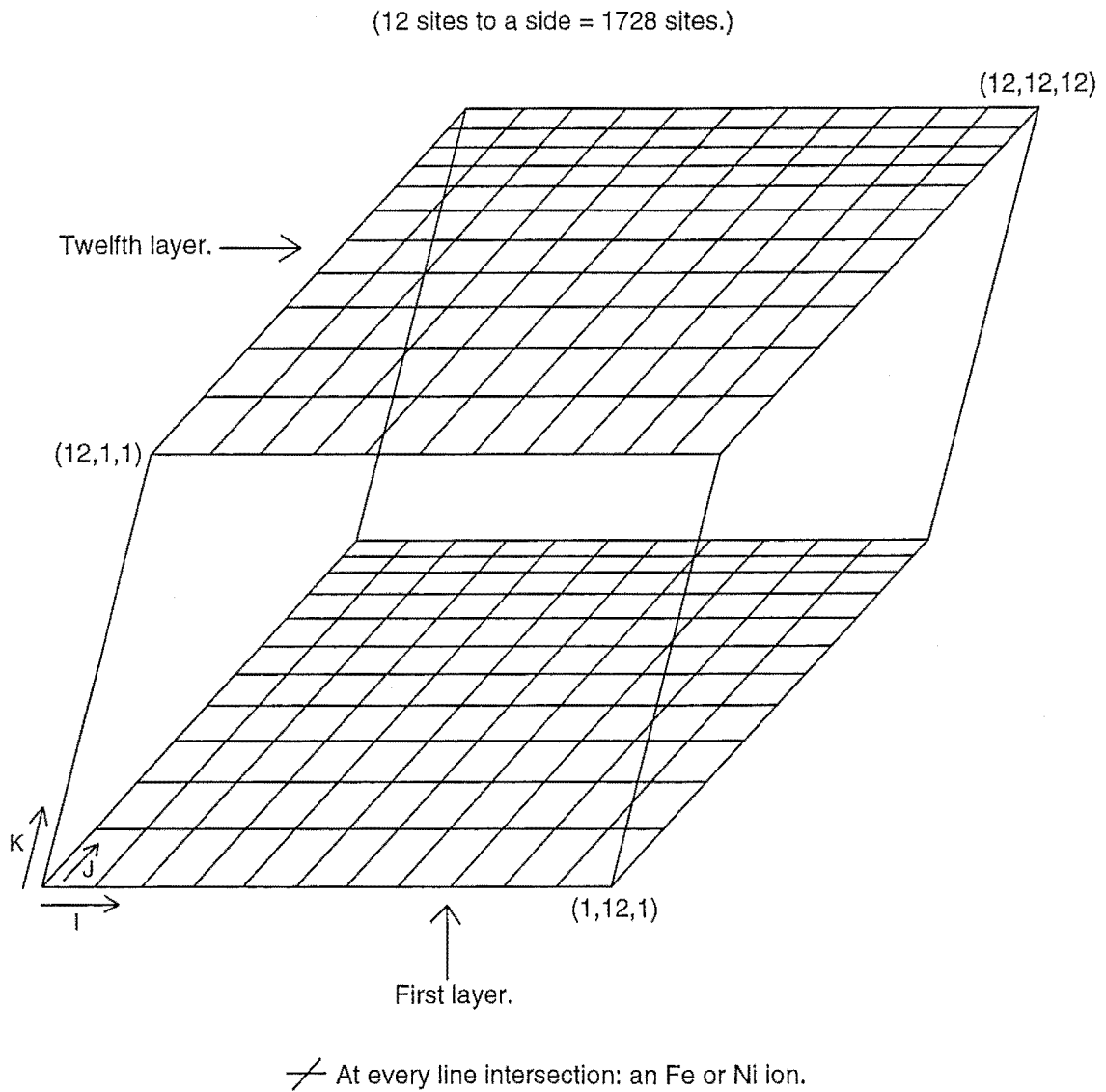
whether to accept that new state or to keep the previous state as the representation of the spin for that step. As was discussed in chapter 3, the Metropolis function ensures that the configurations of spins produced by the Monte Carlo simulations, each produced from the previous configuration (that is, a Markov chain) are produced in proportion to their thermodynamic Boltzmann factor $\exp\left(\frac{-E}{kT}\right)$ with k the Boltzmann constant, and T the temperature in Kelvin. Hence the theoretical spin behaviour will be similar to the physical spin behaviours (Binder and Heerman 1992). This function is defined as follows:

$$P = \exp\left(-\frac{E' - E}{kT}\right) \quad (E' > E) \tag{5.3}$$

or

$$P = 1 \quad (E' < E) \tag{5.4}$$

The states for the first half of each computer simulation were not analysed since the system required time to reach equilibrium about the lowest energy states.

A problem common to all Monte Carlo simulations is worth mentioning. Since the simulations use very small lattices in comparison with the real samples of the various materials, finite size effects are present (Binder and Heermann 1992). The system can access states with high average energy per spin since the total energy can still be low since few spins are present. However, these states are not accessible in a real sample with many spins present, where that same high energy per spin translates to a very high total energy. Therefore quantities calculated will always be an approximation, even if a very large number of steps are used in the simulation.

5.2.2 The Ising model.

The Ising model gave only an approximate description of the $FeCl_2$ system. It is a reasonable description, since the iron spins spend much of their time close to the c axis due to their strong uniaxial magnetic anisotropy. However

configurations with the spin directions at many possible angles to the c axis are possible physically. The Ising model will therefore ignore many possible configurations of spins, including many of quite low energy with little spin disorder present. And the experimental results indicate spin averages that do not lie parallel or anti-parallel to the c axis in the mixed phase, making an Ising simulation inadequate to account for observations.

The problem of spontaneous symmetry breaking arose in the results. The lowest energy state is one in which all the Fe spins orient parallel or anti-parallel to the c axis, with neighbouring spins anti-parallel to one another. However the exact opposite state (spins that were parallel to the c axis now antiparallel, and vice versa) has the same energy and will occur occasionally, if the system consists of few spins, as is the case for Monte Carlo simulations, which use small lattices for reasons of computer processing speed. When the Ising simulations were run, it was noticed that spins tended to align in one direction, but all spins could flip to the opposite orientation more frequently as the temperature increased. This change to the opposite state would be very rare for a large physical system, and the effect was corrected for by taking absolute values of the magnetisations calculated.

The simulations were started with all spins parallel to one another within each plane and anti-parallel to the spins in adjacent planes, and run times were set for 20 000 Monte Carlo steps.

Quantities calculated in the simulation were the staggered magnetisation M and initial magnetic susceptibility χ (the magnetic susceptibility when the magnetic field is zero).

$$M = \frac{1}{N} \sum_{1,2} (S_1 - S_2) \tag{5.5}$$

$$\chi = \frac{1}{T} \left(<M^2> - <M>^2 \right) \tag{5.6}$$

where, in equation 5.5, the sum is over all spins for one Monte Carlo step

with the labels 1 and 2 signifying which sub-lattice the spins belong to (i.e. whether the spin is on a plane with an odd or even value of the coordinate variable K). The variable M represents the average spin magnitude over the whole lattice, summing the spins on the different sublattices differently since the spins orient in opposite directions within the different sublattices/layers.

This quantity was averaged over the entire Monte Carlo simulation. The quantity $< M >$ in equation 5.6 represents that average. N is the total number of spins, and T in equation 5.6 is the temperature in Kelvin.

A graph of magnetisation vs temperature derived using the Ising model for a lattice with L=16 is displayed in figure 5.2, together with values for the magnetisation obtained from NMR studies (Jacobs and Lawrence 1967).

The Monte Carlo magnetisation curves are slightly higher than the curve derived from the NMR study. This is probably because only two states were available to each spin; the lower energy states occurred when the spins were parallel to a majority of in-plane nearest neighbours. Other possible states were very high in energy, since spins with several neighbours misaligned necessarily means total misalignment with those neighbouring spins, as only perfect alignment or misalignment was possible.

The Monte Carlo process therefore often rejected those higher energy states. In comparison, the physical system should allow many states with spins at a variety of angles, with spins close to being parallel to one another. These configurations, which are not allowed in the Ising model, are of low energy yet decrease the staggered magnetisation, so their absence increases the magnetisations calculated from the Ising model.

Hernandez et al (1993a,1993b and 1994) using the Monte Carlo Ising model, simulated the dilute magnetic system $Fe_xMg_{1-x}Cl_2$, a random mixture of the antiferromagnet $FeCl_2$ and the non-magnetic compound $MgCl_2$.

As part of their work, they studied pure $FeCl_2$ and found the temperatures where the initial magnetic susceptibilities reached a peak for several different lattice sizes. Figure 5.3 shows the results derived from the present work on the Ising model with results from Hernandez and Diep (1994) plotted also for comparison. In this figure, the magnetic susceptibility is shown as a function of temperature and the lattice size L. Only the peak values of

Figure 5.2: Magnetisation data as a function of temperature for $FeCl_2$ derived from Ising Monte Carlo simulations using a lattice with L=16 (o) and NMR studies (Jacobs and Lawrence 1967) (*). Exchange constants used were 6.74 K, −1.01 K and −0.07 K for the nearest in plane neighbour, next-nearest in plane neighbour and nearest adjacent plane neighbour respectively. Uncertainties for both data sets are indicated by vertical lines.
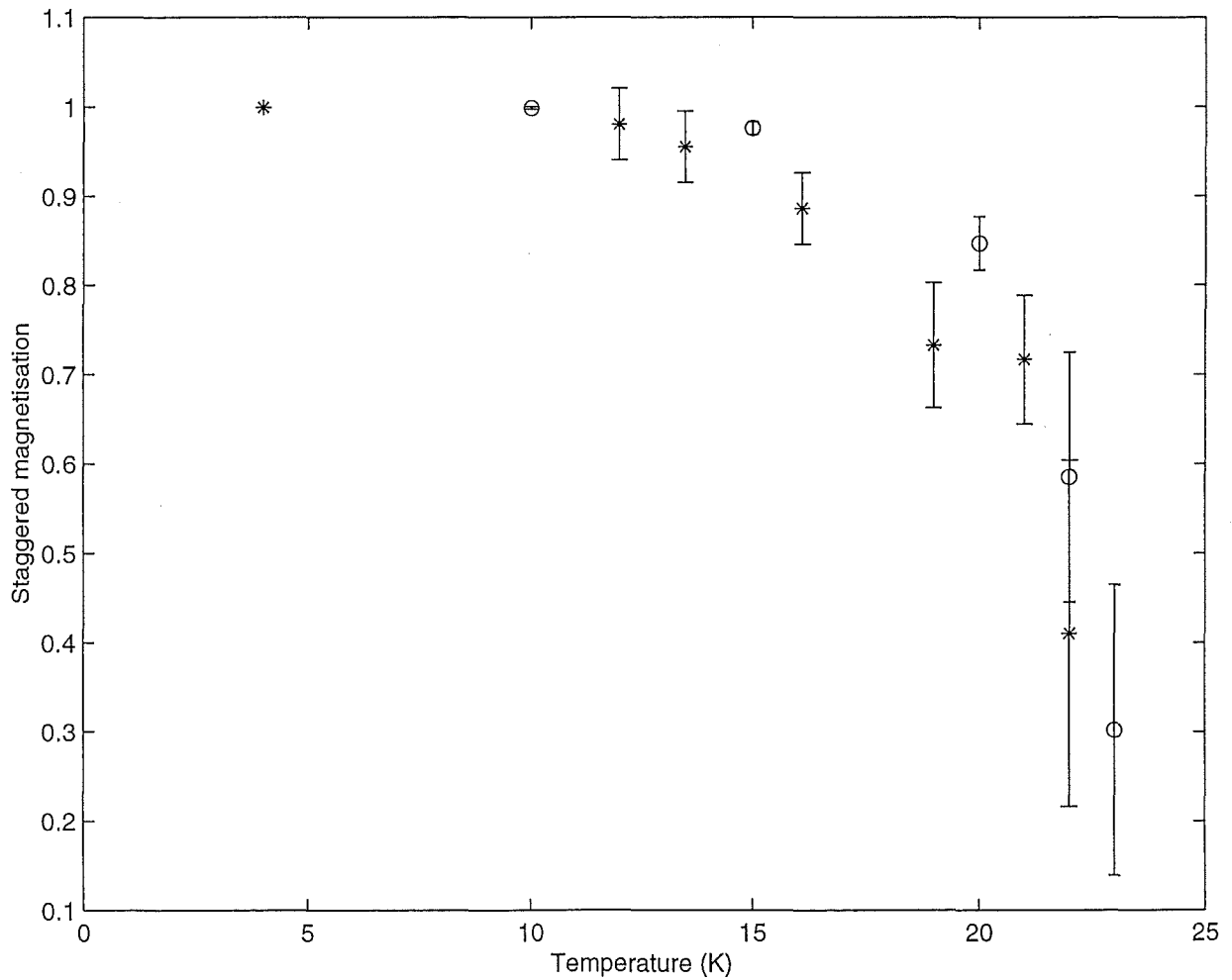
Figure 5.3: Initial magnetic susceptibility data calculated in the present study from Ising Monte Carlo models using a lattice size L=20 ($\square$), L=30 (o) and L=40 ($\triangle$) vs temperature. The peaks in the curves derived from Hernandez and Diep (1994) are also indicated ($*$). The exchange constants chosen were as for figure 5.2. Uncertainties are indicated by vertical lines.
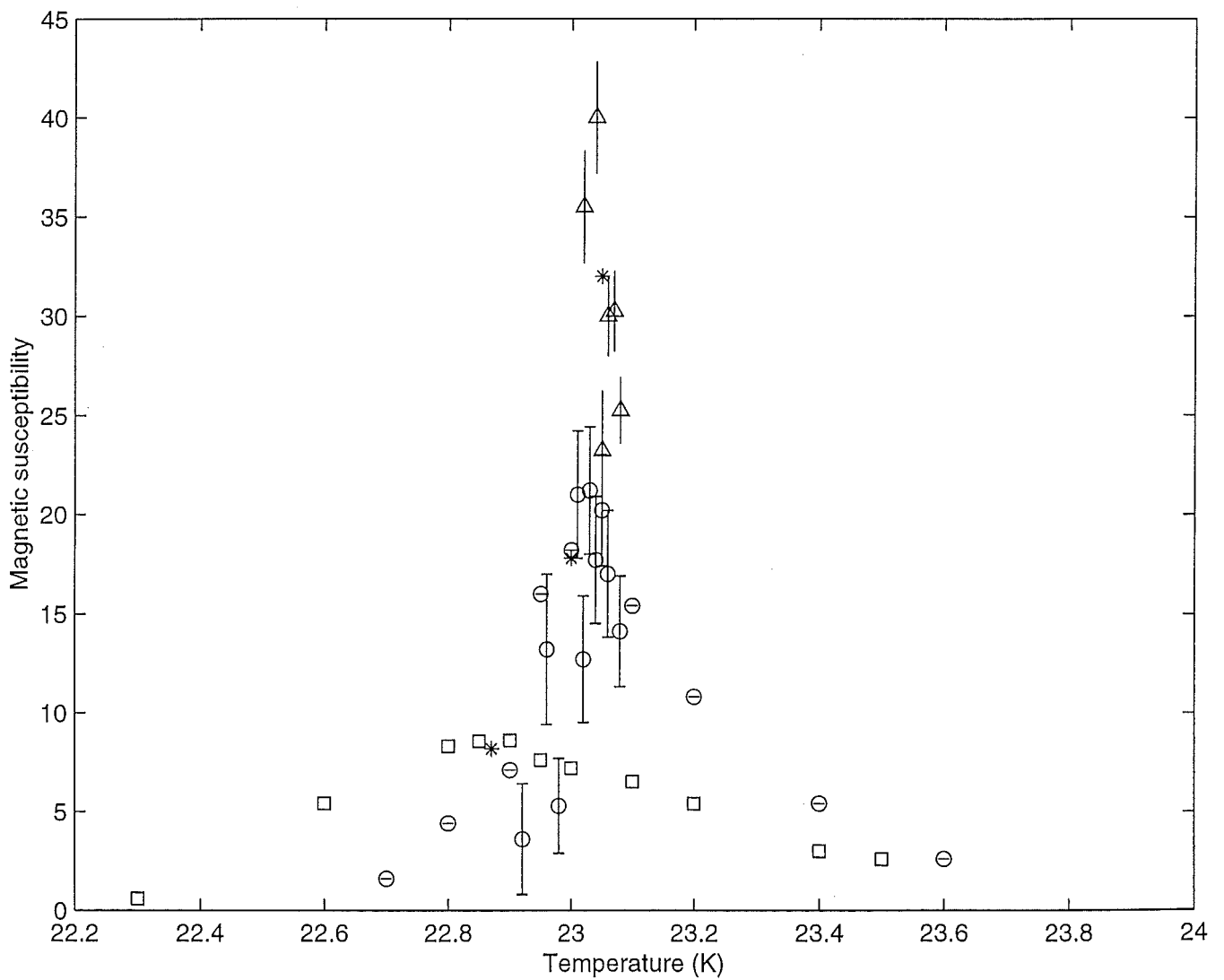
the curves from Hernandez and Diep were given.

The peaks in the curves derived from Hernandez and Diep were in good agreement with the Ising model for L=20 used in the present work, but were too low for the L=30 and L=40 cases. This may be because great care was taken to find the peak positions in the present work with many different readings close to the peak positions being taken. It was noted that as the system size L increased, the peak moved towards T=23.12 K, close to the measured Néel temperature of 23.6 K for $FeCl_2$.

It was therefore concluded that the model used in the program Ising in the present work gave results equivalent to past workers results and consistent with experimental observations. The program was then developed further into the program MANYDIR to model the more complex $Fe_x Ni_{1-x} Cl_2$ system.

5.2.3   Simulations allowing many spin orientations.

Simulations allowing only a small finite number of spin orientations were performed, the available states being graphically represented in figure 5.4. In the figure the small circles represent the available spin states, at several different angles with respect to the c axis (angle θ) and an arbitrary perpendicular axis (azimuthal angle ϕ). If the available spin states are represented by vectors radiating from the centre of a sphere of radius 1 out to the sphere's surface, then figure 5.4 shows a 2D view of the sphere from directly above. The small circles indicate where the spin vectors intercept the surface of the sphere, and are labelled with their θ and ϕ values. In the figure only the spins intercepting the upper hemisphere of the sphere and equator ($\theta = 90°$) are shown. When the simulations were performed for the pure $FeCl_2$ and $NiCl_2$ cases, a serious problem was noted when 26 states were made available. A very large anisotropy constant was required to confine the Ni^{2+} spins to the xy plane at high temperatures ($T > 30$ K). In fact the anisotropy constant had to be 30 times larger than its experimental value of 1 K (Lingard et al 1975). Otherwise the spins had a strong tendency to align parallel/anti-parallel to the c axis, which occurred even when the anisotropy constant for Ni^{2+} was set to zero.

Figure 5.4: Spin orientations available in Heisenberg Monte Carlo models using a finite number of spin states.

26 states available .   114 states available.
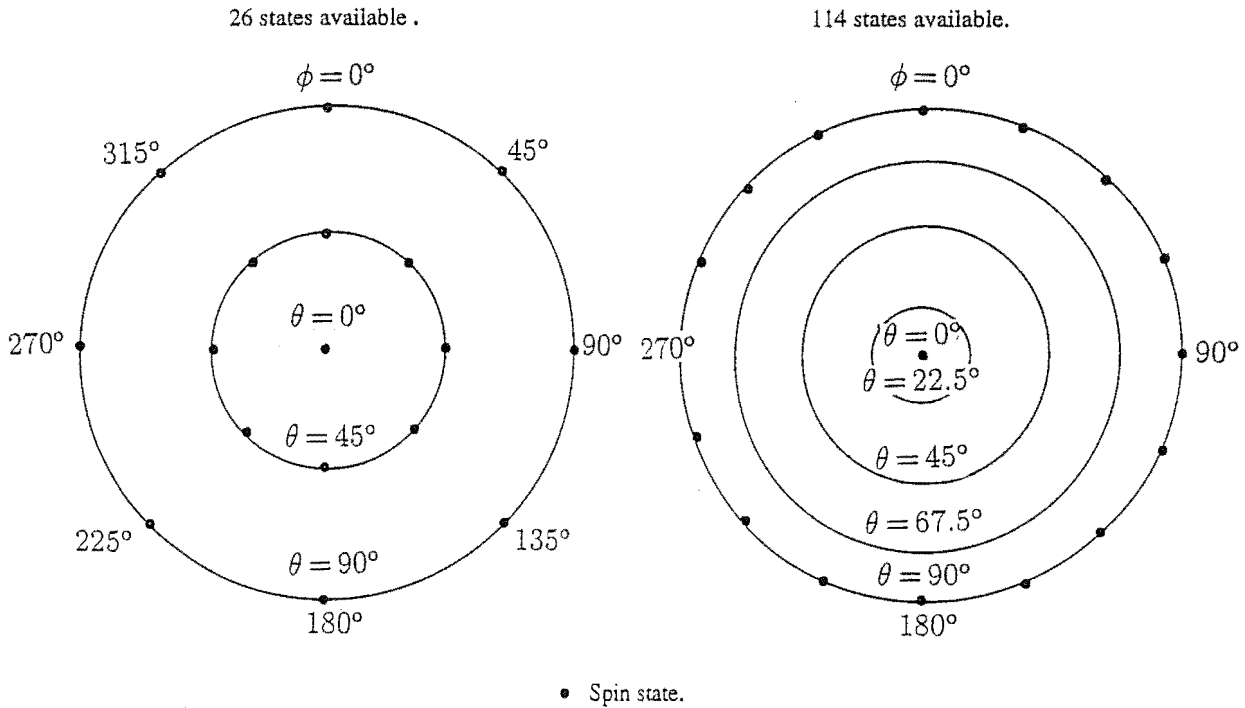
• Spin state.

This effect was thought to be a consequence of the lack of smoothness in the available state array (that is each point on the sphere of available states in figure 5.4 is not equivalent in terms of angles relative to neighbouring spin states). The problem remained even when more states were made available (114 states). This made the mixed system impossible to model, since the anisotropy constant for $FeCl_2$ is ten times larger than the $NiCl_2$ constant, which would thus require an anisotropy constant for pure $FeCl_2$ of 300 K (c.f. experimental value of 10 K). This grossly exaggerated value would mean the anisotropy would totally dominate over the exchange interactions, a situation which does not occur in the experimental case.

To overcome this problem, the available spin states were made continuous in space (In fact 4^{18} states were made available) and the problem of confining the Ni^{2+} spins to the xy plane disappeared, with a more realistic value for the Ni^{2+} anisotropy constant (2 K) being enough to confine the spins even at the high temperature of 50 K.

Each spin was analysized separately and its angle θ from the c axis was recorded, as well as the staggered magnetisation for each ionic species. Simulations were run with zero anisotropy constants, to check for random behaviour of the magnetisations which was expected in that case. In this test, the spins behaved as expected, drifting randomly in 3D space, with no attraction to any axis or plane.

With non zero anisotropy constants, it was noticed that the xy type anisotropy of $NiCl_2$ caused the Ni^{2+} spins to slowly drift around the c axis in the pure $NiCl_2$ case. As a result the spin components and magnetisations averaged to zero after many Monte Carlo steps. To correct for this, the spin components were recorded and averaged in groups large enough to get accurate results for the angle θ , yet insufficient for the spins to have drifted much about the c axis. These values for θ were then averaged. The spins were all initially aligned with θ set at $45°$ or $135°$ depending on which sublattice the spins belonged to. This orientation was chosen to ensure the end point did not depend on the initial orientations.

Simulations were performed to determine the values of the exchange and anisotropy constants needed to accurately model the pure $FeCl_2$ and $NiCl_2$ systems. The constants attempted were similar to the values chosen by previous workers and based on experimental work. Two approximations were used in common with mean-field studies of mixed systems (Igel et al 1990, Matsubara and Inawashiro 1976 and Someya 1981). The exchange constants for an Fe^{2+}-Ni^{2+} pair were taken to be the geometric mean of the pure Fe^{2+}-Fe^{2+} and Ni^{2+}-Ni^{2+} values and the anisotropy constants were not varied with temperature. The magnetisations were only weakly dependent on the anisotropy constants since these were smaller than the exchange constants. The anisotropy determined the directions for the spin averages, and was not important in determining their average values. In any case, variations of the anisotropy constants with temperature would be very difficult to simulate since very large constants would be needed at low temperatures (experimentally the anisotropy increases with decreasing temperature) as over strengthening of the anisotropy constant for Ni^{2+} was necessary to

confine the Ni^{2+} spins to the xy plane for the pure $NiCl_2$ case at high temperature. Such large values for the anisotropy constant would unrealistically under estimate the importance of the exchange interactions for determining magnetisations and spin behaviours. The anisotropy constant for $FeCl_2$ was also increased to avoid the Ni^{2+} anisotropy being relatively over-emphasised, which would deform the magnetic phase diagram of $Fe_xNi_{1-x}Cl_2$. The ratio between the increased anisotropy constants was set equal to the original ratio between the experimental values of the constants.

The value of the Ni^{2+} anisotropy constant chosen finally was that value just sufficient to hold the spins to the xy plane at the high temperature of 50 K, for a large (L=12) lattice simulation. It was noticed that larger values of L meant a smaller anisotropy constant was necessary, but those larger system sizes took a long time to simulate (several days compared with 10 hours for a run of 20 000 Monte Carlo steps). With a large group of ions as in a real crystal, the chance that many spins differ far from the most likely orientation is slight as that would represent a very large energy compared to the ground state. The more spins present, the greater this energy difference will be. A small sample as studied in Monte Carlo simulations with given anisotropy constants will therefore have the ability to drift further from the ground state, for example by drifting out of the xy plane. Thus over estimates of the anisotropy constants is less and less necessary to confine the spins to the xy plane as the system size is increased.

The magnetisation curves derived from the Monte Carlo simulations in this work are compared with experiments (Lingard *et al* 1974, Jacobs and Lawrence 1967) for $FeCl_2$ and $NiCl_2$ in figures 5.5 and 5.6 respectively with the final choice of constants indicated.

The spins had the correct behaviour with the Fe^{2+} spins fluctuating about the c axis and the Ni^{2+} spins randomly moving about the xy plane. However the simulation magnetisations were typically 5-10% lower than the experimental values. This is probably due to the small size of the systems under study (12^3=1728 spins) with the spins again fluctuating more strongly about their easy axis/planes than would spins in the physical case, reducing their magnetisations below the physical values.

5.2. Monte Carlo simulations of the $Fe_x Ni_{1-x} Cl_2$ system.

70

Figure 5.5: Magnetisation data for $FeCl_2$ calculated by the Monte Carlo Heisenberg model (o) vs experimental data (Lingard *et al* 1974) (*) as a function of temperature. Exchange constants used were 5.8 K, -0.72 K and -0.07 K for the nearest in plane neighbour, next-nearest in plane neighbour and nearest adjacent plane neighbour respectively together with an anisotropy constant of 15 K. Uncertainties for the experimental data are indicated by the vertical lines.
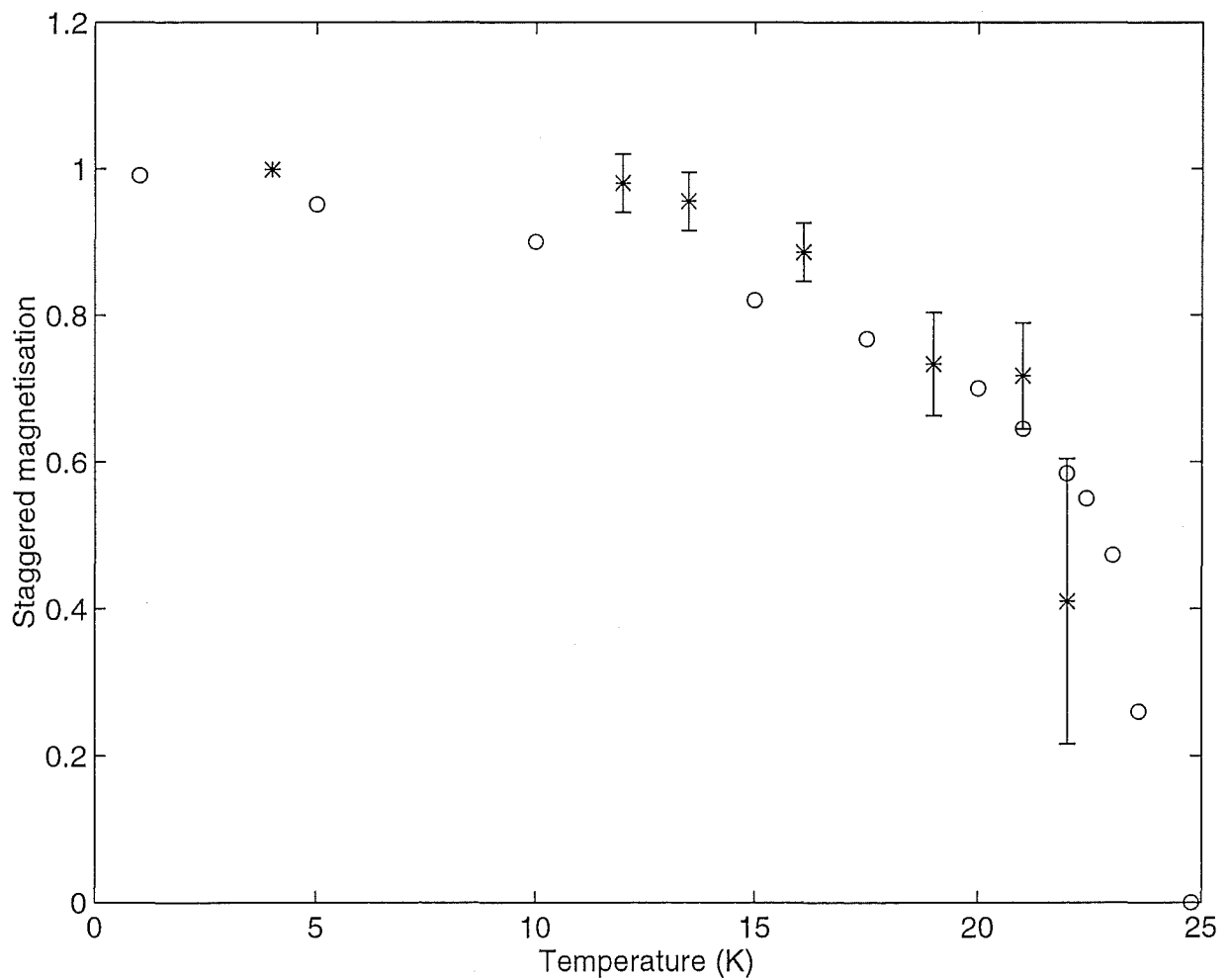
Figure 5.6: Magnetisation average for $NiCl_2$ calculated by the Monte Carlo Heisenberg model (o) and experimental data (Jacobs and Lawrence 1967) (*) as a function of temperature. Exchange constants used were $30.5\,K$, $-6.45\,K$ and $-0.33\,K$ for the nearest in-plane neighbour, next-nearest in-plane neighbour and nearest adjacent-plane neighbour respectively together with an anisotropy constant of $-2\,K$. Uncertainties for the experimental data are indicated by the vertical lines.
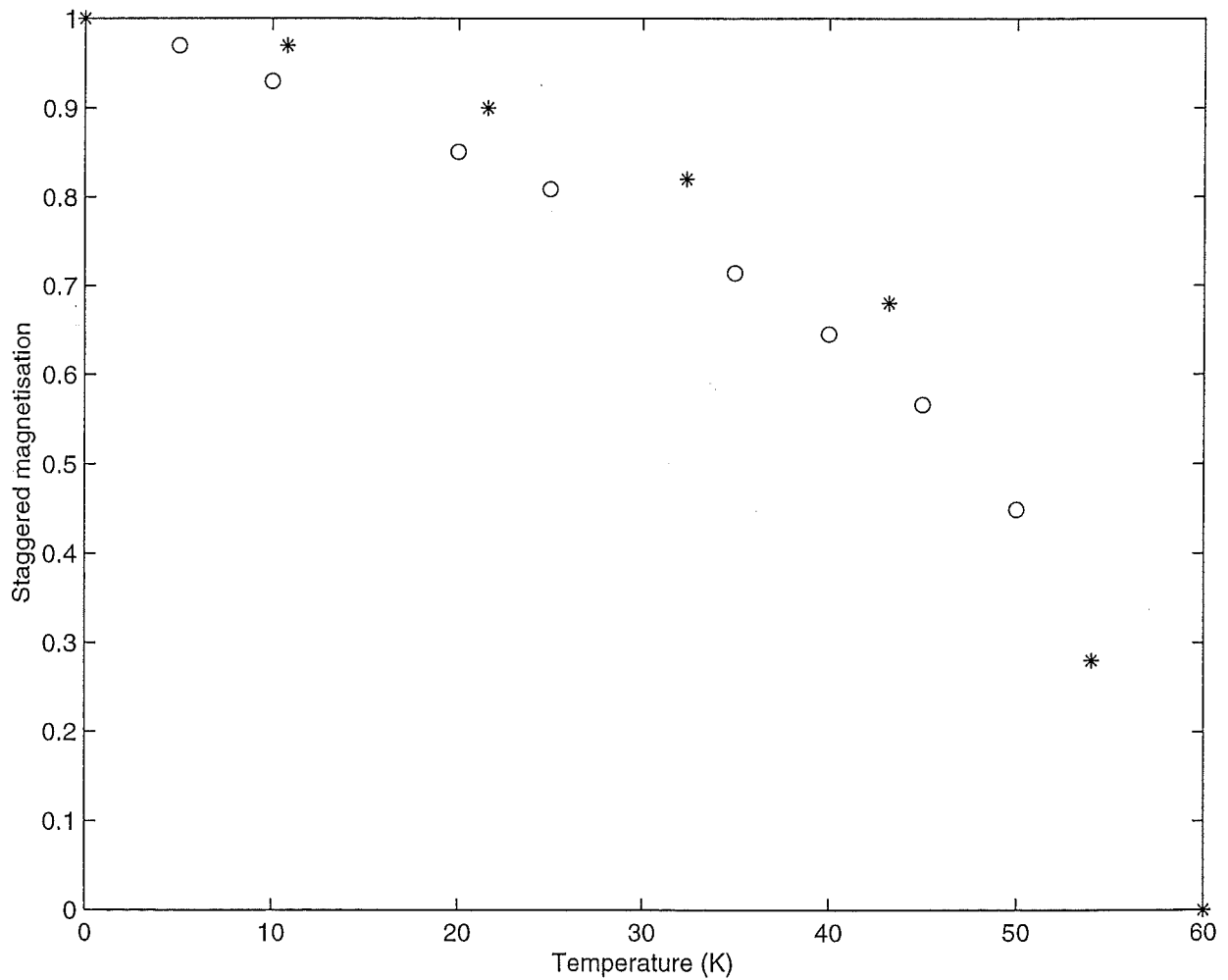
The simulations exhibited statistical errors too small to be plotted on the curves when the simulations were run for 40 000- 80 000 Monte Carlo steps, and the resulting curves are not perfectly smooth to within the (practically zero) errors. The calculation of the errors assumed statistical independence of the magnetisations from step to step, yet each configuration of spins is closely correlated to the configuration from the previous Monte Carlo step. Hence the average magnetisation for a finite number of Monte Carlo steps will slowly fluctuate about the true average value (the value for an infinite number of Monte Carlo steps) and will have an error somewhat larger than the one calculated.

These problems not withstanding, the curves were close enough to the experimental ones to be considered adequate Monte Carlo representations of the pure physical systems, and the exchange and anisotropy constant values were retained for the $Fe_xNi_{1-x}Cl_2$ system. Several long (more than 40 000 steps) simulations were run and the results are displayed in figure 5.7. The arrows in figure 5.7 indicate the directions along which Fe^{2+} spins are oriented on average, and the c axis is also indicated. The shape of the phase diagram is good, with the correct pure anti-ferromagnetic phases observed with the average spins all close to the c axis for x large or confined to the xy plane for x small. However at intermediate concentrations (near $x=0.09$) the spins aligned at an angle to the c axis and no coexisting populations were seen in accordance with the predictions from mean-field theory. Past workers' results detected coexisting spin behaviours within the intermediate region when clusters of pure species were significant in mixtures as mentioned in section 5.1; in $Fe_xNi_{1-x}Cl_2$ the intermediate phase occurs for small values of x (from 0.03 to 0.09) and so large clusters would be rare. However on the assumption that clusters are necessary to form these coexisting populations, several different ionic clustering regimes were attempted, with the aim being to find a method of constructing clusters in a physically reasonable way which can consistently explain the experimental results.

Figure 5.7: Monte Carlo phase diagram for $Fe_xNi_{1-x}Cl_2$. The simulations were performed assuming a random distribution of metal ions.
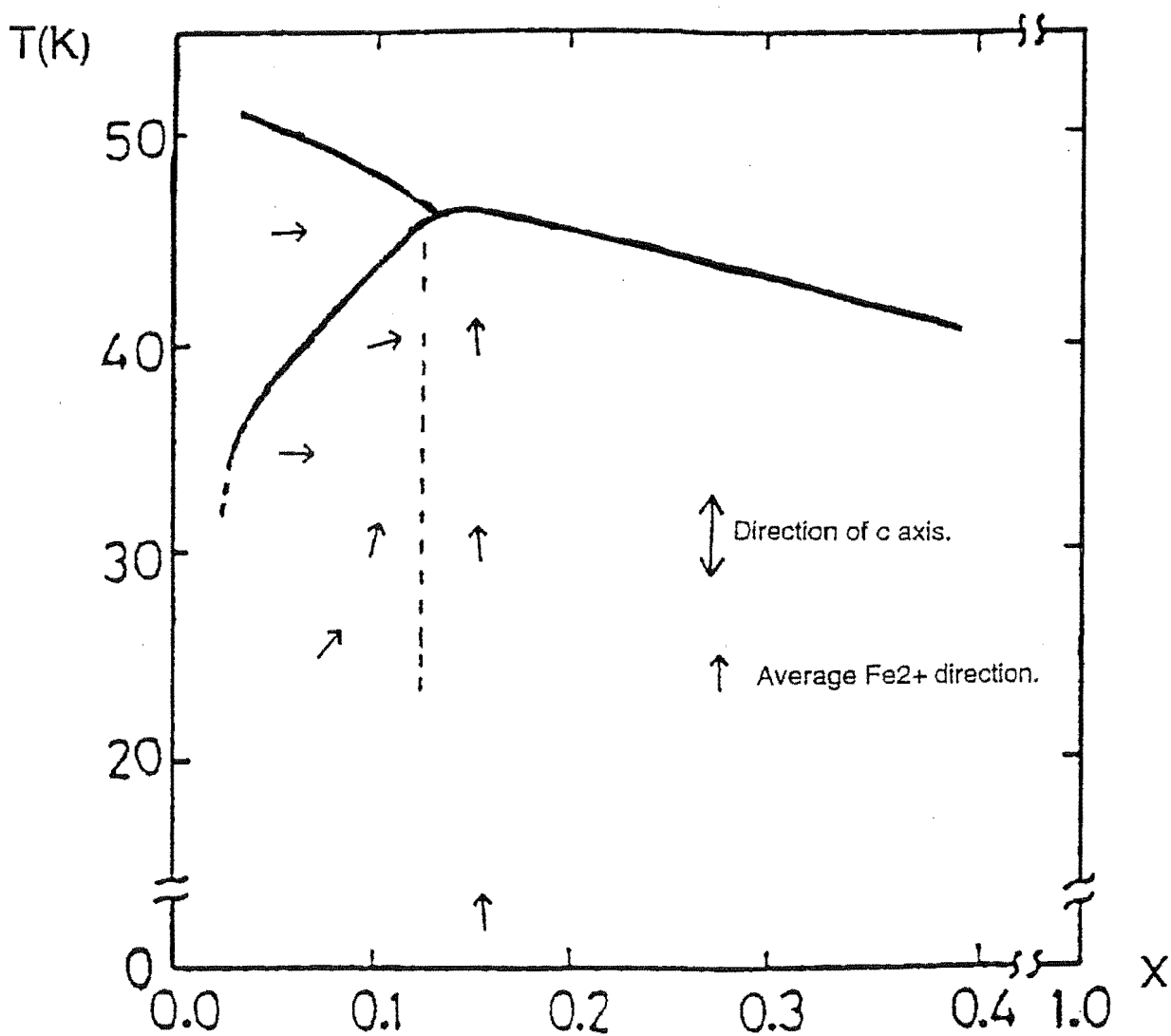
Figure 5.8: One large central cluster of Fe^{2+} ions embedded in a lattice of Ni^{2+} ions.

o   Fe ion.
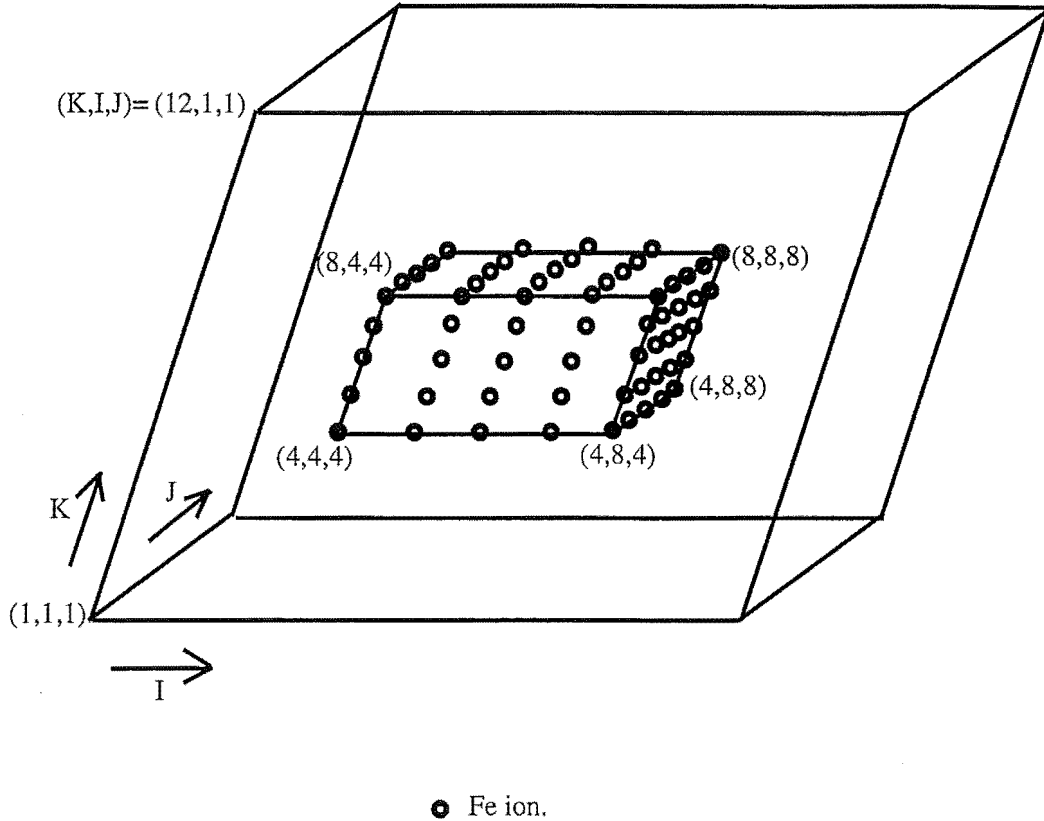
5.3   Cluster simulation results for an $x = 0.08$
Fe$_x$Ni$_{1-x}$Cl$_2$ crystal.

5.3.1   Pure Fe^{2+} clusters.

Figure 5.8 shows the cluster used for a system with L=12 and $x = 0.08$ which was experimentally found to be within the mixed phase up to a temperature of approximately 50 K (Tamaki and Ito 1993). The large central cluster of Fe^{2+} ions was set in a lattice of Ni^{2+} ions. At 30 K the Fe^{2+} spins became almost paramagnetic, with only a small magnetisation. This was significantly lower than the experimentally determined Néel temperature of 50 K. The exchange interactions were not able to hold Fe^{2+} spin order at this temperature, probably because most neighbours of the Fe$_x$Ni$_{1-x}$Cl$_2$ ions were other Fe^{2+} ions in the cluster, and the Fe^{2+}-Fe^{2+} interaction is significantly smaller than the Fe^{2+}-Ni^{2+} interaction.

Figure 5.9: Ion configuration with five small clusters of Fe^{2+} ions embedded in a lattice of Ni^{2+} ions.

$\circ$ Fe ion.
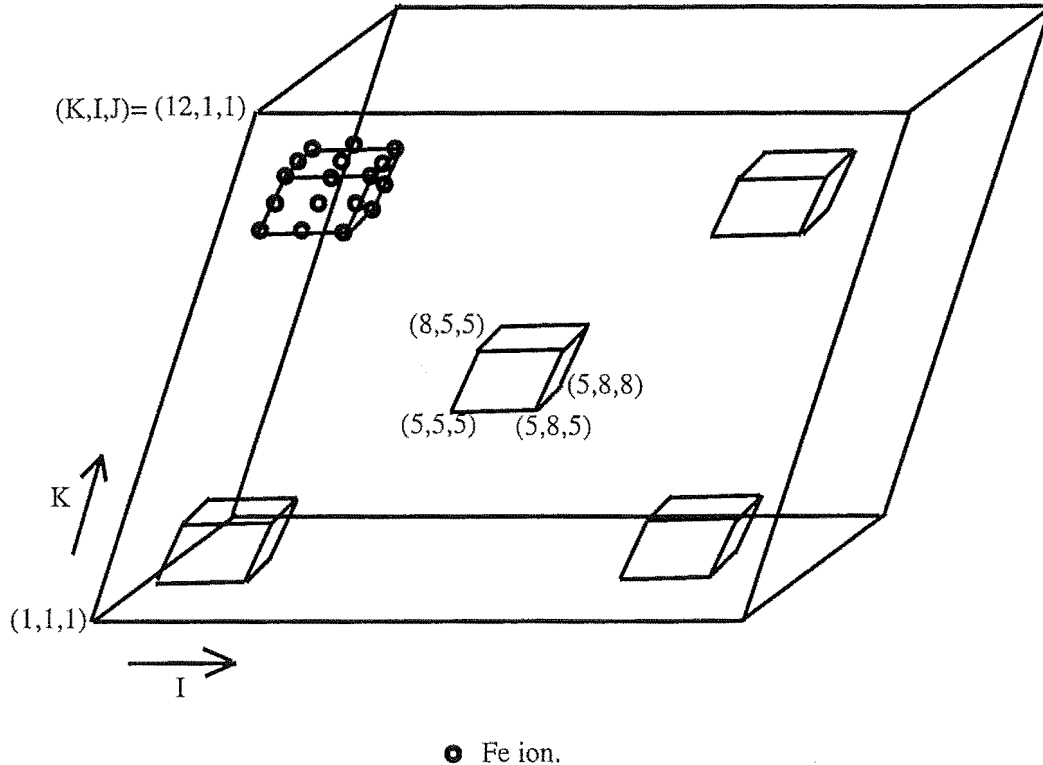
It can therefore be concluded that more couplings to the Fe^{2+} spins must be of the Fe^{2+}-Ni^{2+} type. If pure clusters of Fe^{2+} ions are responsible for the Fe^{2+} spin behaviour then they must be smaller to reduce the number of Fe^{2+}-Fe^{2+} interactions. Further simulations were attempted using 5 small pure Fe^{2+} clusters of 27 spins each, as shown in figure 5.9. However at 30 K the magnetisation of Fe^{2+} spins was again found to be small.

The next simulations involved impure clusters, which contain many Fe^{2+}-Ni^{2+} linkages and could theoretically be large enough to significantly affect the overall spin behaviour.

5.3.2　Impure clusters.

The following simulations all involved impure clusters containing a high Fe^{2+} concentration, embedded in an environment of $Fe_xNi_{1-x}Cl_2$ with x low.

Any clusters of high Fe^{2+} content which might exist and influence the overall spin behaviour are of an unknown nature. Therefore clusters with several different Fe^{2+} contents were simulated, as well as different cluster sizes and shapes.

Models with centrally located cubic clusters of size 5^3 to a side were modelled for the concentrations x=0.5 and 0.72 within the cluster respectively. The result again was' paramagnetic behaviour setting in at temperatures significantly less than 50 K. It set in above 20 K and 30 K for the cluster concentrations $x = 0.5$ and 0.72 respectively.

This recurring problem could be due to the use of a geometric mean in calculating the exchange interaction J_{Fe-Ni} for a Fe^{2+}-Ni^{2+} pair where

$$J_{Fe-Ni} = \sqrt{J_{Fe-Fe} \cdot J_{Ni-Ni}} \qquad (5.7)$$

If this was lower than the true value then, since this interaction is larger than the Fe^{2+}-Fe^{2+} interaction (and is therefore relatively significant in determining Fe^{2+} behaviour) the energy tending to order Fe^{2+} spins would be too low in the simulations. This would be particularly significant at high temperatures, where a large energy is needed to keep Fe^{2+} spins ordering at all. Lower energies will mean lower Fe^{2+} magnetisations (and premature paramagnetic behaviour) . A low Fe^{2+} magnetisation would mean the Fe^{2+} anisotropy would have little impact on the system since each Fe^{2+} spin would have no strong tendency to align along its minimum energy axis, hence, in interacting with neighbouring spins, no strong tendency to align that other spin along the c axis would exist. When the Fe^{2+} spins become paramagnetic, no influence on neighbouring spin behaviours would exist at all.

Attempts were then made to take this into account, and clusters with more realistic shapes (spherical rather than cubic) were used. Also lower concentrations of Fe^{2+} within the clusters were simulated, since having unrealistically high concentrations would also tend to reduce Fe^{2+} order at high temperatures, since the Fe^{2+}-Fe^{2+} interaction is significantly lower than the Fe^{2+}-Ni^{2+} linkage, as mentioned previously.

5.3.3 A spherical cluster containing an Fe content of x=0.35.

Figure 5.10 shows a cluster with x=0.35 (within the cluster), and table 5.1 lists the results for the simulation. The Fe^{2+}-Ni^{2+} interaction was increased by 25 percent.

T(K)	θ(degrees)
10	13 ± 5 (100%)
20	10 ± 2 (100%)
40	18 ± 2 (100%)
42.5	30 ± 5 (100%)
43.5	53 ± 5 (50%) and 73 ± 5 (50%)
45	40 ± 5 (55%) and 63 ± 2 (45%)
46	90 ± 5 : almost paramagnetic (100%)
48	paramagnetic (100%)

Table 5.1: Fe^{2+} spin behaviour for one large impure cluster: x=0.35 within the cluster. $x = 0.08$ for the lattice on average. θ is the angle between the average spins and the c axis. $J_{Fe-Ni} = 1.25\sqrt{J_{Fe-Fe} \cdot J_{Ni-Ni}}$

The results show Fe^{2+} spin order persisting even at the high temperature of 46 K. At high temperatures two coexisting populations were detected, with spins oriented near the c axis or around 45° to 50° to the xy plane. As the temperature increased, spins originally oriented near the c axis jumped into the other population.

The temperatures where the different simulation spin behaviours occurred differed slightly (by 2-3 K) from the experimental data, a minor difference which is probably due in part to the lower simulation magnetisations, a problem of the small lattice size (compared to the real crystal size) as

mentioned previously.

Several variations on the model were also simulated with different values of the Fe^{2+}-Ni^{2+} exchange constant, as well as higher and lower concentrations of Fe^{2+} ions overall (a sample of a real crystal of a size 12^3 will vary in concentration from place to place). Table 5.2 lists the important results from those simulations.

T(K)	θ (degrees) : factor = 1.25 ($x = 0.068$)
43	50 ± 10 (100%)
44	43 ± 5 (34%) and 61 ± 5 (66%)
45	46 ± 5 (100%)

T(K)	θ (degrees) : factor = 1.2 ($x = 0.08$)
45	73 ± 2 (100%)

T(K)	θ (degrees) : factor = 1.3 ($x = 0.08$)
42.5	27 ± 2 (54%)
45	53 ± 2 (76%)

T(K)	θ (degrees) : factor = 1.25 ($x = 0.092$)
43	20 ± 5 (100%)
44	33 ± 2 (100%)
45	40 ± 5 (100%)

Table 5.2: Fe^{2+} spin behaviour for one large impure cluster for different values of the Fe-Ni exchange constant. $x=0.34$ within the cluster. $x = 0.08$ for the lattice on average. θ is the angle between the average spins and the c axis. $J_{Fe-Ni} = (\text{factor})\sqrt{J_{Fe-Fe} \cdot J_{Ni-Ni}}$

Of particular note from table 5.2 is the behaviour at the higher and lower concentrations. A higher concentration of Fe^{2+} ions alters the spin behaviours, with higher concentrations of Fe^{2+} ions leading to spin order closer to the c axis.

5.4 Cluster simulation results for an $x = 0.034$ $Fe_x Ni_{1-x} Cl_2$ crystal.

Simulations were then performed using the concentration $x = 0.034$ to again allow a comparison with Mössbauer results (Tamaki and Ito 1993). 60 Fe^{2+}

Figure 5.10: One large impure cluster containing an Fe content of x=0.35.
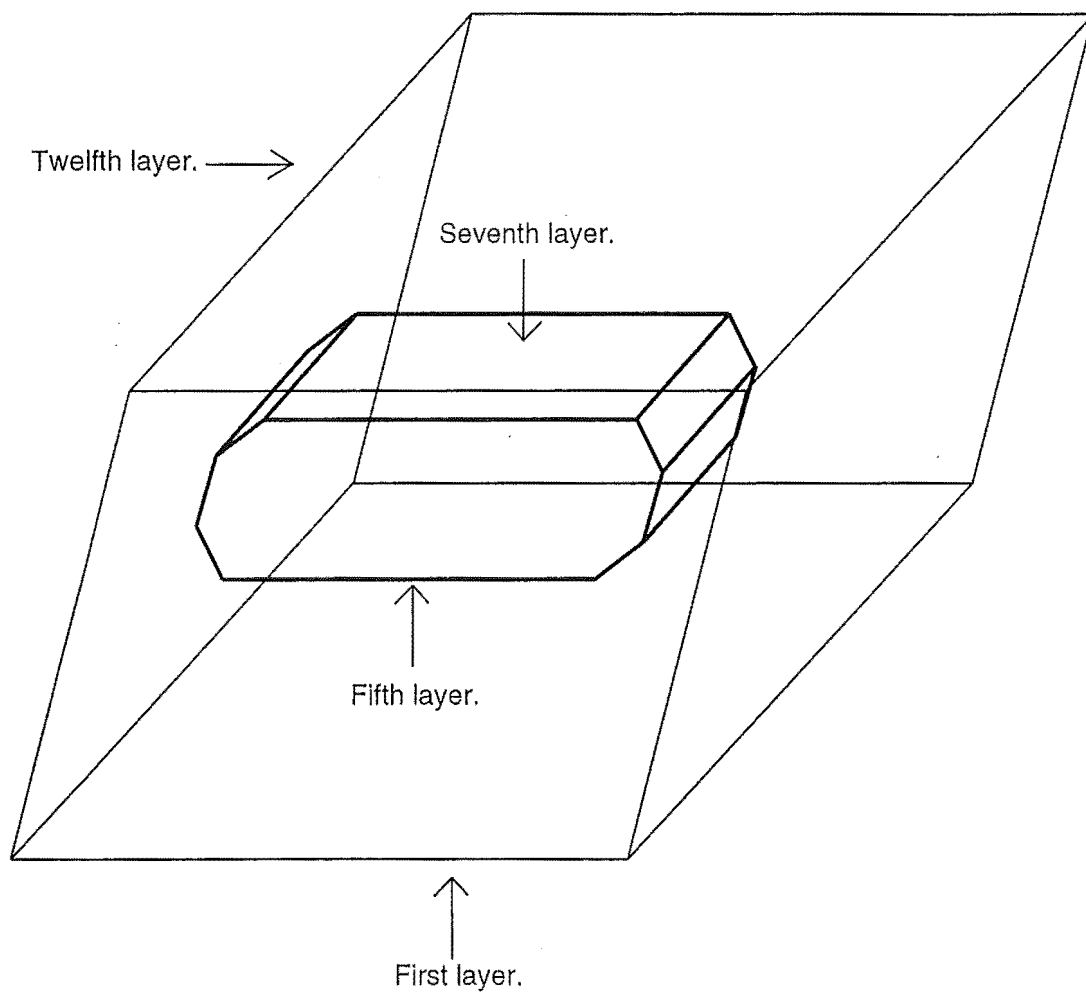
ions were embedded in a lattice of 12^3 sites, with 30 inside a small central cluster (with $x = 0.35$ within it). Table 5.3 lists the results. The interaction constants were the same as used in section 5.3.3.

T(K)	θ (degrees)
4.2	33 ± 5 (68%) and 73 ± 2 (32%)
10	33 ± 10 (55%) and 78 ± 5 (45%)
15	45 ± 10 (55%) and 75 ± 5 (45%)
25	78 ± 2 (100%)
42.5	78 ± 5 (100%)

Table 5.3: Fe^{2+} spin average behaviour for one impure cluster with $x=0.34$ within the cluster. $x = 0.034$ for the lattice on average. θ is the angle between the average spins and the c axis. $J_{Fe-Ni} = 1.25\sqrt{J_{Fe-Fe} \cdot J_{Ni-Ni}}$

Local concentrations of Fe^{2+} ions directed local behaviour, creating co-existing populations of spins which changed their orientations and relative populations with temperature.

Since a real system would probably contain a mixture of cluster sizes and contents, any simulation based on only one or several clusters will be unrealistic to some extent. For this reason, the final simulations attempted consisted of large lattices with a mixture of clusters present.

5.4.1 Large lattices with mixed clusters: $x=0.034$.

A large system of size 20^3 was modelled, consisting of three large clusters containing 363, 162 and 72 lattice sites with local Fe^{2+} concentrations in each cluster of $x=0.3$, 0.25 and 0.15 respectively, embedded in a low Fe^{2+} concentration region as before. The average value of the Fe^{2+} concentration x was 0.034.

Table 5.4 lists the results. The orientation of the Fe^{2+} spins at 10 K was the same as for the smaller system (see table 5.3) and only showed a small variation at 15 K.

A variety of other Monte Carlo simulations of the $Fe_xNi_{1-x}Cl_2$ system were done, which are not discussed in this chapter, since they gave similar results to those simulations described.

It is also important to note that the Ni^{2+} spins aligned near the Fe^{2+} spins in every simulation which was performed, but with an orientation from $0°$ to $20°$ closer to the crystalline xy plane.

T(K)	θ (degrees)	
10	33 ± 10 (32%) and 78 ± 10 (53%)	
15	38 ± 10 (38%) and 78 ± 10 (62%)	
25	81 ± 5 (100%)	

Table 5.4: Fe^{2+} spin behaviour for a mixture of several impure clusters, for $x = 0.034$. θ is the angles between the average spins and the c axis. $J_{Fe-Ni} = 1.25\sqrt{J_{Fe-Fe} \cdot J_{Ni-Ni}}$

5.5 Physical interpretations of the Monte Carlo cluster simulations.

The previous Monte Carlo simulation results showed that clusters with high Fe^{2+} content embedded in an environment with a lower Fe^{2+} concentration can create co-existing magnetic order dominated by the Fe^{2+} and Ni^{2+} anisotropies for temperatures and Fe^{2+} concentrations that bring the system within the mixed region of the phase diagram of $Fe_xNi_{1-x}Cl_2$. This behaviour is reminiscent of the experimental data for $Fe_xNi_{1-x}Cl_2$. A random distribution of metal ions could not create this kind of magnetic order, so the Monte Carlo results provide evidence for clustering behaviour within $Fe_xNi_{1-x}Cl_2$.

5.5.1 Clustering in mixed magnetic systems.

Several workers have found evidence for ionic clustering behaviour in mixed magnetic systems. Kato (1994) modelled the $CsMn_{1-x}Co_xCl_3.2H_2O$ system assuming clusters of Co ions form ordered clusters in the mixed magnetic phase (as mentioned at the beginning of this chapter). Other workers have explained co-existing magnetic order on the assumption that random fields are present in the mixed systems. These possibilities are discussed in the following subsections.

5.5.1.1 Ionic clusters in $Fe_xNi_{1-x}Cl_2$.

As noted in chapter 1, the lattice constants for $FeCl_2$ and $NiCl_2$ differ by only 3%. This means that the $Fe_xNi_{1-x}Cl_2$ system should consist of a fairly even random distribution of metal ions, without very significant clustering (this is not inconsistent with the clusters used in the Monte Carlo simulations described in this chapter). What clustering there would be is a difficult question, as the triangular lattice structure within the metal ion layers of $Fe_xNi_{1-x}Cl_2$ prevents the close packing of the ions with small ions neighbouring larger ones. As previously mentioned, clustering also appears to exist in the $CsMn_{1-x}Co_xCl_3.2H_2O$ system, where the lattice constants of the constituent antiferromagnets differ by only 2%.

However, the lattice constants for $FeCl_2$ and $CoCl_2$ are only 1% different, which should result in an even more random distribution of ions in the compound $Fe_{1-x}Co_xCl_2$, with little or no clustering of same-species ions. This idea is consistent with Mössbauer studies of the system (Howes *et al* 1984), which showed that only one phase is present in the mixed phase of the compound, as is the case with most mixed magnetic systems with competing magnetic anisotropy.

The following subsection describes the effects random fields have on mixed magnetic systems, which constitute another possible mechanism for the creation of coexisting magnetic order in $Fe_xNi_{1-x}Cl_2$.

5.5.1.2 Random fields.

Ising systems subject to random fields (with different magnitudes and orientations at each lattice site) were first considered in a detailed way by Imry and Ma (1975). They found that long range order is destroyed, and domains form with the spins in the up or down state. The direction of the average random field within a domain determines the magnetic order of that domain. The size of the domains are inversely proportional to the average magnitude of the random fields which act on the system.

These ideas were adapted by Wong *et al* (1983, 1980) to describe the mixed anti-ferromagnetic system $Fe_{1-x}Co_xCl_2$. Their neutron diffraction studies showed that lower magnetic transitions (from pure anti-ferromagnetic to mixed-magnetic phases) were broadened. However, both mean-field theory and renormalization group theory (RGT) predict sharp second-order transitions between the different magnetic phases, assuming simple Hamiltonians with only diagonal exchange and magnetic anisotropy terms (detailed in chapter 3). Wong *et al* accounted for the broadened transitions by noting that no lattice sites are strictly identical. Off-diagonal exchange constants could exist, and would have random values for each pair of interacting ions, resulting in a system with a random molecular field at each ionic site. Hence domains should form, with different magnetic order within each, which explains the neutron diffraction data. The non-diagonal exchange interactions could be comparable in magnitude to the exchange interactions, as the orbital moment in $Fe_{1-x}Co_xCl_2$ are not quenched (Katsumata *et al* 1985). Renormalization group studies working with Hamiltonians containing random off-diagonal exchange terms also support this view (Oku 1983). Howes *et al* (1984) also found this broadened behaviour using Mössbauer spectroscopy, with the lower phase transitions occurring over a 10 percent concentration range.

Katsumata *et al* (1992) used the same argument to explain coexisting magnetic order in the mixed system $Fe_{0.75}Co_{0.25}Br_2$, which has a magnetic phase diagram (and four phase structure) similar to that of $Fe_xNi_{1-x}Cl_2$. They performed neutron diffraction studies which again showed broadened lower magnetic transitions. They also detected coexisting order in the phase predicted by simple mean-field theory and RGT studies to be pure anti-ferromagnetic, with both Fe^{2+} and Co^{2+} spins oriented on average parallel to the easy axis of Fe^{2+} (the c axis). They explained this co-existence by assuming the random fields affecting the system had a non-zero average. They represented the non-diagonal exchange interactions between spins by the term $JS_{xy}^iS_z^j$ where J is the non-diagonal exchange integral (and is random from site to site). S_{xy}^i and S_z^j are the components of spins i, j in the xy plane or parallel to the c axis, respectively. If J has a non-zero

average, then ordering in the xy plane should create domains which order obliquely to the xy plane, with a non zero component along the c axis on average for the whole system (as opposed to zero on average if J had an average of zero). However, the authors did not offer an explanation for the non-zero average of J.

Elastic neutron diffraction studies have also been performed on the $Fe_xNi_{1-x}Cl_2$ system (Ito et al 1983). The phase line boundaries were quite sharp, but there was diffuse scattering at $x = 0.12$, which could indicate a coupling between the parallel and perpendicular spins components, as for the previously mentioned system in this section.

If random fields were creating the co-existing magnetic order observed in the mixed phase of $Fe_xNi_{1-x}Cl_2$ using Mössbauer spectroscopy, they would have to have a significant non-random average value, to create the two domain types observed. However, there is no mechanism for this. Even so, Monte Carlo simulations were performed with random distributions of ions, and random non-diagonal exchange interactions at each site were included. The resulting magnetic order in the mixed phase was simply the single phase predicted by mean-field theory and found previously in section 5.2.3. This was the case for a variety of maximum magnitudes for the random exchange interactions. Therefore random fields were rejected as a possible explanation for the complex magnetic order found in the mixed phase of $Fe_xNi_{1-x}Cl_2$.

5.6 Conclusions.

The Monte Carlo simulations described in this chapter indicate that the complex behaviour of Fe^{2+} and Ni^{2+} spins in the mixed magnetic phase of $Fe_xNi_{1-x}Cl_2$ cannot be accounted for by assuming a completely random distribution of metal ions. However, clusters of high Fe^{2+} content embedded in a low Fe^{2+} environment could create magnetic order similar to that observed experimentally using Mössbauer spectroscopy. This is in contrast to most other mixed magnetic systems that have been observed experimentally, which have one phase within the mixed region of their phase diagrams.

Chapter 6

Fitting of the Mössbauer spectra of $Fe_xNi_{1-x}Cl_2$.

6.1 Introduction.

As discussed in chapter 4, several single crystals of the mixed compound $Fe_xNi_{1-x}Cl_2$ were studied using Mössbauer spectroscopy, with the aim of determining the Fe spin behaviour in the mixed phase region of the magnetic phase diagram (since the behaviour in this phase has lead to disagreement in conclusions between two different groups). Although the concentrations of Fe within the prepared crystals did not all lie within that mixed phase, they all nevertheless help to determine the sizes and shapes of the various magnetic phases.

The different crystals were studied to determine their anti-ferromagnetic and paramagnetic behaviours, at low (typically less than $50\,K$) and high temperatures respectively. The following sections describe the Mössbauer spectra obtained for each crystal studied, and attempts to determine basic nuclear and electronic properties. This was done by comparing the experimentally obtained spectra with computed spectra, as discussed in chapter 2.

6.2 Mössbauer spectra for an $Fe_xNi_{1-x}Cl_2$ crystal with $x = 0.031$.

6.2.1 Paramagnetic spectra.

The quantities QS and IS discussed in this and the following sections are described in chapters 2 and 4. The fitted values of the electric quadrupole

splitting QS and the chemical isomer shift IS

T(K)	QS (mm/s)	IS (mm/s)	Γ (mm/s)
140	1.225(8)	1.159(4)	0.237(4)
130	1.228(7)	1.166(4)	0.236(8)
115	1.253(6)	1.175(3)	0.240(6)
100	1.245(6)	1.177(3)	0.235(6)
95	1.270(6)	1.190(3)	0.241(6)
90	1.264(6)	1.185(3)	0.236(6)
80	1.269(6)	1.188(3)	0.245(6)

Table 6.1: Nuclear quantities for an $Fe_xNi_{1-x}Cl_2$ crystal with $x = 0.031$ at paramagnetic temperatures. QS is the electric quadrupole splitting, IS is the isomer shift and Γ is the half width, as defined in chapter 2. The numbers in the brackets indicate the uncertainty in the last significant figure.

are listed in table 6.1 with uncertainties set equal to twice the statistical error for each quantity, which is a procedure adopted for all quantities quoted for the rest of this chapter. The set of parameters $EQVZ2$, η_{hf}, θ_{hf} and ϕ_{hf} are not determined unambiguously from magnetically split spectra, as Mössbauer spectra allow only 3 linear combinations of these variables to be determined. However, B_{hf} can be determined unambiguously (Karyagin 1966).

The quadrupole splittings QS are displayed graphically in figure 6.1 and the fitted and experimental Mössbauer spectra are shown in figure 6.2. The points in figure 6.2 are from the experimental spectra, and the continuous curves are the fitted spectra. This is also true for all of the other spectra displayed in this chapter. The crystal proved to be spectroscopically thin, with the area ratio between the large and small spectral lines being 2.5 on average. The spectra were fitted by allowing the variables α, QS, IS and Γ to vary, and compared well with the experimental spectra, using an average value for α of 20°. This effective α value accounts for misalignment between the incoming gamma rays and a line perpendicular to the crystal c axis, which corresponds with the principal electric field gradient axis since

there is no magnetic field at the nucleus on average. It also accounts for line broadening may have contributed to the line intensity ratio being less than the theoretical value of 3 (Bancroft 1973). The widths of the lines were only 0.24 mm/s on average, compared to a theoretical minimum value of $2\Gamma = 0.2$ mm/s. Therefore thickness broadening effects were small. The effects of thickness broadening would have been even less significant at lower temperatures, where the magnetic splitting lowers the divergence of the lines away from a Lorentzian shape.

This follows since the paramagnetic lines with particular depths split into a larger number of lines with smaller depths. Therefore deeper layers in the crystal will receive more radiation at velocities where absorption occurs, leading to less absorption saturation. The computed spectra were only very weakly dependent on the angle β, which was therefore set to zero and not varied.

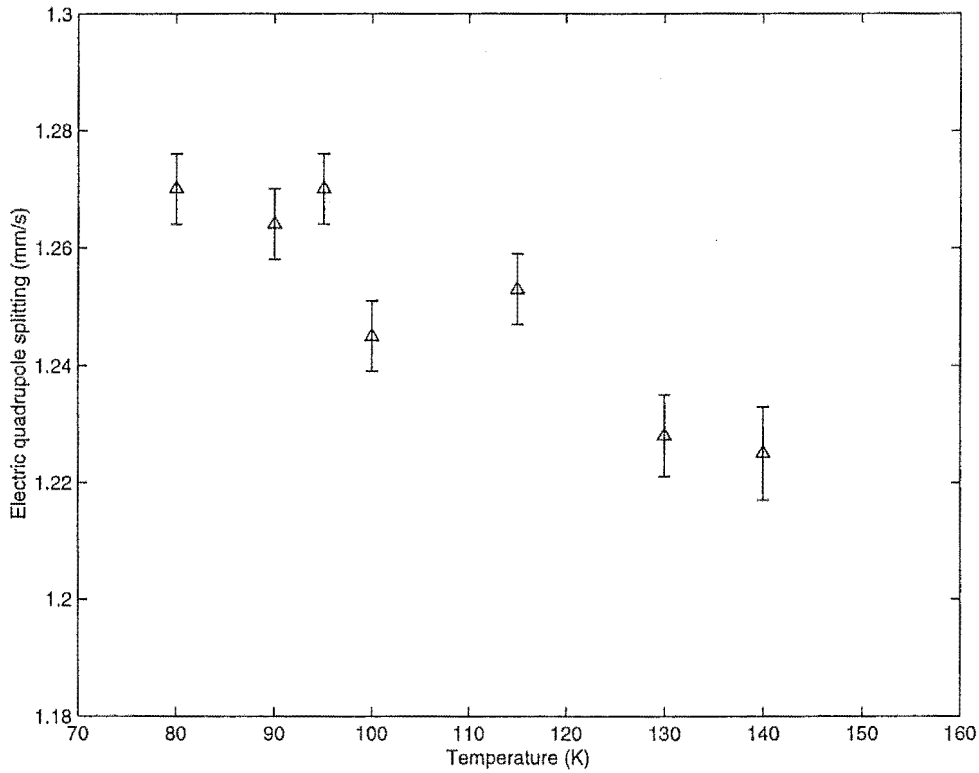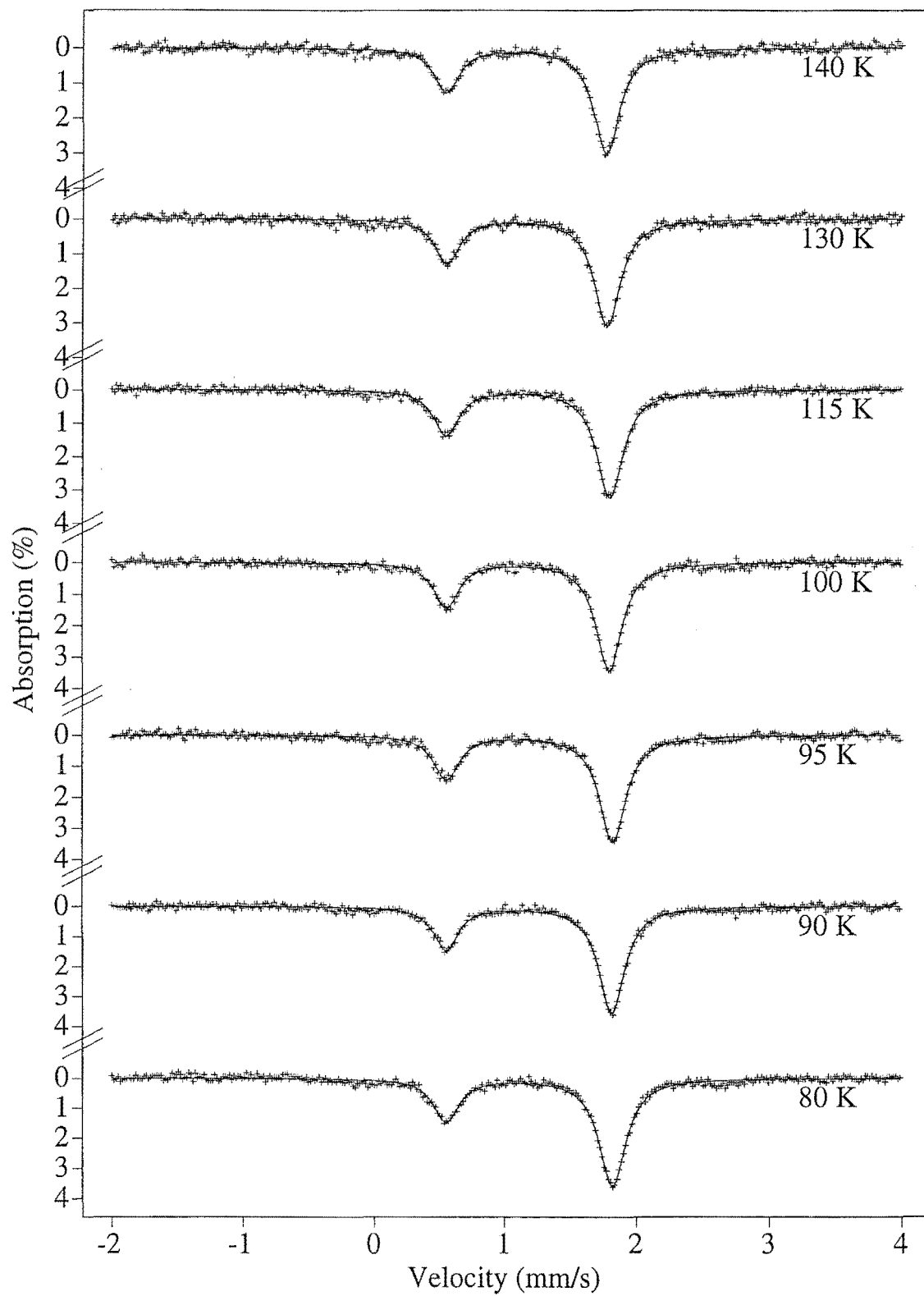Figure 6.1: Electric quadrupole splitting QS for $x = 0.031$ at paramagnetic temperatures.

Figure 6.2: Mössbauer and fitted spectra for an $Fe_xNi_{1-x}Cl_2$ crystal with $x = 0.031$ at paramagnetic temperatures.

6.2.2 Magnetic spectra.

The magnetic spectra for the $Fe_xNi_{1-x}Cl_2$ crystal with $x = 0.031$ were fitted in two different ways, to determine which of the two models for the mixed phase (Pollard *et al* (1991) and Tamaki and Ito (1991, 1993)) respectively, as discussed in chapter 1), give the best agreement with the experimental data. The models of Tamaki and Ito and Pollard *et al* are labelled models 1 and model 2 respectively.

Model 1 involves two co-existing sites in the mixed phase, which are both oblique to the c axis and the xy plane. Therefore a full set of parameters α, B_{hf}, $EQVZ2$, η, θ_{hf}, ϕ_{hf}, IS, Γ and Dip (quantities defined in chapter 4) were varied for each site. θ_{hf} was initially set to $20°$ and $65°$ - $90°$ for the two sites labelled site 1 and site 2, respectively.

Model 2 was more restricted, with the values for θ_{hf}, ϕ_{hf} and η all set permanently to zero for site 1, so that for this site B_{hf} was parallel to the principal z axis. The second site was fitted with all parameters allowed to vary, with θ_{hf} initially set to $85°$.

Figures 6.3 and 6.4 show the experimental vs fitted spectra for the two models. Figures 6.5 to 6.8 display graphically the electric quadrupole splitting and hyperfine magnetic fields computed for the two models, and figures 6.9 and 6.10 show the relative proportion of site 1 in each model. The important nuclear quantities obtained are listed in tables 6.2 and 6.3.

The populations of spins for either model which create a hyperfine magnetic field close to the c axis is termed population 1 (their magnetic site is labelled site 1). The other population which generated a hyperfine field near the xy plane is termed population 2 (with their magnetic site labelled site 2). This notation is followed for the rest of this chapter.

An attempt was made to eliminate any line broadening, if present. A variant on the program MOSCOR was used, based on ideas from Ure and Flinn (1971). Briefly, the absorption cross-section as a function of velocity was extracted from a Fourier analysis of each spectrum, which allowed ideal thin-absorber spectra to be constructed. However, the resulting spectra were insignificantly different in shape from the original ones, leading to nearly identical fits.

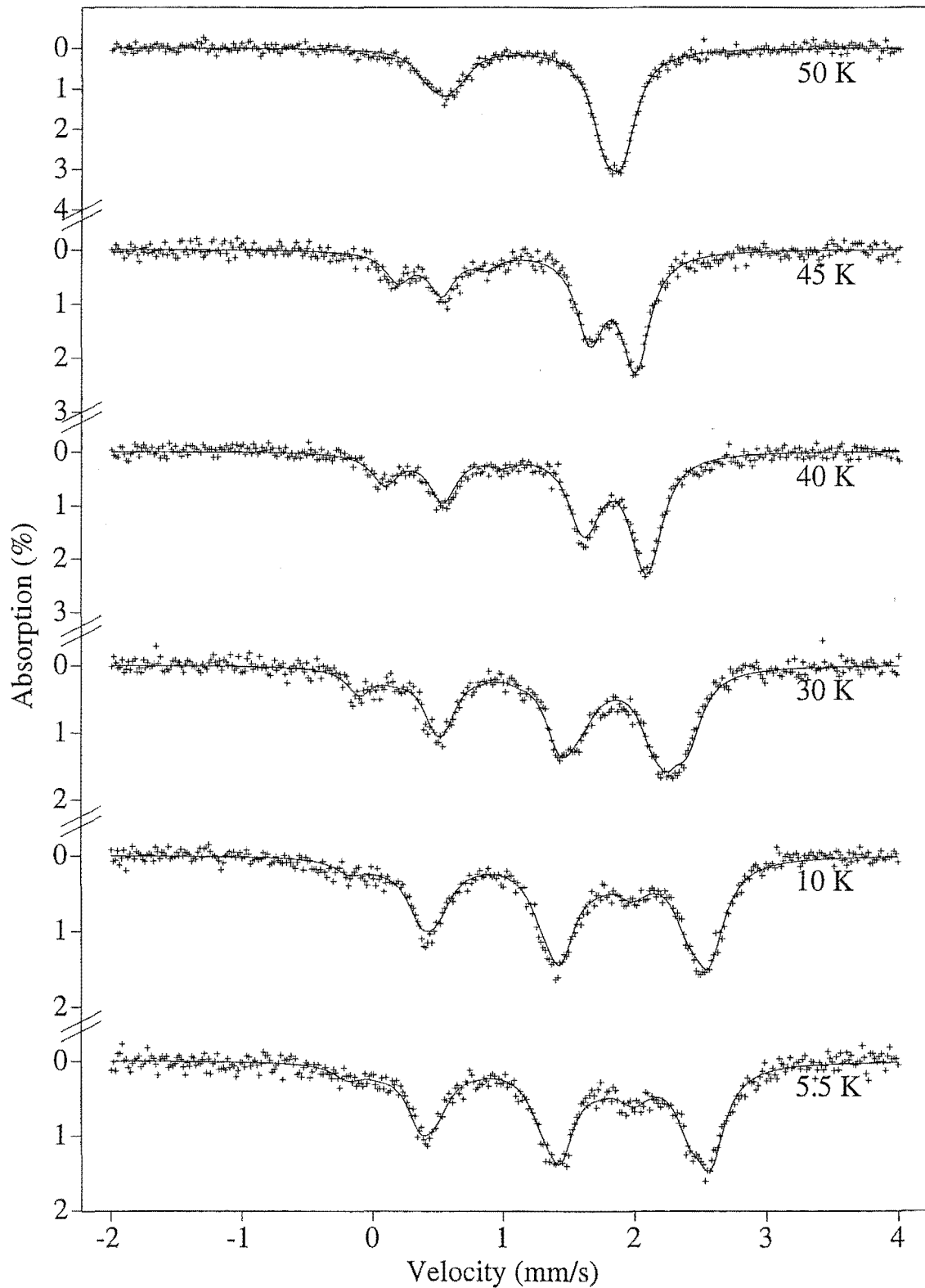Figure 6.3: Mössbauer and fitted spectra for an $Fe_xNi_{1-x}Cl_2$ crystal with $x = 0.031$ at magnetic temperatures: model 1.

Figure 6.4: Mössbauer and fitted spectra for an $Fe_xNi_{1-x}Cl_2$ crystal with $x = 0.031$ at magnetic temperatures: model 2.

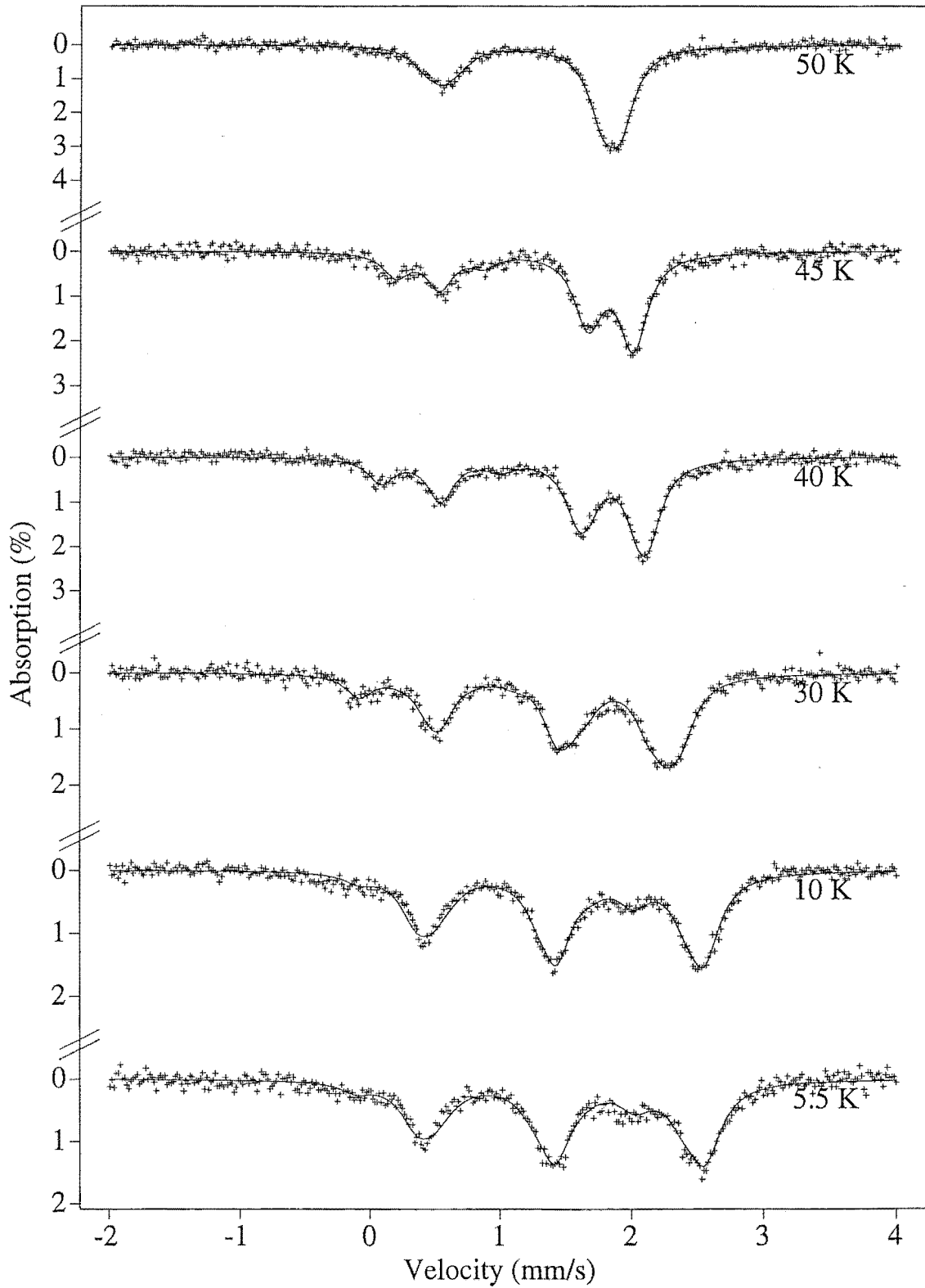Figure 6.5: Magnetic hyperfine field for an $Fe_xNi_{1-x}Cl_2$ crystal with $x = 0.031$: model 1.
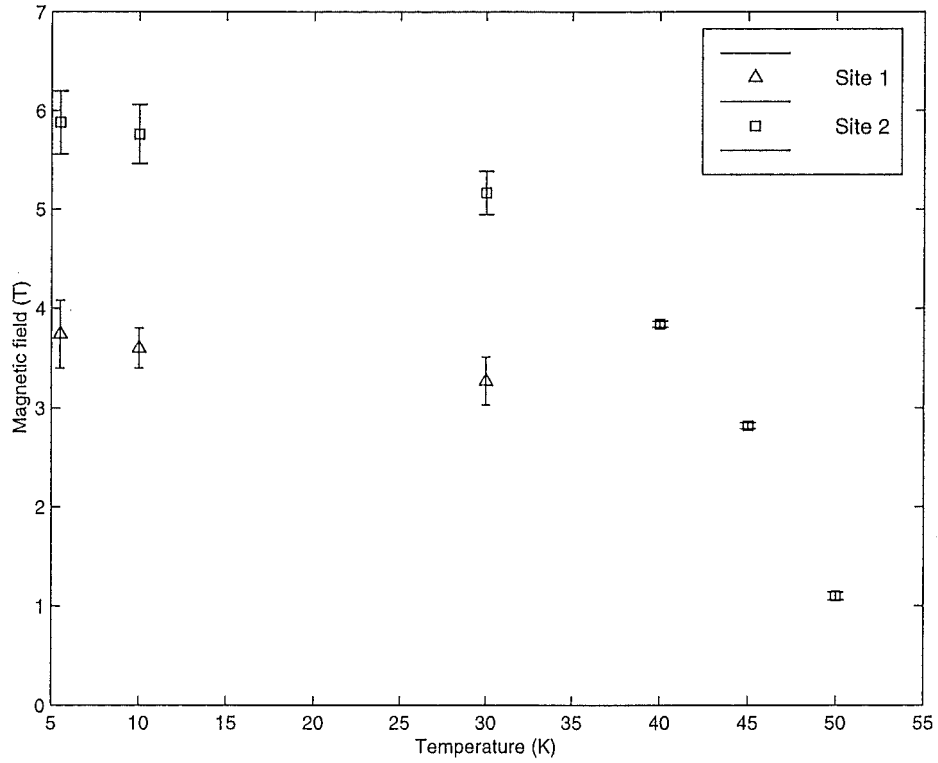
Figure 6.6: Magnetic hyperfine field for an $Fe_xNi_{1-x}Cl_2$ crystal with $x = 0.031$: model 2.
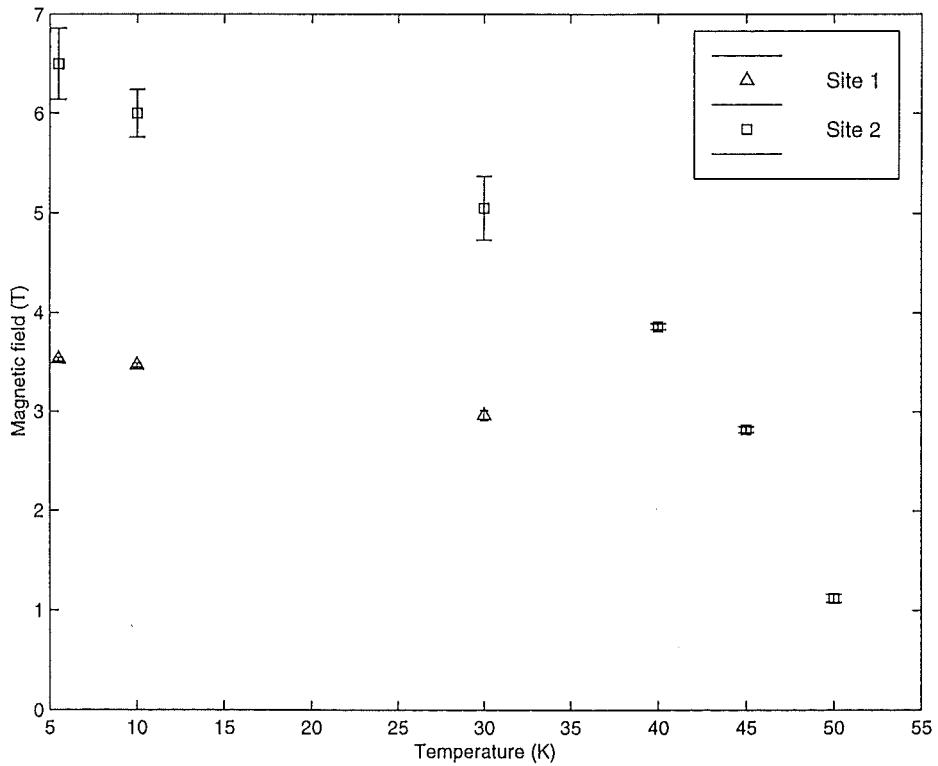
Figure 6.7: Electric quadrupole splitting factor QS for an $Fe_xNi_{1-x}Cl_2$ crystal with $x = 0.031$ at magnetic temperatures: model 1.
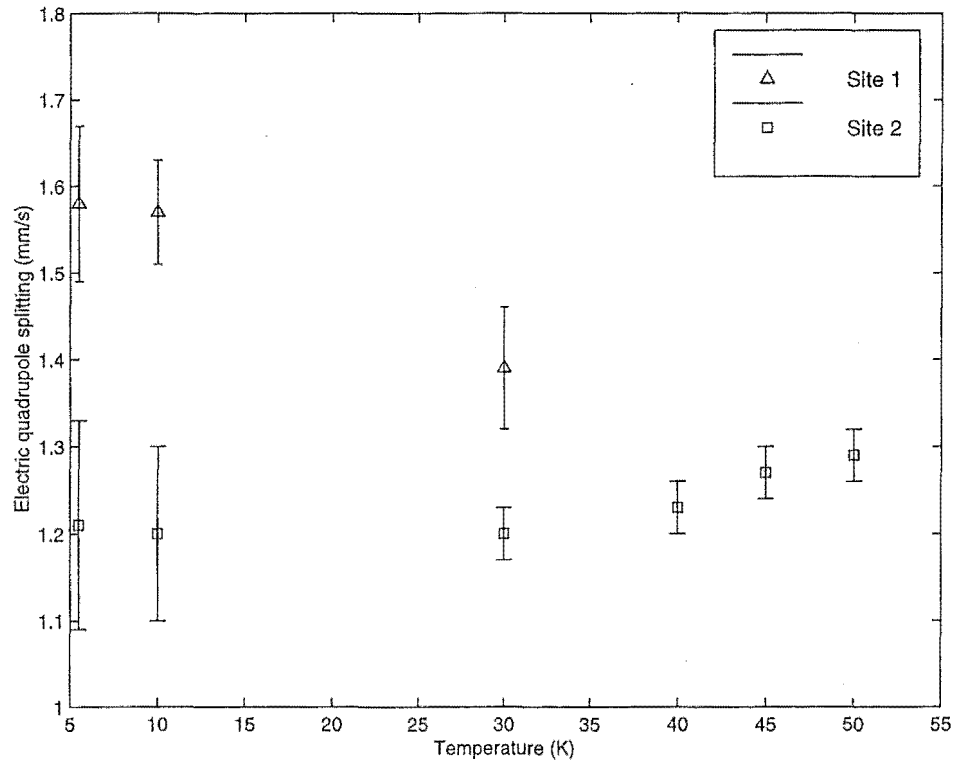
Figure 6.8: Electric quadrupole splitting factor QS for an $Fe_xNi_{1-x}Cl_2$ crystal with $x = 0.031$ at magnetic temperatures: model 2.
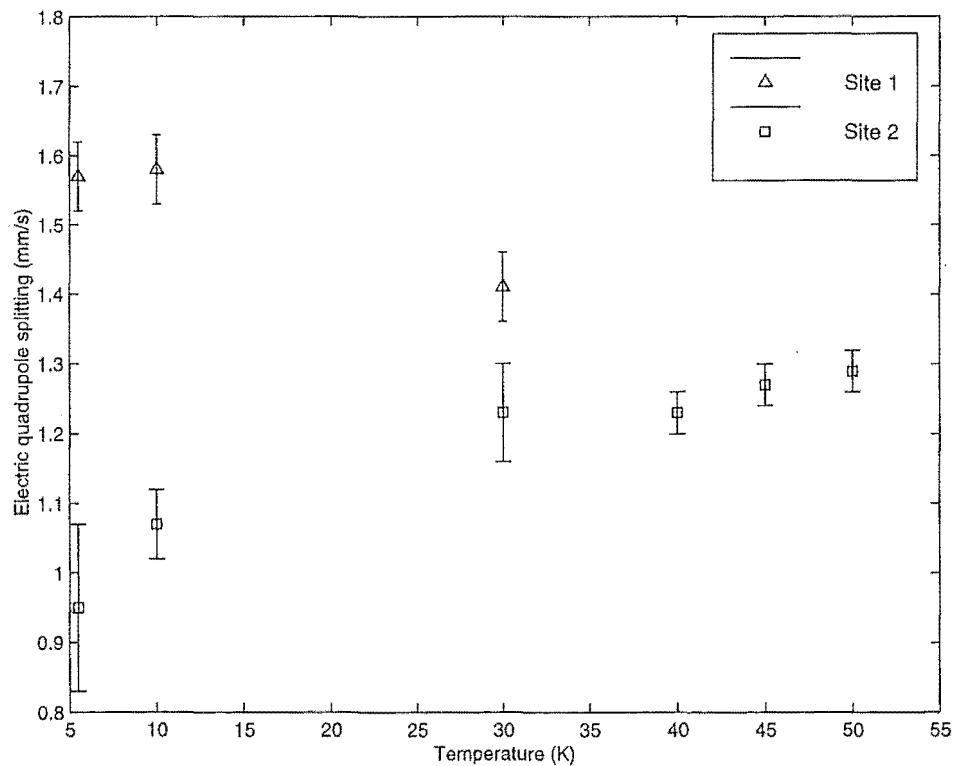
Figure 6.9: Relative proportion of spin population 1 for an $Fe_x Ni_{1-x} Cl_2$ crystal with $x = 0.031$ at magnetic temperatures: model 1.
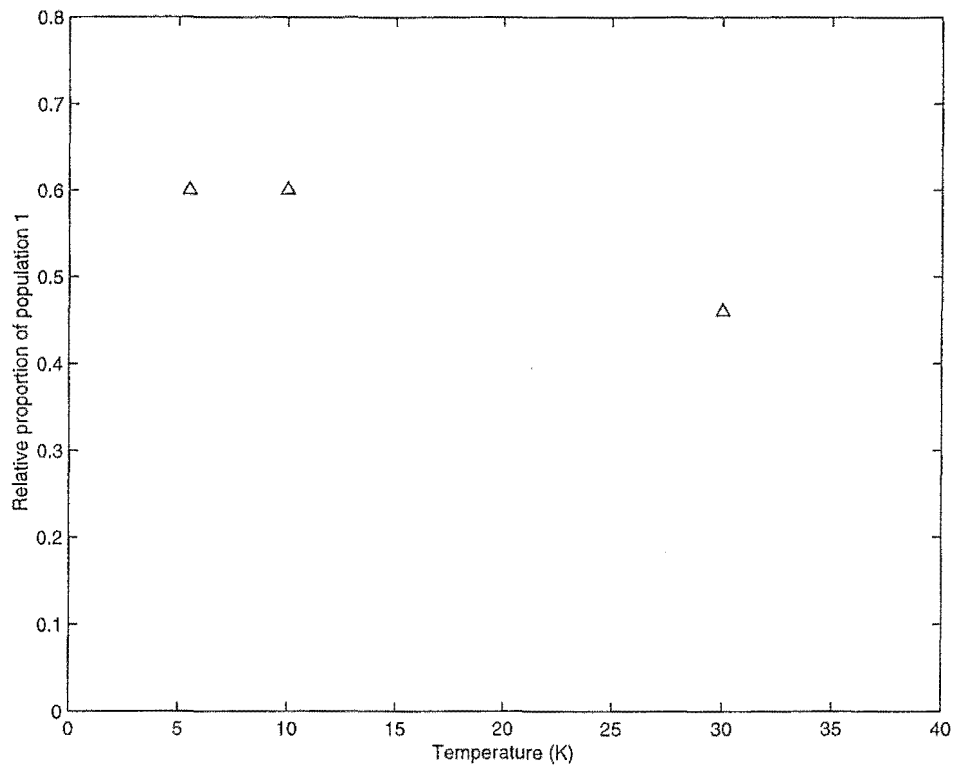
Figure 6.10: Relative proportion of spin population 2 for an $Fe_x Ni_{1-x} Cl_2$ crystal with $x = 0.031$ at magnetic temperatures: model 2.
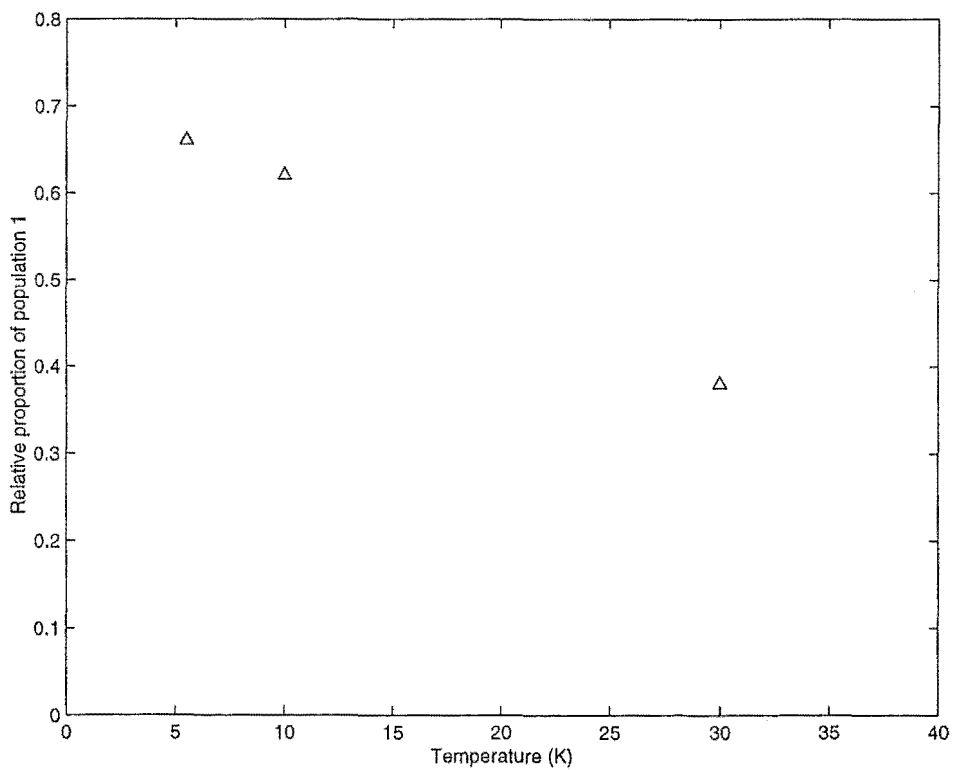
(Model 1) T(K)	B_{hf}(T)	QS(mm/s)	θ_{hf}($^\circ$)
50 (P2)	1.10(8)	1.29(3)	90(0)
45 (P2)	2.82(6)	1.27(3)	90(0)
40 (P2)	3.84(7)	1.23(3)	90(0)
30 (P1)	3.3(3)	1.39(7)	28(16)
30 (P2)	5.2(1)	1.2(3)	85(4)
10 (P1)	3.6(1)	1.57(6)	[17 to 19] (14)
10 (P2)	5.8(3)	1.2(1)	[61 to 69] (3)
5.5 (P1)	3.7(2)	1.58(9)	[21 to 24] (12)
5.5 (P2)	5.9(3)	1.2(1)	[62 to 70] (3)
(Model 2) T(K)	B_{hf}(T)	QS(mm/s)	θ_{hf}($^\circ$)
50 (P2)	1.12(8)	1.29(3)	90(0)
45 (P2)	2.82(6)	1.27(3)	90(0)
40 (P2)	3.86(6)	1.23(3)	90(0)
30 (P1)	2.96(9)	1.41(5)	0(0)
30 (P2)	5.1(3)	1.23(7)	[84 to 90] (3)
10 (P1)	3.47(3)	1.58(5)	0(0)
10 (P2)	6.0(2)	1.07(5)	85(0)
5.5 (P1)	3.53(4)	1.57(3)	0(0)
5.5 (P2)	6.5(3)	1.0(1)	85(0)

Table 6.2: Data obtained from the best fits to the spectra for a $Fe_x Ni_{1-x} Cl_2$ crystal with $x = 0.031$. Model 1 is that of Tamaki and Ito, and model 2 is that of Pollard *et al.* B_{hf} is the hyperfine magnetic field at the nucleus, QS is the quadrupole splitting and θ is the angle between the hyperfine field and the z axis of the principal axis system. P1 and P2 represents spin populations 1 and 2 respectively. The numbers in the curved brackets indicate the uncertainty in the last significant figure.

(Model 1) T(K)	IS(mm/s)	Γ(mm/s)	Relative area
50 (P2)	1.189(6)	0.25(1)	1.0
45 (P2)	1.179(6)	0.25(1)	1.0
40 (P2)	1.197(6)	0.26(1)	1.0
30 (P1)	1.21(1)	0.26(2)	0.46
30 (P2)	1.20(1)	0.25(3)	0.54
10 (P1)	1.21(2)	0.28(2)	0.62
10 (P2)	1.16(2)	0.28(2)	0.38
5.5 (P1)	1.21(3)	0.27(2)	0.60
5.5 (P2)	1.15(3)	0.27(2)	0.40
(Model 2) T(K)	IS(mm/s)	Γ(mm/s)	Relative area
50 (P2)	1.187(6)	0.25(1)	1.0
45 (P2)	1.179(6)	0.24(1)	1.0
40 (P2)	1.196(6)	0.25(1)	1.0
30 (P1)	1.20(1)	0.26(2)	0.38
30 (P2)	1.20(1)	0.26(2)	0.62
10 (P1)	1.20(1)	0.28(2)	0.62
10 (P2)	1.19(2)	0.28(2)	0.38
5.5 (P1)	1.21(2)	0.30(2)	0.66
5.5 (P2)	1.18(2)	0.29(2)	0.34

Table 6.3: Data obtained from the best fits to the spectra for a $Fe_xNi_{1-x}Cl_2$ crystal with $x = 0.031$. IS is the isomer shift, Γ is the half width of the absorption site and the relative area is the proportion of the total absorption spectrum due to a particular population of spins. P1 and P2 represents spin populations 1 and 2 respectively. The numbers in the brackets indicate the uncertainty in the last significant figure.

The angle α decreased from 20° to 2° for both models. Figures 6.3 and 6.4 show fitted spectra that are quite similar for the two models, both of which are close to the experimental spectra. Model 1 spectra were slightly more consistent with the experimental spectra, and in fact the angle θ_{hf} for site 2 in model 2 had to be set at most temperatures (indicated in tables 6.2 and 6.3 by a zero statistical error for θ_{hf}) or site 2 would become consistent with model 1. The angles θ_{hf} were significantly different for the two models below 30 K.

The main difference between the two models is in the behaviour of the electric quadrupole splittings at low temperatures, with the splittings decrease sharply for site 2 in model 2.

The difference between the fitted spectra generated from each model does not appear to be sufficient to state with certainty which model is better at modelling mixed magnetic behaviour for an $Fe_xNi_{1-x}Cl_2$ crystal for an Fe concentration of $x = 0.031$.

6.3 Mössbauer spectra for an $Fe_xNi_{1-x}Cl_2$ crystal with $x = 0.052$.

6.3.1 Paramagnetic spectra.

Table 6.4 lists nuclear quantities determined by a comparison between the experimental and fitted Mössbauer spectra, which are shown in figure 6.11. The spectrum for 130 K had to be truncated since an error in the recording process led to data corruption for many readings at negative detector velocities.

Again the spectral lines were narrow, with Γ equal to 0.24 mm/s on average. The area ratio between the two lines was found to be 2.6 on average. The effective value of α varied from 18° to 15° as temperature decreased. The electric quadrupole splittings are shown in figure 6.12.

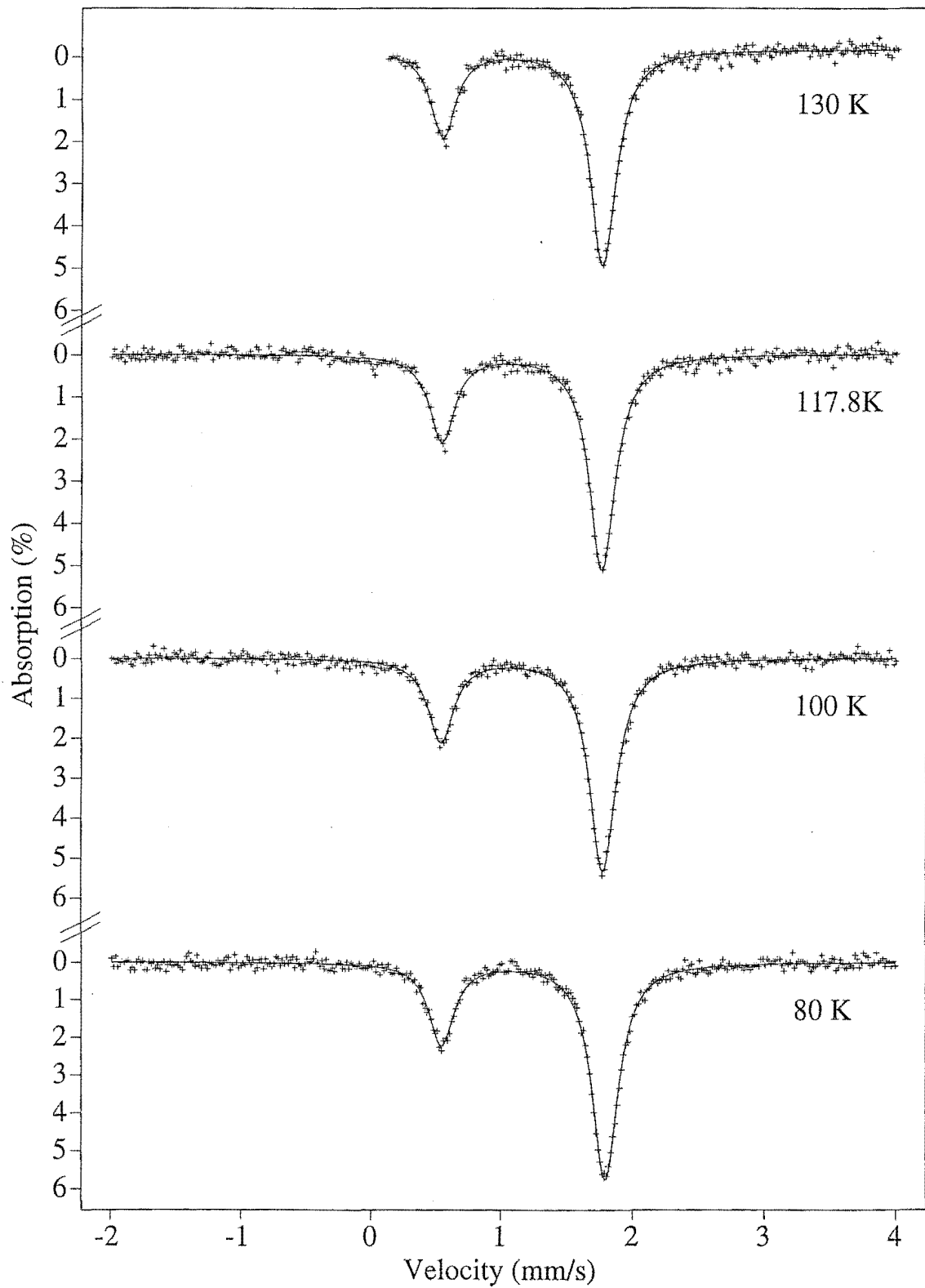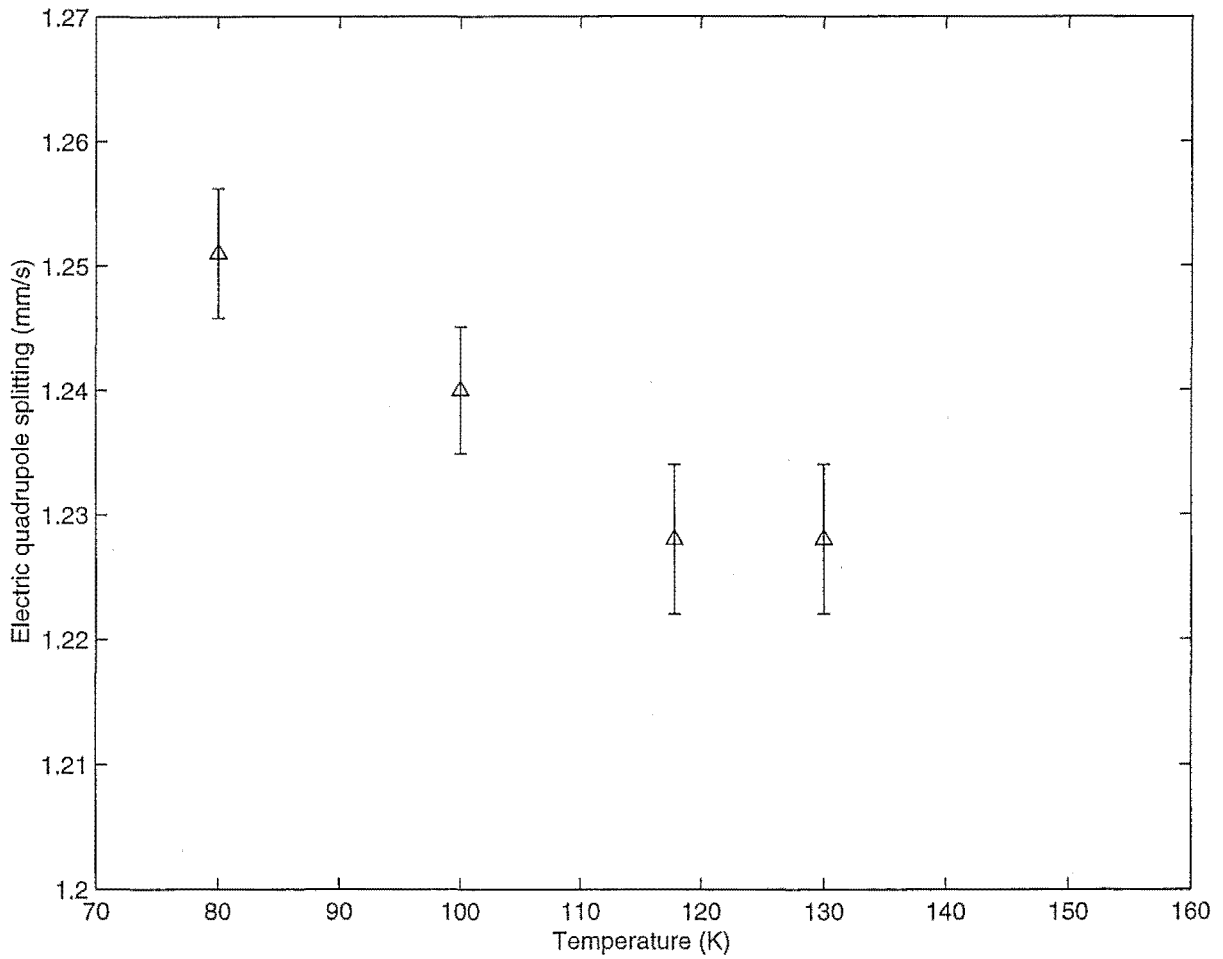Figure 6.11: Mössbauer and fitted spectra for an $Fe_xNi_{1-x}Cl_2$ crystal with $x = 0.052$ at paramagnetic temperatures.

Figure 6.12: Electric quadrupole splitting QS for an $Fe_xNi_{1-x}Cl_2$ crystal with $x = 0.052$ at paramagnetic temperatures.

T(K)	QS (mm/s)	IS (mm/s)	Γ (mm/s)
130	1.228(6)	1.158(4)	0.238(6)
117.8	1.228(6)	1.158(3)	0.238(1)
100	1.240(6)	1.161(3)	0.243(5)
80	1.251(5)	1.175(3)	0.238(5)

Table 6.4: Nuclear quantities for an $Fe_xNi_{1-x}Cl_2$ crystal with $x = 0.052$ at paramagnetic temperatures. QS is the electric quadrupole splitting, IS is the isomer shift and Γ is the half width, as defined in chapter 2. The numbers in the brackets indicate the uncertainty in the last significant figure.

6.3.2 Magnetic spectra.

Figures 6.13 and 6.14 show the fitted and experimental Mössbauer spectra for the crystal, for model 1 and 2 respectively. The magnetic hyperfine fields are shown in Figures 6.15 and 6.16, and the electric quadrupole splittings are shown in figures 6.17 and 6.18. Finally, the relative proportion of population 1 in the total Mössbauer spectra are shown in figures 6.19 and 6.20. The nuclear quantities of interest derived from these spectra are listed in tables 6.5 and 6.6. Again, the two models generated spectra which were similar. Both showed similar discrepancies between fitted and experimental spectra.

However, in this case, the angle θ_{hf} for models 1 and 2, for both sites 1 and 2, were very close. This was also true of the other hyperfine quantities shown in figures 6.5 and 6.6, and the relative proportions of spin populations 1 and 2. Also, both models required values of α which decreased from 20° to 2° as temperature decreased.

Hence, within the statistical errors (and taking into account ambiguities in the nuclear data), it is difficult to distinguish the models at all. From either model, it can be concluded that the angles between the magnetic hyperfine fields, and the z axis of the principal axis system, are close to 0° and 90° for sites 1 and 2, respectively. This data is consistent with the magnetic order being along or close to the crystalline c axis and xy planes for sites 1 and 2 respectively, as mentioned previously (see chapter 1).

6.3. Mössbauer spectra for an $Fe_xNi_{1-x}Cl_2$ crystal with $x = 0.052$.

101

Figure 6.13: Mössbauer and fitted spectra for an $Fe_xNi_{1-x}Cl_2$ crystal with $x = 0.052$ at magnetic temperatures: model 1.
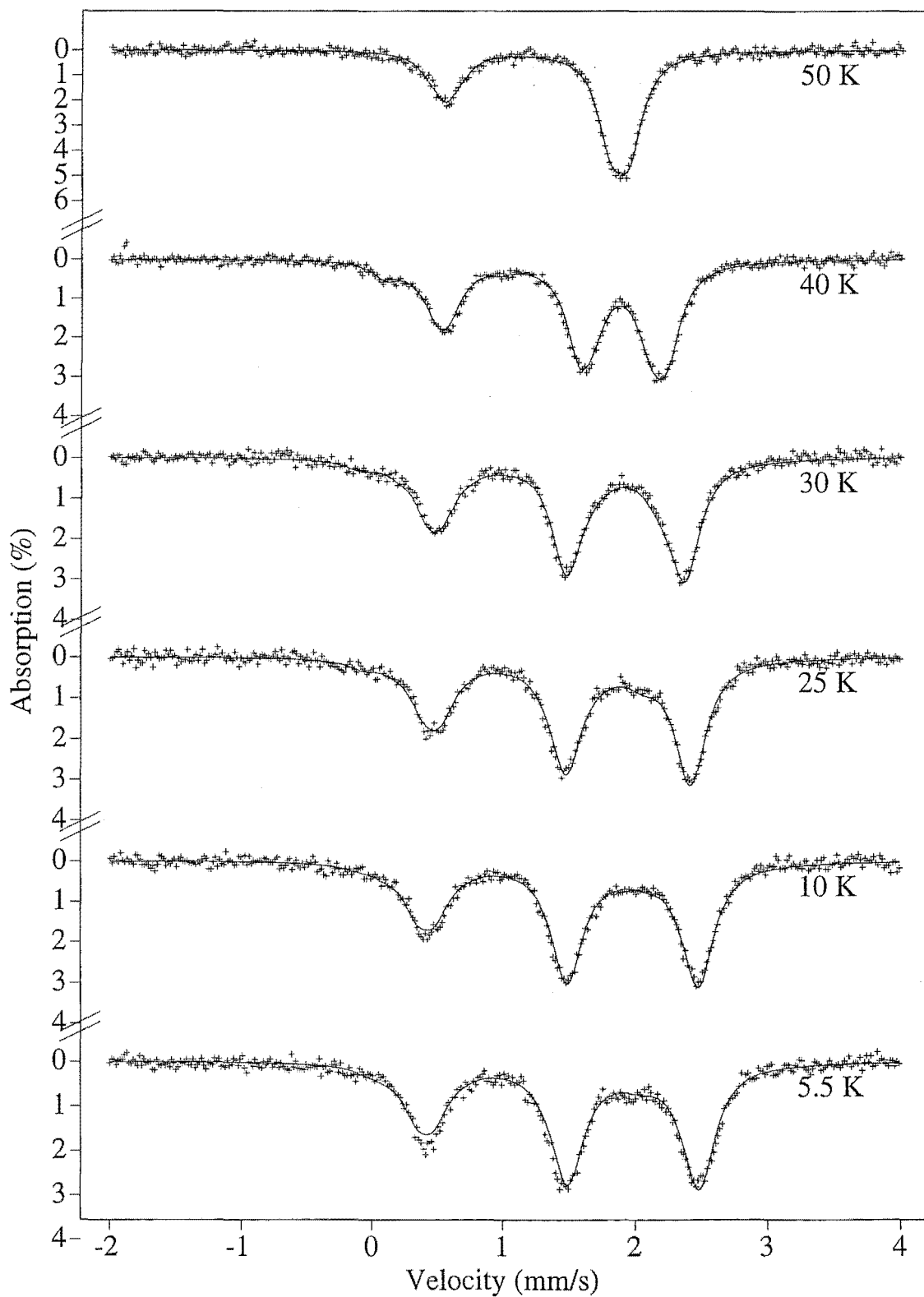
Figure 6.14: Mössbauer and fitted spectra for an $Fe_xNi_{1-x}Cl_2$ crystal with $x = 0.052$ at magnetic temperatures: model 2.
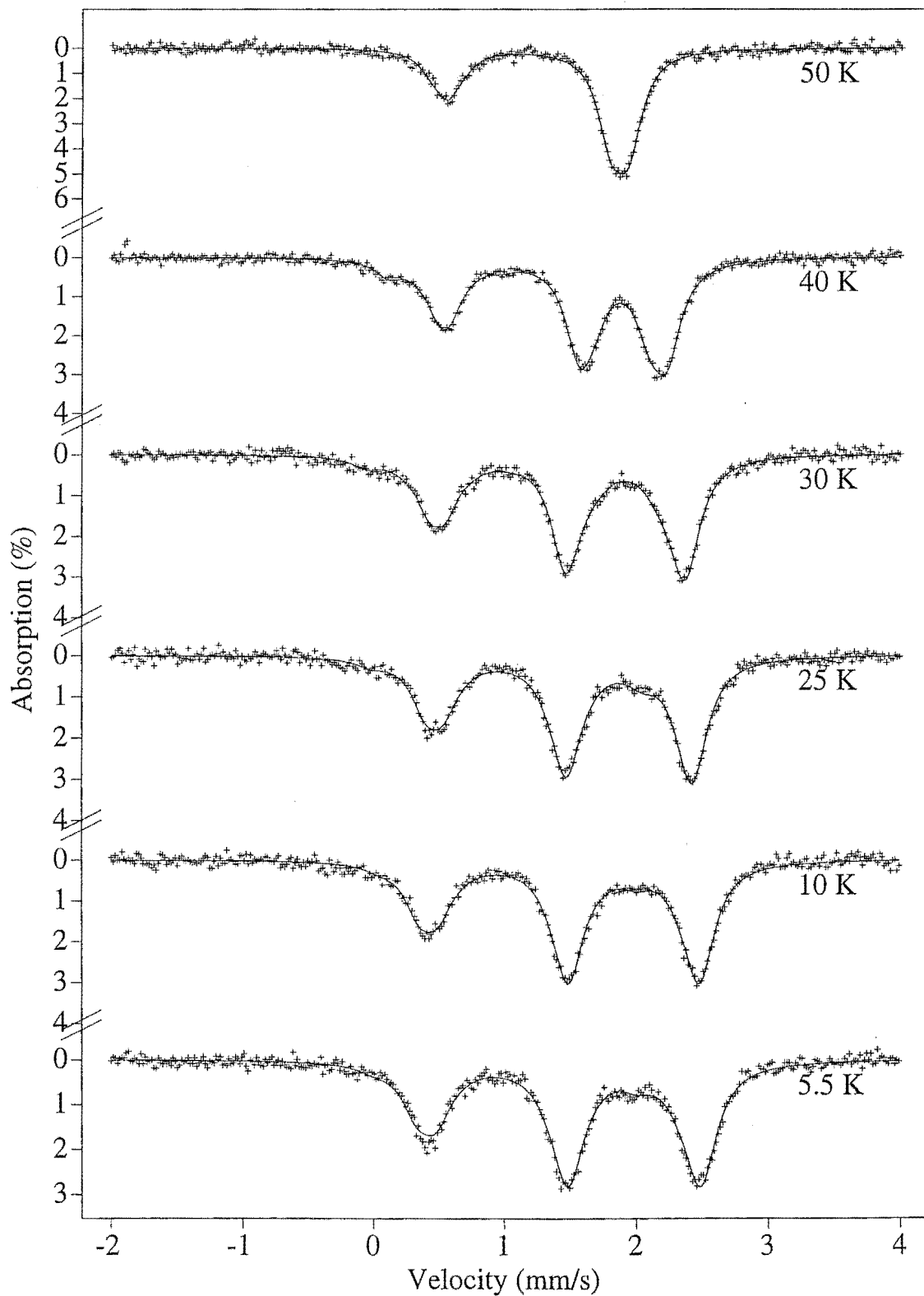
Figure 6.15: Magnetic hyperfine field for an $Fe_xNi_{1-x}Cl_2$ crystal with $x = 0.052$: model 1.
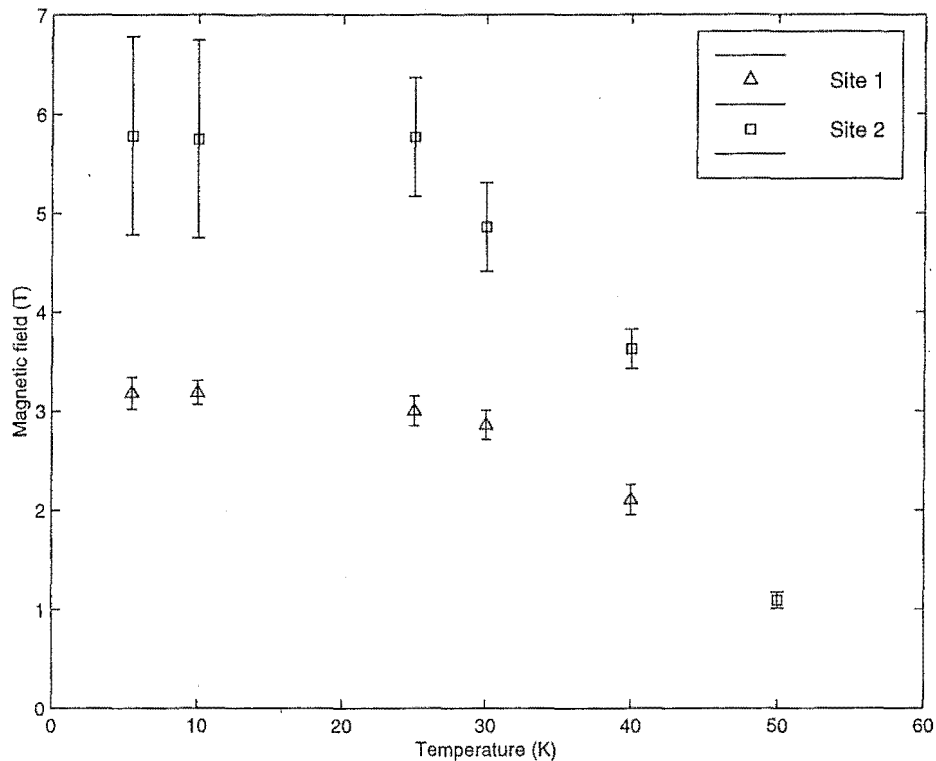
Figure 6.16: Magnetic hyperfine field for an $Fe_xNi_{1-x}Cl_2$ crystal with $x = 0.052$: model 2.
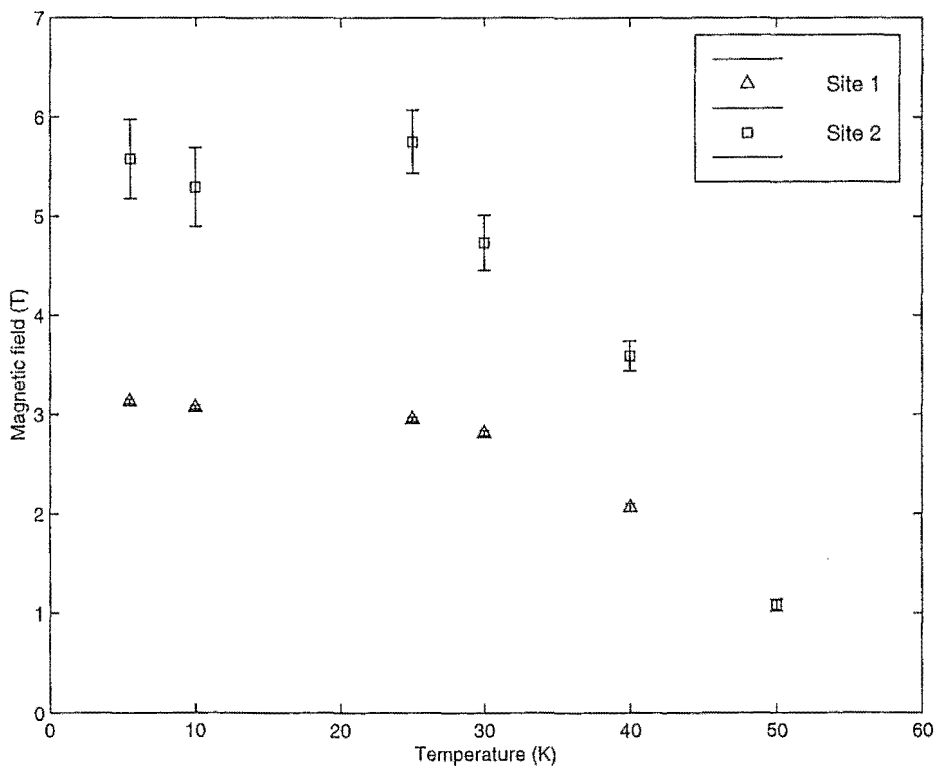
Figure 6.17: Electric quadrupole splitting QS for an $Fe_xNi_{1-x}Cl_2$ crystal with $x = 0.052$ at magnetic temperatures: model 1.
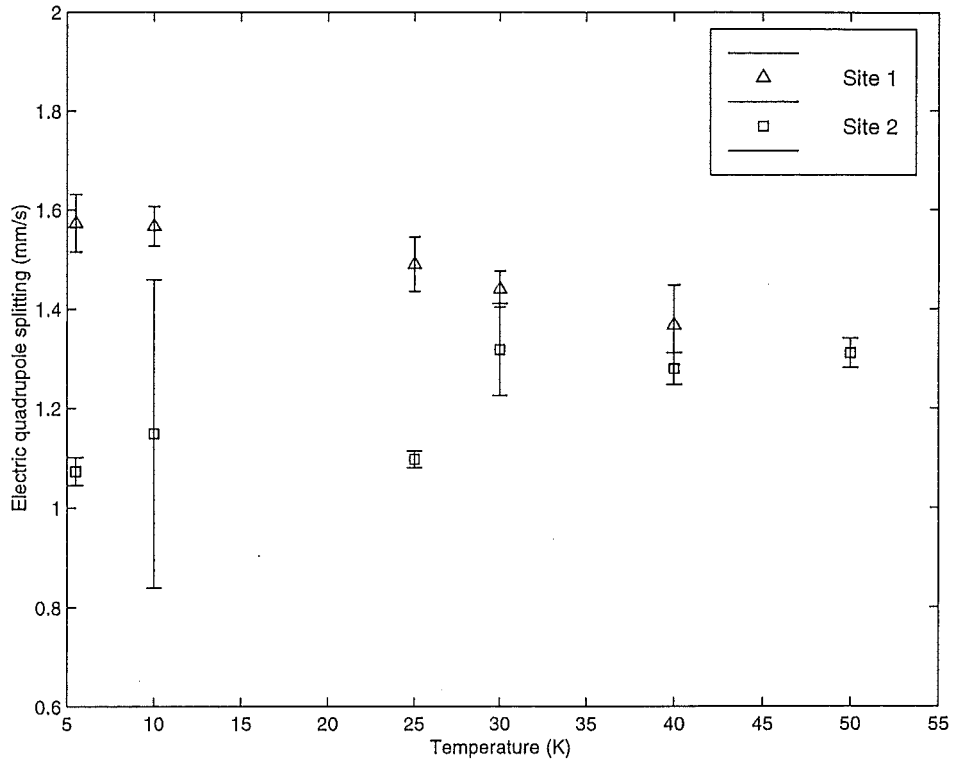
Figure 6.18: Electric quadrupole splitting QS for an $Fe_xNi_{1-x}Cl_2$ crystal with $x = 0.052$ at magnetic temperatures: model 2.
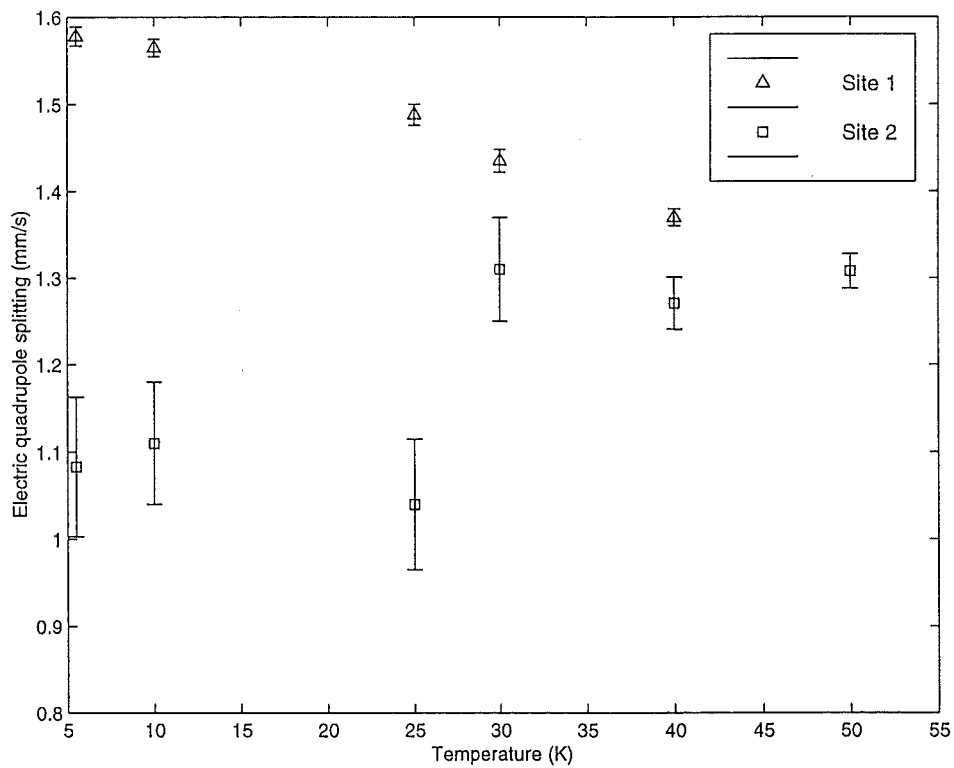
Figure 6.19: Relative proportion of spin population 1 for an $Fe_xNi_{1-x}Cl_2$ crystal with $x = 0.052$ at magnetic temperatures: model 1.
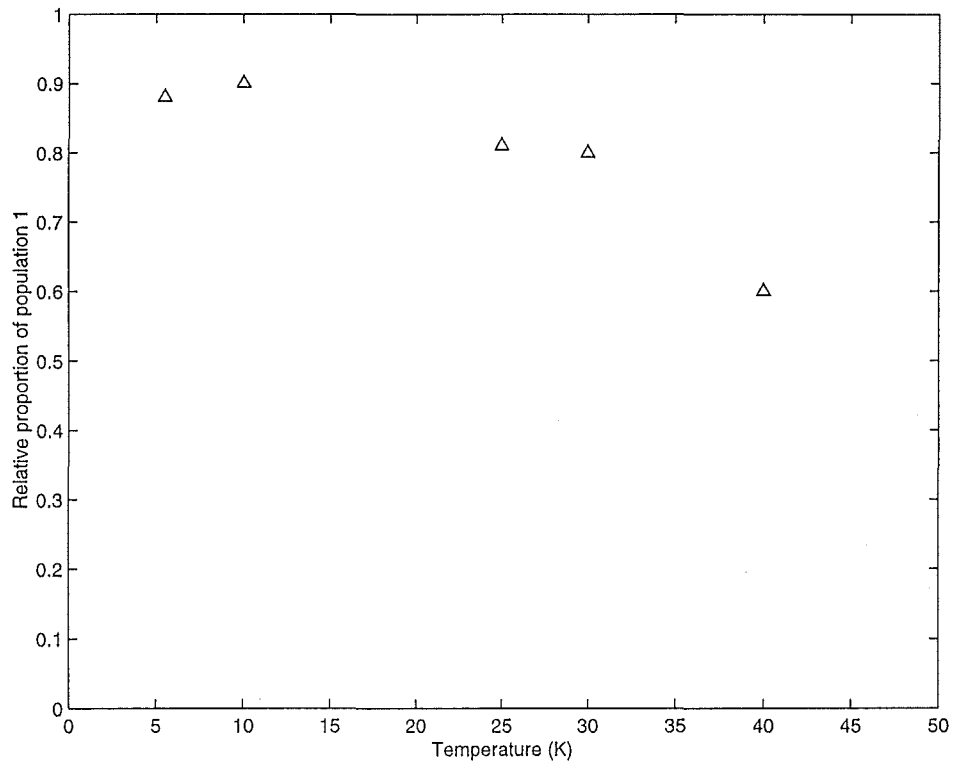
Figure 6.20: Relative proportion of spin population 1 for an $Fe_xNi_{1-x}Cl_2$ crystal with $x = 0.052$ at magnetic temperatures: model 2.
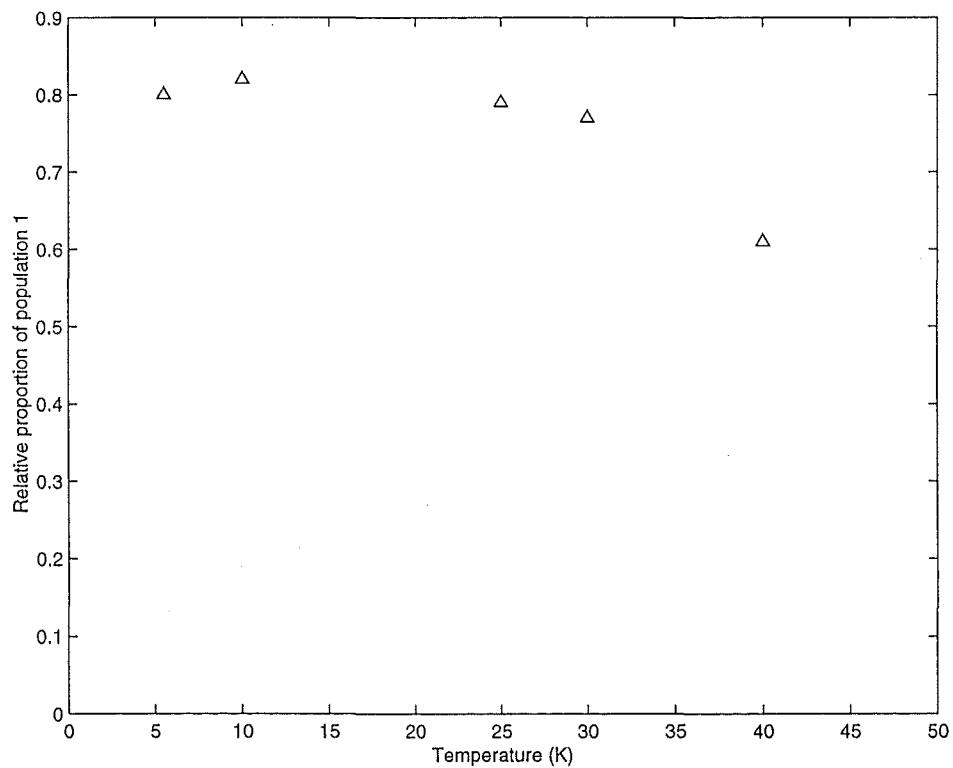
(Model 1) T(K)	B_{hf}(T)	QS(mm/s)	θ_{hf}(°)
50 (P2)	1.09(8)	1.31(3)	90(0)
40 (P1)	2.1(1)	1.37(8)	[12 to 16] (20)
40 (P2)	3.6(2)	1.28(3)	90(0)
30 (P1)	2.9(1)	1.44(4)	[16 to 17] (14)
30 (P2)	4.9(4)	1.32(9)	87(15)
25 (P1)	3.0(1)	1.49(6)	[14 to 16] (12)
25 (P2)	5.8(6)	1.10(2)	[78 to 86] (7)
10 (P1)	3.2(1)	1.57(4)	[17 to 20] (8)
10 (P2)	6(1)	1.15(31)	[77 to 89] (11)
5.5 (P1)	3.2(2)	1.57(6)	[16 to 18] (12)
5.5 (P2)	6(1.0)	1.07(3)	[80 to 86] (22)
(Model 2) T(K)	B_{hf}(T)	QS(mm/s)	θ_{hf}(°)
50 (P2)	1.08(6)	1.31(2)	90(0)
40 (P1)	2.07(4)	1.37(1)	0(0)
40 (P2)	3.6(1)	1.27(3)	90(10)
30 (P1)	2.81(3)	1.44(1)	0(0)
30 (P2)	4.7(3)	1.31(6)	85(0)
25 (P1)	2.95(2)	1.49(1)	0(0)
25 (P2)	5.8(3)	1.04(8)	85(0)
10 (P1)	3.07(2)	1.57(1)	0(0)
10 (P2)	5.3(4)	1.11(7)	85(0)
5.5 (P1)	3.13(2)	1.58(1)	0(0)
5.5 (P2)	5.6(4)	1.08(8)	85(0)

Table 6.5: Data obtained from the best fits to the spectra for a $Fe_xNi_{1-x}Cl_2$ crystal with $x = 0.052$. B_{hf} is the hyperfine magnetic field at the nucleus, QS is the quadrupole splitting and θ is the angle between the hyperfine field and the z axis of the principal axis system. P1 and P2 represents spin populations 1 and 2 respectively. The numbers in the curved brackets indicate the uncertainty in the last significant figure.

(Model 1) T(K)	IS(mm/s)	Γ(mm/s)	Relative area
50 (P2)	1.211(4)	0.24(1)	1.0
40 (P1)	1.21(1)	0.25(1)	0.60
40 (P2)	1.21(1)	0.25(1)	0.40
30 (P1)	1.20(1)	0.27(1)	0.80
30 (P2)	1.19(2)	0.27(1)	0.20
25 (P1)	1.204(6)	0.28(1)	0.81
25 (P2)	1.204(6)	0.28(1)	0.19
10 (P1)	1.197(5)	0.28(1)	0.91
10 (P2)	1.197(5)	0.28(2)	0.09
5.5 (P1)	1.199(7)	0.29(2)	0.88
5.5 (P2)	1.199(7)	0.29(2)	0.12
(Model 2) T(K)	IS(mm/s)	Γ(mm/s)	Relative area
50 (P2)	1.21(1)	0.23(1)	1.0
40 (P1)	1.21(1)	0.25(1)	0.61
40 (P2)	1.21(1)	0.25(1)	0.39
30 (P1)	1.20(1)	0.26(1)	0.77
30 (P2)	1.21(1)	0.26(1)	0.23
25 (P1)	1.21(1)	0.27(1)	0.79
25 (P2)	1.21(1)	0.27(1)	0.21
10 (P1)	1.20(1)	0.28(1)	0.82
10 (P2)	1.20(1)	0.28(1)	0.18
5.5 (P1)	1.20(1)	0.29(1)	0.80
5.5 (P2)	1.20(1)	0.29(1)	0.20

Table 6.6: Data obtained from the best fits to the spectra for a $Fe_x Ni_{1-x} Cl_2$ crystal with $x = 0.052$. IS is the isomer shift, Γ is the half width of the absorption site and the relative area is the proportion of the total absorption spectrum due to a particular population of spins. P1 and P2 represents spin populations 1 and 2 respectively. The numbers in the brackets indicate the uncertainty in the last significant figure.

6.4 Mössbauer spectra for $x = 0.15$

6.4.1 Paramagnetic spectra.

Table 6.7 lists the quantities of interest derived from the paramagnetic spectra of the crystal. The linewidths were noticeably larger than was the case with the previous two Fe concentrations within $Fe_xNi_{1-x}Cl_2$ absorbers. The average value of the effective angle α was 24° this time, indicating thickness effects were more important with this sample. Figure 6.21 shows the fitted vs experimental spectra for the crystal, while figure 6.22 shows the electric quadrupole splittings as a function of temperature.

T(K)	QS (mm/s)	IS (mm/s)	Γ (mm/s)
150	1.18(1)	1.136(2)	0.26(2)
130	1.26(1)	1.166(4)	0.26(1)
120	1.26(5)	1.170(3)	0.27(1)
110	1.28(1)	1.177(4)	0.25(1)
100	1.29(1)	1.178(3)	0.25(1)
90	1.29(1)	1.187(3)	0.26(1)
80	1.29(1)	1.190(3)	0.26(1)
55	1.30(1)	1.195(4)	0.26(1)

Table 6.7: Nuclear quantities for an $Fe_xNi_{1-x}Cl_2$ crystal with $x = 0.15$ at paramagnetic temperatures. QS is the electric quadrupole splitting, IS is the isomer shift and Γ is the half width as defined in chapter 2. The numbers in the brackets indicate the uncertainty in the last significant figure.

Figure 6.21: Mössbauer and fitted spectra for an $Fe_xNi_{1-x}Cl_2$ crystal with $x = 0.15$ at paramagnetic temperatures.
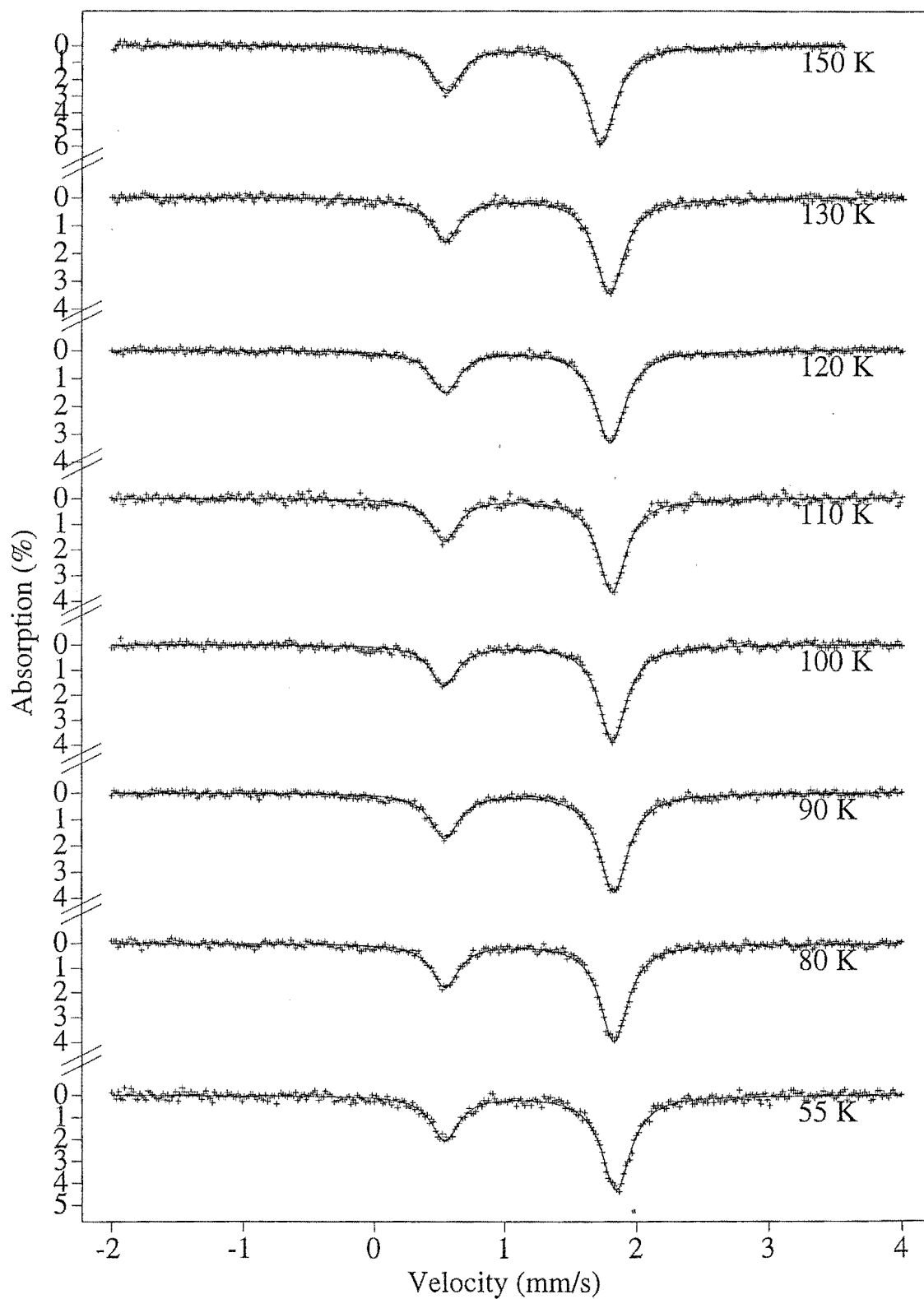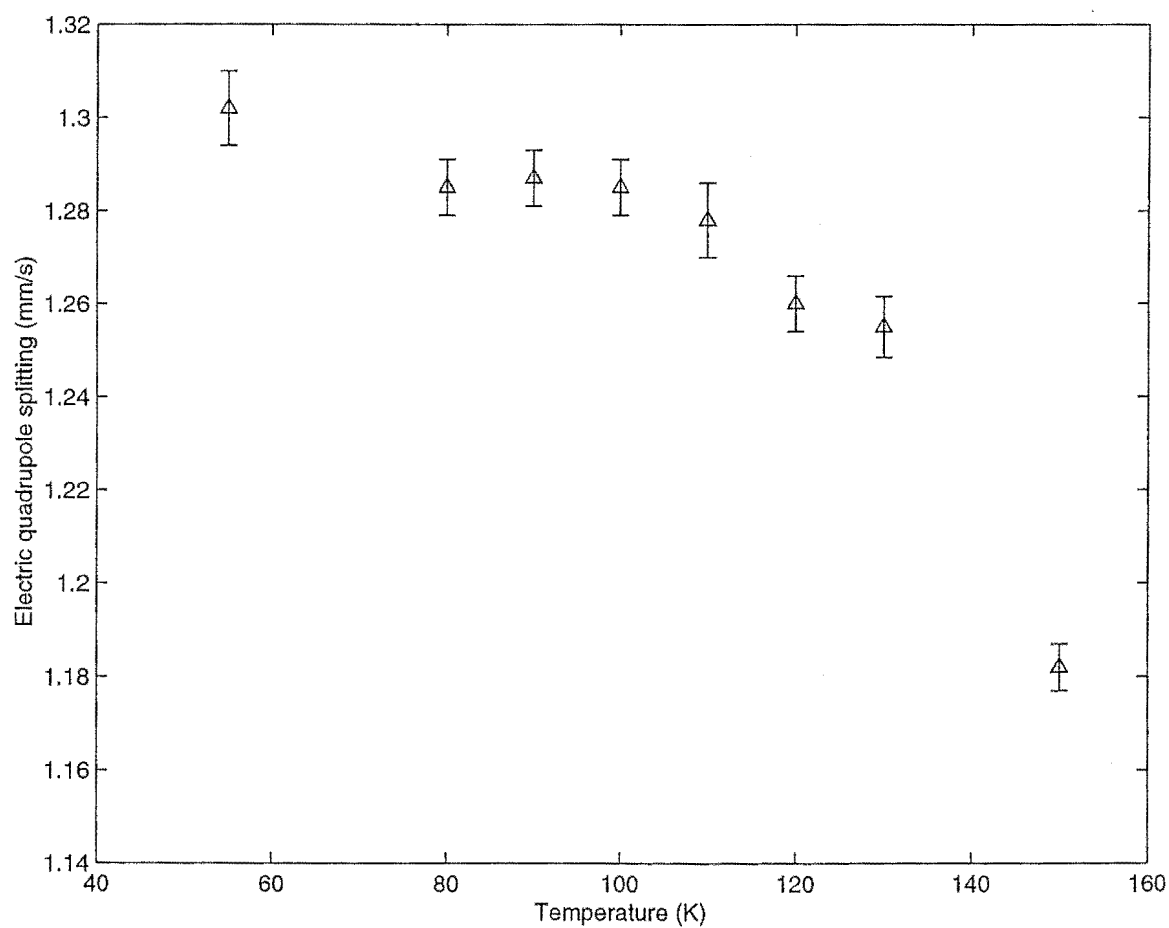
Figure 6.22: Electric quadrupole splitting QS for an $Fe_xNi_{1-x}Cl_2$ crystal with $x = 0.15$ at paramagnetic temperatures.

6.4.2 Magnetic spectra.

Sample thickness corrections were introduced, but again gave insignificant changes to the experimental Mössbauer spectra.

Models 1 and 2 this time involved only one site, with the hyperfine magnetic field close to the z axis of the principal axis system (i.e. site 1). The two models gave results that were not distinguishable at any temperature, and therefore this section lists only the results from model 2. These results are listed in table 6.8. Figure 6.23 displays the fitted and experimental spectra, and figures 6.24 and 6.25 shows the fitted values of magnetic hyperfine fields and electric quadrupole splittings respectively.

Clearly, the best fit to the spectra involved magnetic order along the z axis of the principal axis system, which is consistent with magnetic order along the crystalline c axis only.

T(K)	B_{hf}(T)	QS(mm/s)	IS(mm/s)	Γ(mm/s)
45	1.02(1)	1.35(1)	1.207(5)	0.30(1)
40	1.90(1)	1.36(1)	1.207(4)	0.29(1)
30	2.62(3)	1.45(1)	1.207(6)	0.30(1)
20	2.83(2)	1.51(1)	1.202(5)	0.31(1)
10	2.83(2)	1.54(1)	1.194(6)	0.29(1)
5.5	2.83(2)	1.54(1)	1.194(6)	0.29(1)

Table 6.8: Data obtained from the best fits to the spectra for a $Fe_xNi_{1-x}Cl_2$ crystal using model 2, with $x = 0.15$. B_{hf} is the hyperfine magnetic field at the nucleus, QS is the quadrupole splitting, IS is the isomer shift and Γ is the half width. Only spin population 1 exists. θ_{hf} is fixed at zero. The numbers in the brackets indicate the uncertainty in the last significant figure.

Figure 6.23: Mössbauer and fitted spectra for an $Fe_xNi_{1-x}Cl_2$ crystal with $x = 0.15$ at magnetic temperatures: model 2.
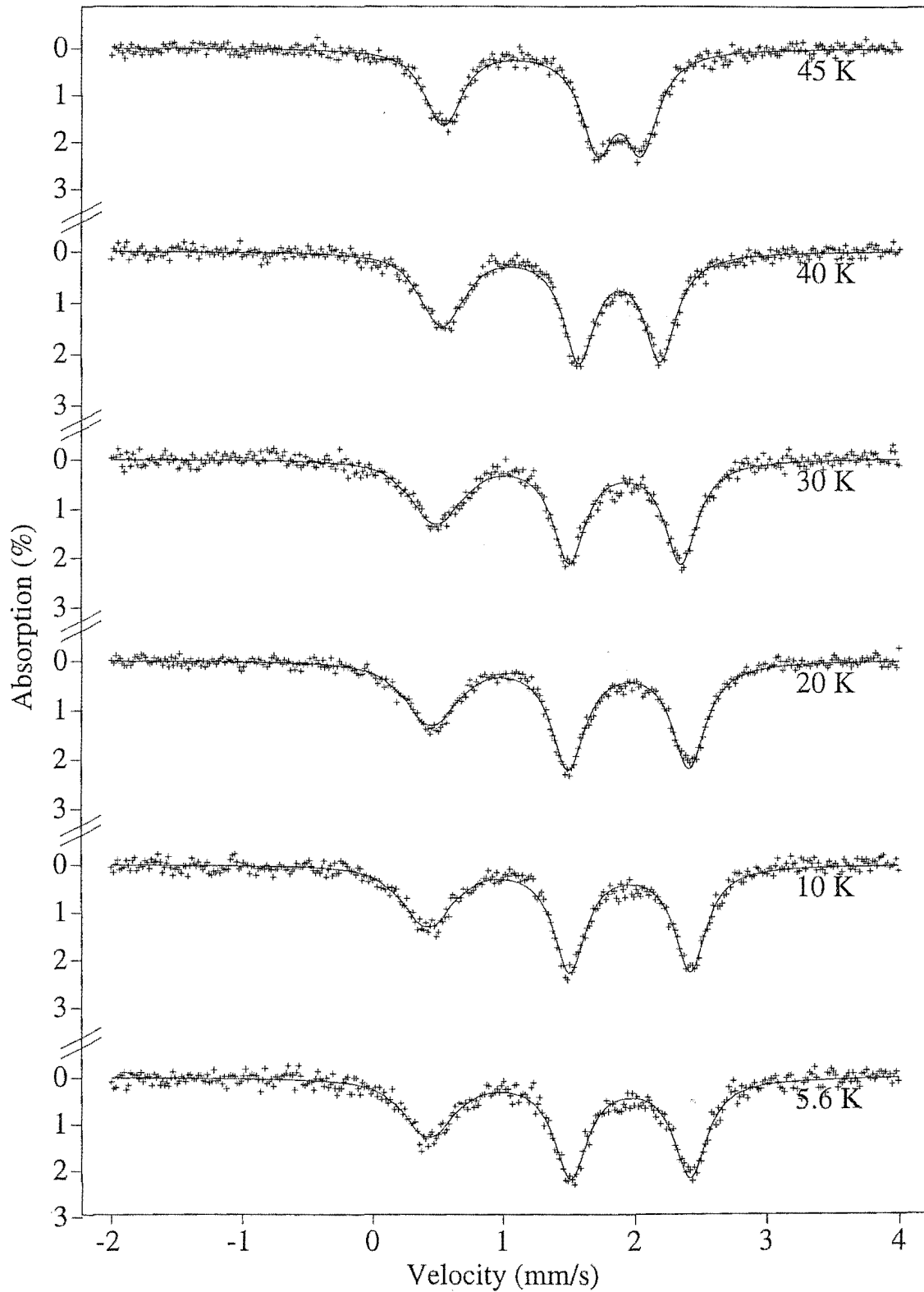
Figure 6.24: Magnetic hyperfine field for an $\mathrm{Fe}_x\mathrm{Ni}_{1-x}\mathrm{Cl}_2$ crystal with $x = 0.15$: model 2.
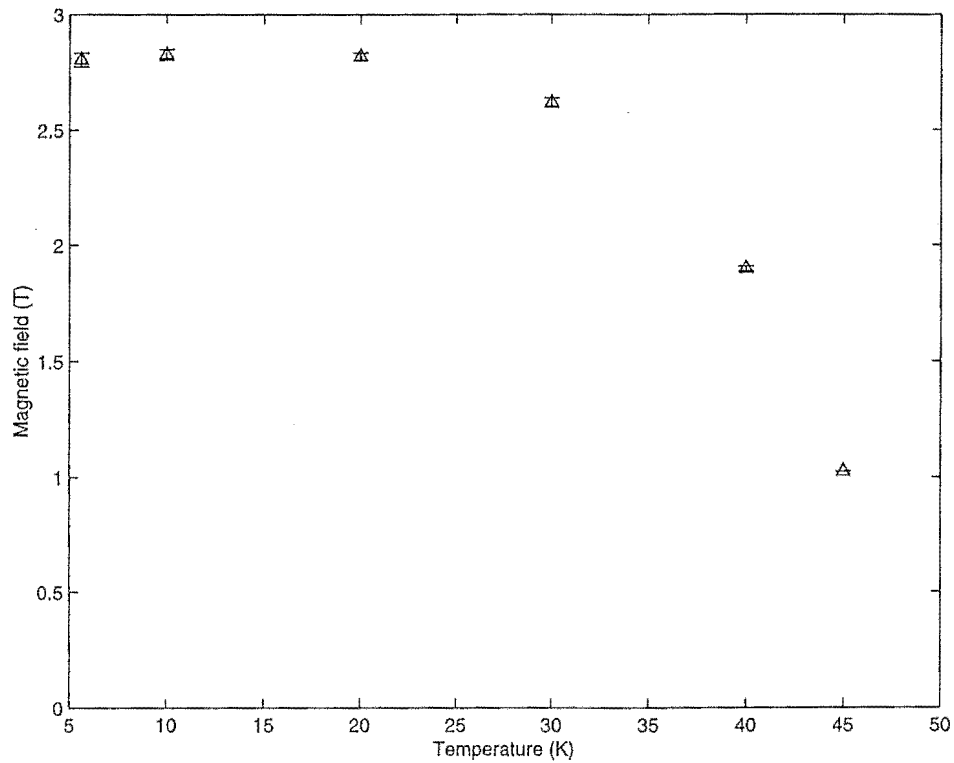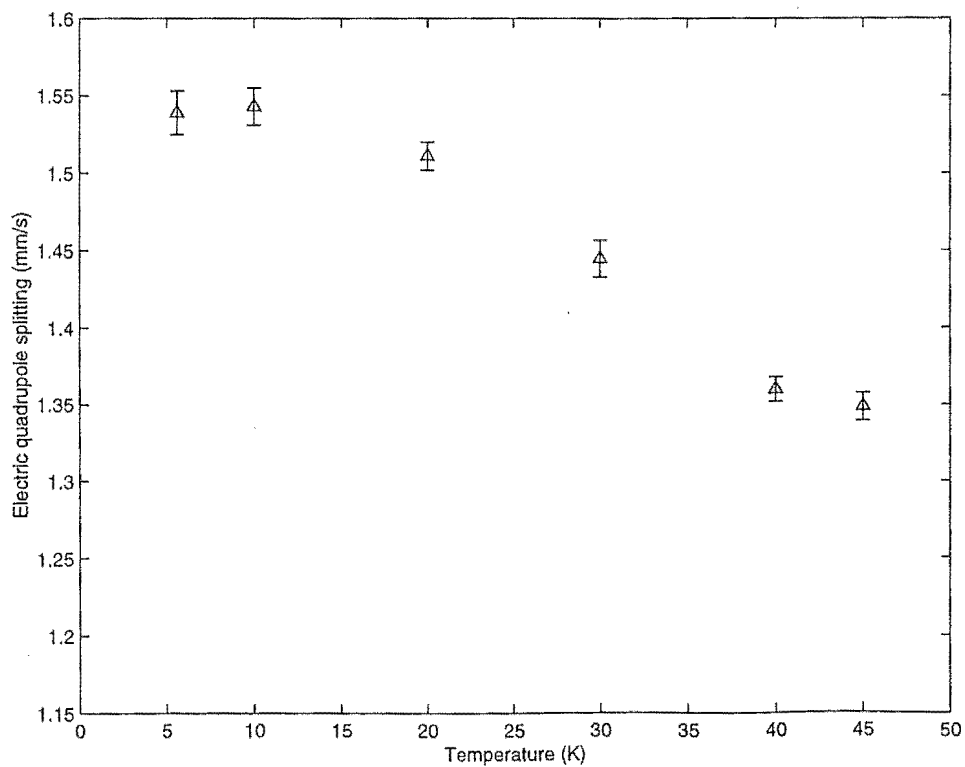

Figure 6.25: Electric quadrupole splitting QS for an $\mathrm{Fe}_x\mathrm{Ni}_{1-x}\mathrm{Cl}_2$ crystal with $x = 0.15$ at magnetic temperatures: model 2.

Chapter 7

Discussion and conclusions.

New Mössbauer spectra of the $Fe_xNi_{1-x}Cl_2$ mixed magnetic system were obtained, for crystals with a relative Fe content of $x = 0.031, 0.052$ and 0.15, with the first two concentrations bringing the system into the mixed magnetic phase of $Fe_xNi_{1-x}Cl_2$ at temperatures less than 50 K. This phase was of particular interest, since the behaviour of the Fe spins in the mixed phase has been interpreted differently by two groups of workers (as discussed in chapter 1).

An analysis of this new Mössbauer data did not lead to a conclusive determination of the magnetic ordering in the mixed phase. The Tamaki and Ito (1991, 1993) model (model 1), which had the hyperfine magnetic fields either near the z axis of the principal axis system (site 1) or rising out of the xy plane (site 2), generated simulated spectra which were only marginally better than simulated spectra from model 2 due to Pollard *et al* (1991) which had the hyperfine magnetic fields parallel to the principal z axis or nearly perpendicular to it (sites 1 and 2 for model 2). Both models generated fitted spectra that gave good approximations to the experimentally determined spectra, with small remaining anomalies in line shapes and depths. These anomalies are not unexpected, since all the Mössbauer absorbers produced came from single crystals having small concentration gradients. Also, thickness effects were evident in the $Fe_xNi_{1-x}Cl_2$ crystals with the higher Fe contents of $x = 0.052$ and 0.15.

The two models gave similar trends and values for most hyperfine quantities, with the exception being the quadrupole splittings QS. Model 2 calculated quadrupole splittings which decreased sharply at temperatures below 30 K for site 2, while model 1 gave a slower decrease of QS for that site. Previous workers calculated that model 2 data was consistent with the magnetic

order being parallel or perpendicular to the crystalline c axis (Pollard *et al* 1991). This analysis took the crystalline environment of $Fe_xNi_{1-x}Cl_2$ into account, and allowed the principal axis z to be different from the crystalline c axis. Workers who used model 1 previously (Tamaki and Ito 1991,1993) assumed that the principal z axis coincides with the crystalline c axis at all concentrations, which led them to conclude that the spins for site 1 and 2 were both oblique to the crystal axes.

Since models 1 and 2 both generate fitted spectra with approximately the same accuracy of fit (compared with the experimental spectra obtained for this thesis), the present work has not discriminated which model gives the better fit.

A theoretical study of the $Fe_xNi_{1-x}Cl_2$ mixed magnetic system was not attempted, since the complexity of the system limits the usefulness of the primary theoretical models of magnetic systems. Mean-field theory, which is easily applied to systems of magnetic spins, has the limitation that spin order throughout the system is identical for particular species of atoms or ions. This ignores many spin configurations that are energetically favourable, even though they are more disordered that the average mean-field state. Also, the possibility that complex clustering of ionic species occurs in mixed magnetic systems is neglected. Certainly, a mean-field approach could not predict the complex magnetic order that is experimentally observed in the mixed phase of $Fe_xNi_{1-x}Cl_2$, where magnetic order near the crystalline c axis and the xy plane coexists.

The more recent renormalization group theory is more exact, since it takes account of the long wavelength fluctuations in the magnetic order, which become important as critical points (lines) are approached. However, it is only useful over a very small critical region, which does not include most of the mixed phase. Also, the complexity of the theory limits its usefulness, with simple Hamiltonians being used to model magnetic systems. Again, these theories do not take into account possible clustering.

Because of these restrictions to the applicability of theoretical models to the $Fe_xNi_{1-x}Cl_2$ system, the numerical Monte Carlo technique was applied instead. This method had the advantage that the complicated structure

of $FeCl_2$ and $NiCl_2$ were simple to program, and clusters of metal ions could easily be simulated. Also, all of the interactions between the metal ions could be included (the magnetic anisotropy and the various exchange interactions between nearest in-plane, next-nearest in-plane and between-plane nearest-neighbouring metal-ion spins).

However, the results from simulating the $Fe_xNi_{1-x}Cl_2$ system, assuming a random distribution of ions, proved disappointing, with only one phase being predicted in the magnetic mixed phase for each ionic species. Even so, the overall structure of the magnetic phase diagram was predicted well, with the four experimentally observed phases being present.

Simulations using clusters of Fe ions were then performed, which gave orientations for the spins which were similar to model 1 values in the mixed phase. Although the exact results depended on the size and Fe content of the clusters chosen, they did have the common feature that Fe spins within the clusters were aligned close to (but not parallel to) the c axis, while the spins in the regions between the clusters aligned close to (but not wholly in) the xy plane.

Based on these calculations, the physical $Fe_xNi_{1-x}Cl_2$ system would thus appear to be a system containing small clusters of relatively high Fe content, embedded in regions with relatively lower Fe content. The change of the relative proportion of spins in site 1 or 2 is attributed to the ions in different clusters having different behaviour as the temperature varies. The smaller clusters tend to align near the c axis at low temperatures, but become dominated by the void regions as the temperature increases, and then align near the xy plane. This same change in behaviour occurs also for the larger clusters, but at higher temperatures. However, there exists no independent confirmation of the existence of these clusters in $Fe_xNi_{1-x}Cl_2$.

Any future work performed on the $Fe_xNi_{1-x}Cl_2$ system should concentrate on gaining high quality Mössbauer spectra for the region of the mixed phase with an Fe content near $x = 0.03$, since then the simulated spectra generated from models 1 and 2 show the greatest contrast, and high quality spectra could lead to a firm conclusion about which model better describes the magnetic behaviour of $Fe_xNi_{1-x}Cl_2$.

Acknowledgements

I wish to thank the following people;

- Dr Valda McCann my supervisor, for the advise, patience and help she has given me

- Dr Glynn Jones my assistant supervisor, especially for his enthusiasm and energy in helping me finish on time

- Drs John Laban and Nick Sheen, for their assistance using and operating the Mössbauer equipment and experiments

- The technical staff of the Physics and Astronomy Department, especially Mark Aitchison, Ron Culley, Bob Flygenring, Ross Richie, Clive Rowe, Wayne Smith and Tom Walker. Also Dave Macdonald and Rob McGregor of the Chemistry Department

- The secretarial and administrative staff of the Physics and Astronomy department, especially Beverly Bristrowe, Paul Bramley and Gill Evans

- Michael Flaws for the X-ray diffraction experiments he did for me in determining the atomic content of $Fe_xNi_{1-x}Cl_2$.

References.

Aharony A and Fishman S (1976) Phys. Rev. B **37** 23

Amit D (1984) *Field theory, the renormalization group and critical phenomena* (Singapore: World Scientific)

Aplesnin SS (1988) Phys. Stat. Sol. (b) **149** 267

Ausloos M and Elliot T (1983) *Magnetic phase transitions*
(Berlin, Germany: Springer - Verlag)

Bancroft G (1973) *Mössbauer spectroscopy: An introduction for inorganic chemists and geochemists* (London: McGraw Hill)

Bellac M (1991) *Quantum and statistical field theory* (Oxford, UK: Clarendon Press)

Bevart L, Frikkee E, Lebesque J and Jongh L (1978) Sol. State Commun. **25** 539

Binder K (1981) Phys. Rev. B **24** 11 6736

Binder K and Heerman D (1992) *Monte Carlo simulation in statistical physics* (Heidelberg, Germany: Springer-Verlag)

Binney J (1992) *The theory of critical phenomena* (Oxford, UK: Oxford University Press)

Birgeneau R J, Yelon W B, Cohen E and Makovsky J (1972) Phys. Rev. B **5** 2607

Chikazumi S and Charap S (1993) *Physics of Magnetism* (London UK.)

CRC handbook (1997) (London UK: CRC Press)

CRC handbook of chemistry and physics (1996-1997) (London UK: CRC Press, inc.)

Frauenfalder H (1963) *The Mössbauer effect* (New York USA : W A Benjamin inc)

Donnay J and Ondk H (general editors) (1973) *Crystal data determinative tables, third edition, volume II* (US Department of Commerce, USA)

Fishman S and Aharony A (1978) Phys. Rev. B **18** 7

Fujita T, Ito A and Ono K (1969) J. Phys. Soc. Japan **275** 1143

Gibb T (1976) *Principles of Mössbauer spectroscopy* (London: Chapman and Hall)

Greenwood and Gibb (1971) *Mössbauer spectroscopy* (London: Chapman and Hall Ltd)

Hernandez L, Diep H and Betrand D (1993a) Phys. Rev. B **47** 2602

Hernandez L, Diep H and Bertrand D (1993b) Phys. Rev. B **48** 15772

Hernandez L and Diep H (1994) J. Appl. Phys **76** (10) 7093

Hook J and Hall H (1991) *Solid state physics* (New York USA: Wiley)

Howes B, Price D and Wiltshire M (1984) J. Phys. C: Solid State Physics **17** 3669

Igarashi M, Tazuke Y and Nagata K (1992) J. Phys. Soc. Japan **616** 2081

Igel B, Kleemann W and Vilfan I (1990) J. Phys.:Condens. Matter **2** 4495

Imry Y and Ma S (1975) Phys. Rev. Lett. **35** 1399

Inawashiro M (1978) J. Phys. C: Solid State Phys. **12** 3200

Ito A, Tamaki T, Someya Y and Ikeda H (1983) Physica **120B** 207

Ito A (1986) Hyperfine Interact. **27** 81

Jacobs I S and Lawrence P E (1967) Phys. Rev. **164** 2

Karyagin S (1966) Sov. Phys. Solid State **8** 391

Kato T (1994) Phys. Stat. Sol. (b) **182** 219

Katsumata K, Yoshizawa H, Shirane G and Birgeneau R (1985) Phys. Rev. B **31** 316

Kittel, C (1986) *Introduction to solid state physics* (New York, USA: Wiley.)

Kolk B (1984) *Studies of dynamical properties of solids with the Mössbauer effect* (New York: Elsevier Science Publishers)

Lines M (1963) Phys. Rev. **131** 2 546

Kubo H, Uryu H, Nishihara H and Yasuoka J (1984) J. Phys. Soc. Japan **532** 2099

Kubo H, Hamasaki T and Uryu N (1989) Phys. Rev. B **40** 9098

Lawrie I (1990) *A unified grand tour of theoretical physics* (Bristol, UK: IOP Publishing)

Lindgard P A, Birgeneau R J, Als-Nelson J and Guggenheim H J (1975) J. Phys. C: Solid State Phys. **8** 1059

Ma S (1976) *Modern theory of critical phenomena* (Massachusetts USA: W A Benjamin)

Mandl F and Shaw G (1984) *Quantum field theory* (New York USA: Wiley)

Mano H (1990) Prog. of Theo. Phys. Supp. **101**

Matsubara F and Inawashiro S (1977) J. Phys. Soc. Jap. **42** 1529

Matsubara F and Inawashiro S (1979) J. Phys. Soc. Jap. **46** 6 1740

Mattis D (1981) *The theory of magnetism I* (Berlin, Germany: Springer-Verlag.)

Mook H, Koehler W, Maple M, Fisk Z, Johnston D and Woolf L (1982) Phys. Rev. B **25** 1 372

Oku M (1983) Prog. of Theo. Phys. **70** 6 1493

Pollard R, McCann V and Ward J (1982a) J. Phys. C: Solid State Phys. **15**

6807

Pollard R (1982b) *Mössbauer spectroscopy of some magnetic materials* Ph.D Thesis (Department of Physics and Astronomy, University of Canterbury, New Zealand)

Pollard R, Bauer C, Laban J and McCann V (1991) J. Phys. C: Condens. Matter **3** 5741

Ramond P (1981) *Field theory: a modern primer* (Massachusetts USA: Benjamin/Cummings)

Schobinger-Papamantellos P, Fischer P, Kaldis E, Halg W and Wachter P (1981) Sol. State Commun. **39** 759

Smart D (1966) *Effective field theory of magnetism* (Philadelphia USA: Saunders)

Sobol I (1994) *A primer for the Monte Carlo method* (London Great UK: CRC Press)

Someya Y (1981) J. Phys. Soc. Japan **50** 3897

Someya Y (1982) Phys. Stat. Sol. (a) **74** 167

Starr C (1940) Phys. Rev. **27** 984

Tamaki T and Ito A (1991) Hyperfine Interact. **68** 365

Tamaki T and Ito A (1993) Nucl. instr. and meth. in phys. research **B76** 52

Teller P (1995) *An interpretive introduction to quantum field theory* (New York, USA: Princeton University Press)

Thosar B and Iyengar P (editors), Srivastava J and Bhargava S (co-editors) (1983) *Advances in Mössbauer spectroscopy* (New York : Elsevier Science Publishers)

Ure M and Flinn P (1971) *Mössbauer effect methodology* **7** Plenum, New York USA

Vettier C and Yelon W (1975) Phys. Rev. B **11** 4700

Wagner D (1972) *Introduction to the theory of magnetism* (London, UK: Pergamon Press.)

Wertheim G (1964) *Mössbauer effect: principles and applications* (London Great UK: Academic Press)

Wilkinson M, Cable J, Wollan E and Koehler W (1959) Phys. Rev. **113** 2 497

Wilson K and Kogut G (1974) Physics reports **12** 2

Wiltshire M C K and Hayes W (1978) J. Phys. C: Solid State Phys. **11** 3701

Wong P, Horn P, Birgeneau R, Safinya C and Shirane G (1980) Phys. Rev. Lett. **45** 24 1974

Wong P, Horn P, Birgeneau R and Shirane G (1983) Phys. Rev. B **27** 1 428

Wong P (1986) Phys. Rev. B **34** 1864